Preoperative Systems for
Computer Aided Diagnosis based on Image Registration: Applications to

Original
Preoperative Systems for Computer Aided Diagnosis based on Image Registration: Applications to Breast Cancer and Atherosclerosis / RIYAHI ALAM, MOHAMAD SADEGH. - (2015). [10.6092/polito/porto/2592170]

Publisher:
Politecnico di Torino

Published
DOI:10.6092/polito/porto/2592170

Preoperative Systems for Computer Aided Diagnosis based on Image Registration: Applications to Breast Cancer and Atherosclerosis

Mohamad Sadegh Riyahi Alam

Department of Mechanical and Aerospace Engineering
Politecnico di Torino
Turin, Italy
February 2015

Supervisors:
Filippo Molinari
Alberto Audenino

Assistant Supervisors:
Valentina Agostini
Umberto Morbiducci

A dissertation submitted to Politecnico di Torino in partial fulfillment of the requirements for the degree of Doctor of Philosophy.

THIS PAGE WAS LEFT INTENTIONALLY BLANK

to my beloved father and mother who
devoted their precious life for us
put us in more than we expected
taught us nothing but pureness

Acknowledgment

Before starting my PhD, Marta Peroni who taught me what is “Biomedical Engineering”, told me studying doctorate would be a good opportunity to face how to solve the problems “individually”. During my career, many times I had to inevitably overcome both scientific and daily problems relying on self-capabilities. However obviously, conquering obstacles would become easier each time after one learns how to organize the time and energy and how to control the “stress” to maintain the problems ahead. I was from away, so the first year must have been on self-proving to the engineering society of “Electronics and Mechanics” that their combination had emerged the group of “Bioengineers”, so that I would be able to fix my position somewhere there. I was assigned “two professors” from both societies in which after a while I learned it is quite “unusual”. In any case, I tried to tighten the nodes of both societies. Of course did not go well. I chose a project from the “Electronics” and deploying my abilities I was able to obtain an acceptable outcome “scientifically”. Sometimes, in your life something happens that you are forced to believe there might be a superior spiritual power. The second year ahead, I found a project in which “accidentally” it was “Biomechanics”. I was going to Nagoya. Days were hard-working but super-satisfying. I went back with good outcome, again “scientifically”. Eventually, probably I will be able to connect the nodes from two societies. That is a good outcome “non-scientifically”. Now I admit PhD is the best opportunity to learn problem solving, in which brings you up in your next career, raise your expectations and self-confidence. That is why it is called “Over-qualified degree”. The “conclusion” is that it was “assolutamente” worth it stepping into this society where the following people helped me partially or permanently to arrive to this point:

Prof. Molinari, you made me comprehend how an excellent coordinator should be like. Indeed without your helpful comments and advices, I would not have been able to go forward all the way. Thank you for being around and fair.

Prof. Audenino, I appreciate your short helpful advices during my both works, when I was stuck and confused with the new concepts. You really know everything. You have always been kind and smiling to me.

Valentina, you know without your help I was not able to complete my works. You not only advised me on the projects but you also inspired me to keep moving forward. Grazie mille!

Umberto, you always were there if I had to ask you something. Thank for your aspiration on hard-working.

I appreciate all the members from both BioLab and my own office, Prof. Knaflitz, Prof. Balestra, Prof. Bignardi, Beppe (you are special!), Kristen, Issey, Valeria Chiono, and my dear friend Shady in which being right beside you was fun during more than half of my career. Thanks for energizing me. Both Giuseppi (Isu and Pisani), meeting you was the last best thing happened in my last year. Thanks for being around as good friends.

Last but not least, my parents, my dear father and mother, I do not have any word to express my gratitude for your efforts and kindness to keep me motivated in this way. My father, your precious advices helped me to love my field of work. My dear lovely mother, your heart-warming patience gave me a huge support during the hard times in my way. Thank you both!

Thank you all who helped me to finish this career with a complete confident, what I started with a doubt.

Abstract

Computer Aided Diagnosis (CAD) systems assist clinicians including radiologists and cardiologists to detect abnormalities and highlight conspicuous possible disease. Implementing a pre-operative CAD system contains a framework that accepts related technical as well as clinical parameters as input by analyzing the predefined method and demonstrates the prospective output. In this work we developed the Computer Aided Diagnostic System for biomedical imaging analysis of two applications on Breast Cancer and Atherosclerosis.

The aim of the first CAD application is to optimize the registration strategy specifically for Breast Dynamic Infrared Imaging and to make it user-independent. Base on the fact that automated motion reduction in dynamic infrared imaging is on demand in clinical applications, since movement disarranges time-temperature series of each pixel, thus originating thermal artifacts that might bias the clinical decision. All previously proposed registration methods are feature based algorithms requiring manual intervention. We implemented and evaluated 3 different 3D time-series registration methods: 1. Linear affine, 2. Non-linear Bspline, 3. Demons applied to 12 datasets of healthy breast thermal images. The results are evaluated through normalized mutual information with average values of 0.70 ± 0.03, 0.74 ± 0.03 and 0.81 ± 0.09 (out of 1) for Affine, BSpline and Demons registration, respectively, as well as breast boundary overlap and Jacobian determinant of the deformation field. The statistical analysis of the results showed that symmetric diffeomorphic Demons registration method outperforms also with the best breast alignment and non-negative Jacobian values which guarantee image similarity and anatomical consistency of the transformation, due to homologous forces enforcing the pixel geometric disparities to be shortened on all the frames. We propose Demons registration as an effective technique for time-series dynamic infrared registration, to stabilize the local temperature oscillation.

The aim of the second implemented CAD application is to assess contribution of calcification in plaque vulnerability and wall rupture and to find its maximum resistance before break in image-based models of carotid artery stenting. The role of calcification inside fibroatheroma during carotid artery stenting operation is controversial in which cardiologists face two major problems during the placement: (i) “plaque protrusion” (i.e. elastic fibrous caps containing early calcifications that penetrate inside the stent); (ii) “plaque vulnerability” (i.e. stiff plaques with advanced calcifications that break the arterial wall or stent). Finite Element Analysis was used to simulate the balloon and stent expansion as a preoperative patient-specific virtual framework. A nonlinear static structural analysis was performed on 20 patients acquired using in vivo MDCT angiography. The Agatston Calcium score was obtained for each patient and subject-specific local Elastic Modulus (EM) was calculated. The *in silico* results showed that by imposing average ultimate external load of 1.1MPa and 2.3MPa on balloon and stent respectively, average ultimate stress of 55.7 ± 41.2kPa and 171 ± 41.2kPa are obtained on calcifications. The study reveals that a significant positive correlation (R=0.85, $p<0.0001$) exists on stent expansion between EM of calcification and ultimate stress as well as Plaque Wall Stress (PWS) (R=0.92, $p<0.0001$), comparing to Ca score that showed insignificant associations with ultimate stress (R=0.44, $p=0.057$) and PWS (R=0.38, $p=0.103$), suggesting minor impact of Ca score in plaque rupture. These average data are in good agreement with results obtained by other research groups and we believe this approach enriches the arsenal of tools available for pre-operative prediction of carotid artery stenting procedure in the presence of calcified plaques.

Table of Contents

List of Tables

List of Figures

Section 1: Computer Aided Diagnosis System for Breast Cancer Detection in Dynamic Area Telethermometry

Chapter 1 : Introduction to Dynamic Area Telethermometry

1.1. Dynamic Area Telethemometry

Early detection of breast cancer has been shown to be crucial for the survival of the patients [1]. Dynamic Area Telethermometry (DAT) has been explored as a potential complementary technique with respect to mammography. The basic assumption is that normal tissues show temperature modulation that is different from cancerous tissue [2]. The surface temperature modulation caused by cancer, occurs at specific frequencies [2], [3]. Hence, the spectral analysis of the time variations of the local temperature could allow for non-invasively detecting cancerous lesions.

In general, IR radiation covers wavelengths that range from 0.75μm to 1000µm, among which the human body emissions that are traditionally measured for diagnostic purposes only occupy a narrow band at wavelengths of 8µm to 12µm [4]. This region is also referred to as the Long-Wave IR (LWIR) or body infrared rays. Another terminology that is widely used in medical IR imaging is Thermal Infrared (TIR), which, as shown in Figure 1.1, covers wavelengths beyond about 1.4µm. Within this region, the infrared emission is primarily heat or thermal radiation, and hence the term thermography. The image generated by TIR imaging is referred to as the thermogram. The Near Infrared (NIR) region occupies wavelengths between 0.75µm and 1.4µm. The infrared emission that we observe in this region is not thermal [4]. Although the NIR and Mid-Wave IR (MWIR) regions are not traditionally used in human body screening, the new generation detectors have enabled the use of multispectral imaging in medicine, in which both NIR [5] and MWIR [5] are observed in different diagnostic cases.

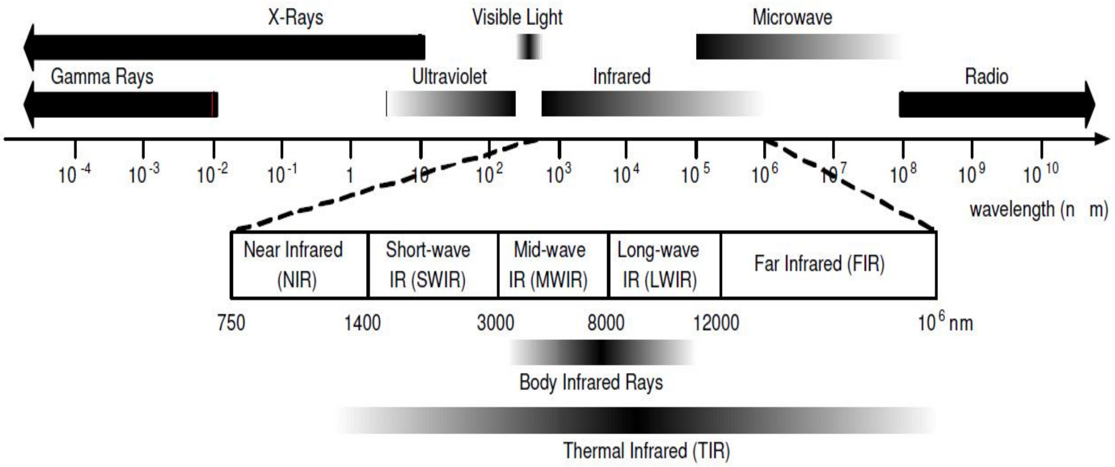

Figure 1.1. The electromagnetic spectrum and the IR region.

A general DAT procedure starts with a thermal camera generating consecutive 2D frames of the patient’s breasts, reconstructed as 3D thermograms. Then all the frames are segmented in order to remove artifacts and reduce the computational time. 3D time-series frame registration is performed to eliminate the movement by aligning the corresponding pixels of each frame. Eventually, the time-temperature series of each pixel during the time interval of acquisition is obtained and transformed to the frequency domain to measure the modulation of the temperature. More specifically, the Power Spectral Density (PSD) of the time-temperature signal is obtained for each pixel. Then, the power in a specific frequency band is calculated obtaining a single final image. Figure 1.2 shows the whole procedure.

In eventual spectral analysis of the dynamic infrared imaging for breast cancer diagnosis, motion reduction of the patient is necessary, since it is combined with the signal of interest acting as the noises. Therefore, motion reduction on the frames of thermogram is crucial. In our previous work [9], a feature-based registration was applied on breast dynamic thermograms using a linear piecewise polynomial transformation function with linear interpolation technique in order to compensate the patients movements. However, there are certain drawbacks in feature-based registration such as difficulty in placing the markers manually on the patient during the acquisition as well as obtaining the optimal number of markers, necessity of additional prior marker detection algorithms, limitation on choosing types of registration transformation function/ interpolation techniques/similarity metric and optimization method. Therefore, performing automated intensity based motion reduction methods on the sequence of frames as well as landmark-based registration by taking the criteria concluded in the previous article into the account and annotating the landmarks on the dataset automatically, we can intensively facilitate the whole acquisition process and dramatically advance the registration routine by choosing the best suited method in motion compensation for DAT modalities. Clinical information is obtained by analyzing in the frequency domain the small temperature fluctuations taking place in numerous breast areas constituted by a few pixels.

Malignant cells release a chemical into the surrounding area called nitric oxide (NO), causes to keep the existing blood vessels open (vasodilation), which awake the inactive cells and create new one [6]. This is called angiogenesis and since malignant/aggressive and benign/normal tissues have different infrared signals and temperature and physiological cardiovascular activities, due to activities such as angiogenesis which is crucial for a tumor cell, hence thermo cameras can be used to identify the latter activities and depict the temperature map predefined as Hot Spots (final spectral image). The harmonic analysis of the time course of temperature fluctuations allows obtaining information on the local blood perfusion using specific characteristics of the vasculature supplying blood to the tumor, and the altered metabolism of cancerous tissue. In literature, it has been reported that temperature fluctuations have an important diagnostic value in oncology. [6]

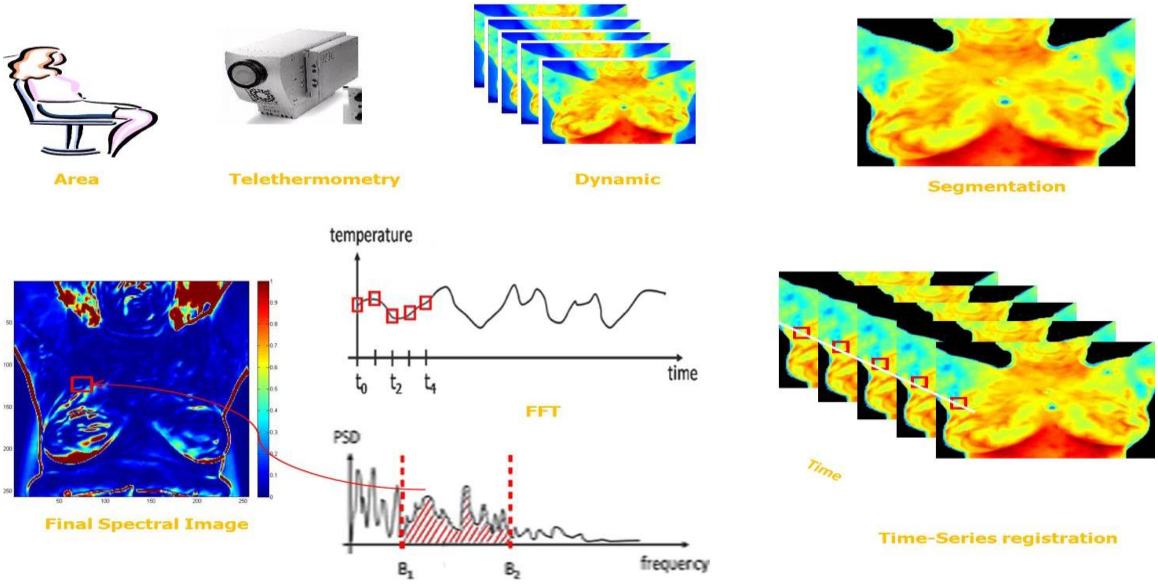

Figure 1.2. General procedure of a DAT starting from patient acquisition, segmentation of breast region, registration of corresponding pixels on time temperature series and converting the signal to frequency domain followed by computation of PSD over specific frequency.

In this work the breast regions in all frames are masked out and segmented from the background area, using a semi-automated algorithm developed by N. Scales et al [10] that employs Canny edge detection and the Hough transform to detect the symmetric breast boundaries and isolates the region of interest. Breast segmentation was checked and altered where necessary using algorithm embedded in 3D Slicer software based on multiple label mapping and Otsu's thresholding, hence only body and breast region is registered and evaluated which helps in computational time and the accuracy of the algorithm. Unsharp masking filtering is applied on the images prior to evaluation to negate the noise and smoothness effect of interpolation.

DAT as a new modality can be deployed to detect the breast cancers relatively close to the surface of the body. In a DAT detection examination, depending on the frame rate of the thermal camera as the sampling frequency, several frames are acquired from the patient during a certain amount of time. Based on Nyquist frequency, the sample rate of up to twice larger than the chosen frequency band is sufficient. However depending on the limitation of the camera, the more sampling frame rate one chooses, the obtained preliminary information is consecutive and reliable. The perfusion frequency of the breast region is very low ranged from 0.1 to 1 Hz (considering the ambient frequencies banded up to 6 Hz) mainly belonging to cardiogenic and vasomotor frequencies [2], [3]. DAT is based on the assumption that normal tissues radiate different temperature fluctuations, comparing to the malignant tissues due to the activities such as angiogenesis [1]. DAT framework is proposed as following: first the infrared intensity versus time series function at each pixel of the sequential frames is obtained and using PSD of the time-series, the average integrated power distributed over the banded temperature frequency is calculated. Finally the integrated outcome value is mapped into each pixel of a 2D thermal map image.

Prior to spectral analysis of the signal of interest for the clinical evaluation, superimposed noise signal emerged by the patient movement must be distinguished and eliminated and the sequential dynamic frames must be registered. The movement during the consecutive dynamic frames, disarrange the time-temperature series of each pixel, causing to false positive in the eventual thermal map evaluation.

Section 1 of this thesis is organized as follows:

Chapter 1 introduces the major functionality of DAT framework as a complementary modality for breast acquisition and cancer detection along with the problems we defined and the goal of the research. Moreover the general concepts on image registration methods are presented as well as evaluation of image registration methods.

In Chapter 2, we introduced our novel method of 3D time series registration methods in which they are utilized for patient movement reduction. Then the DAT specific registration evaluation methods are introduced along with data acquisition procedure.

Chapter 3, we show the results of our methods along with pre and post registration comparisons. Then we use spectral analysis of temperature modulation on time temperature series as one DAT specific evaluation method.

Finally in Chapter 4 we state the discussion followed by the eventual conclusion.

1.2. Problems and Aims of the work

A major problem exists during a DAT examination. While acquiring several frames of patients' breasts, the movements disarrange the time-temperature series of each pixel, thus originating thermal artifacts that might lead to a false positive or false negative in the final spectral image used for diagnosis. Therefore, prior to spectral analysis, the patient movement must be compensated and the sequential frames must be aligned using a 3D time-series registration method [4].

We proposed an automated framework which after acquiring the thermal images, segments the breast region of interest using non-interventional automated method and registers the thermal frames to realign the sequence of images in order to attenuate the frequency difference of the same corresponding pixels which represents the fluctuations in the temperature as well as to compensate the patients' movements during the acquisition. Finally by performing a thermal frequency spectral analysis on the sequence of images, we obtain the spectral image in order to perform estimations on detecting the suspicious cancerous regions.

In the literatures, many probes on registering static visible and infrared image have been performed, however very few methods are proposed on automated real-time motion reduction in sequential dynamic infrared frames especially in breast cancer detection. The most relevant research is presented by [8] where the final aim is to detect the breast cancer tissue by performing combination of several spatial and frequency filtering methods in order to increase the signal-noise ratio on the sequence of 1200-1700 frames, acquired by 50 and 70 Hz frame rate of 24s breath-holding images. However the movement of the patient is neglected as a prior-stabilization process and the algorithms are performed by using Matlab, not suited for a real-time application. In all of the similar works movement of the patient as a noise is either neglected or a breath-hold process is supposed as assumption where in the 10-30s acquisition process, hardly can be expected from the patient. Likewise in the very few previous attempts, no elaboration has been made in terms of complete technical aspects of the frame registration.

In our previous work [9], a feature-based registration was applied on breast dynamic thermograms using a linear piecewise polynomial transformation function with linear interpolation technique in order to compensate the patients movements. However, there are certain drawbacks in feature-based registration such as difficulty in placing the markers manually on the patient during the acquisition as well as obtaining the optimal number of markers, necessity of additional prior marker detection algorithms, limitation on choosing types of registration transformation function/ interpolation techniques/similarity metric and optimization method. Therefore, performing automated intensity based motion reduction methods on the sequence of frames as well as landmark-based registration by taking the criteria concluded in [] into the account and annotating the landmarks on the dataset automatically, we can intensively facilitate the whole acquisition process and dramatically advance the registration routine by choosing the best suited method in motion compensation for DAT. Figure 1.3 depicts the problem of misalignment of the pixels in the sequential consecutive frames of DAT.

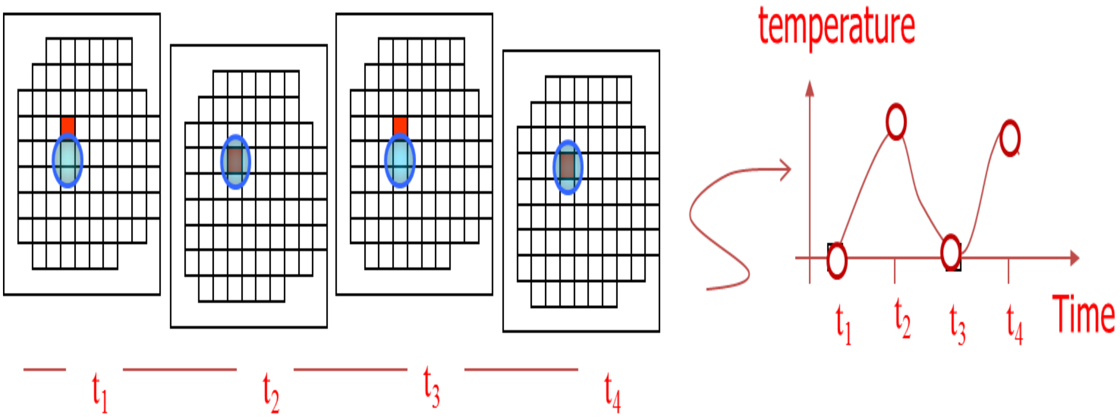

Figure 1.3. Problem exists in DAT procedure during patient acquisition leading to misalignment of the temperatures along the frames.

Image registration is the process of defining the transformation between two images so that the coordinates in one image correspond to those in the other. Depending on the type of transformation function, it is referred to as linear or deformable registration [5].

Very few methods were proposed for dynamic infrared images registrations, all were concentrated on manual feature-based motion reduction [6], [7], [8]. In these methods several markers are located on the region of interest of patient's breast skin before the acquisition. The markers are then recognized and used to construct the transformation function obtaining the displacement to be compensated. In a previous work from our team [9], [10] a marker-based registration was applied on breast dynamic thermograms. However, this technique had some drawbacks: i) it was cumbersome to manually place the markers; ii) the registration was dependent on the number of markers; iii) detection algorithms were needed to accurately locate the centroid of each marker; iv) there were limitations on choosing types of registration parameters. Figure 1.4 shows the landmark placement on the breast in order to follow the manual feature based registration method. These points of the landmarks are utilized as a transformation function for patient reduction methods. Figure 1.4 (b) shows the thermogram of the same image in which the landmarks are completely visible as noises on the image that interrupt the final decision.

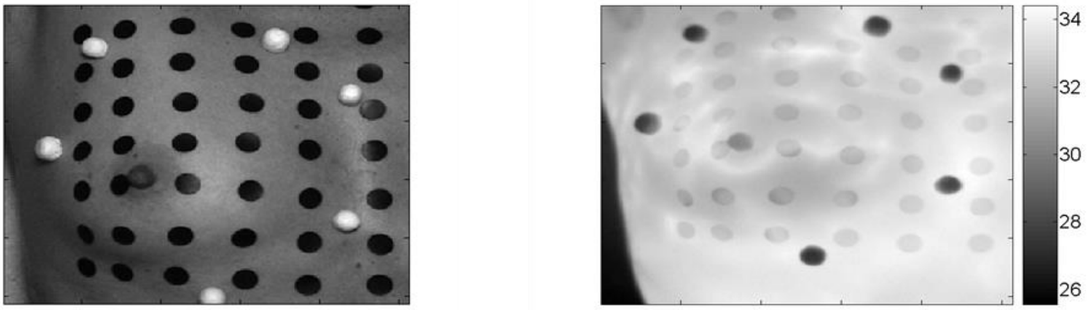

(a)

(b)

Figure 1.4. (a) Traditional Landmark placement on the breast for manual feature based registration. (b)Thermogram obtained with landmarks on the breast.

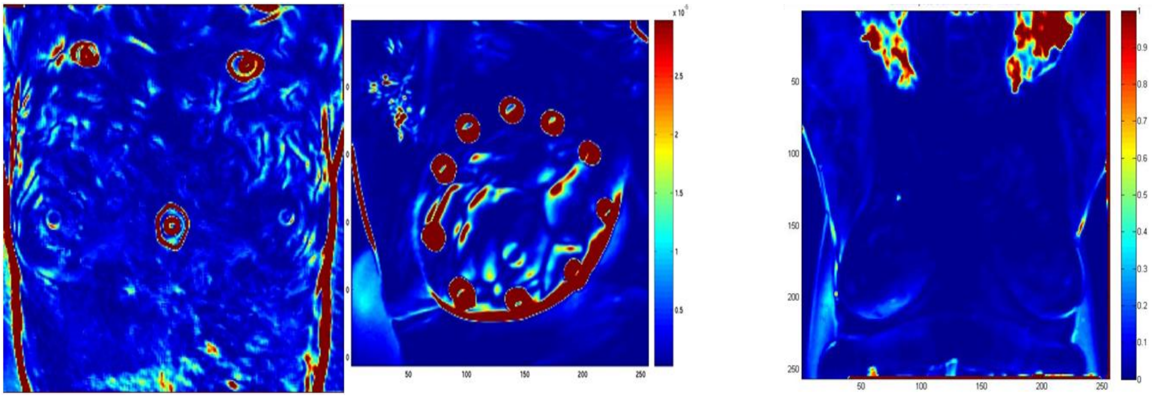

(a) (b)

Figure 1.5. (a) Final PSD spectral image obtained after placing the landmarks. (b) Smoothed spectral image obtained without landmark deploying an automated registration.

Figure 1.5 panel (a) shows final spectral image with landmarks placed on the breast region in which ruined the image by noises and misleads the radiologists in diagnosis of the suspicious spots. On the contrary in panel (b), by deploying automated registration method without landmarks, we can obtain a smooth final PSD image which helps the radiologists to clearly focus on vulnerable spots only.

The purpose of this paper is to implement and test different types of marker-less linear and non-linear intensity based registration methods (which we implemented in ITK [11]) on the healthy subjects of dynamic time series breast infrared images, in order to obtain the best suited registration method along with optimization of DAT registration parameters.

We developed Affine linear registration along with Bspline and Demons nonlinear 3D time-series registration method by minimizing the spatial displacement of the corresponding points on the images. Performance of the methods was evaluated using assessment of DAT specific symmetric alignment of breast boundary followed by image similarity measurement using Normalized Mutual Information (NMI) and eventually Jacobian determinant of the transformation. All the methods are performed automatically without human intervention.

DAT motion compensation evaluation is crucial since, there are huge amount of works that have been done on evaluating different registration techniques on different current state of the art modality dataset of different parts of body e.g. Brain CT/MRI, Xray-mammography, head and neck, pulmonary CT, Prostate etc. taking into account the physiological/anatomical motion properties, in order to obtain an optimal compensation of the excess movement. However, there is no work having done on evaluation and comparison of different registration methods on time series frames of dynamic thermograms. Despite the latter medical modalities which two different mono/multi-modalities images are used as fixed and moving image to perform the registration algorithm, in this field of work, different slices/frames inside one 3D image/thermogram should be aligned on eachother, taking into account the first frame as fixed image and all the rest sequential frames as the moving image. This fact brings the automated intensity based registration into a new challenge. This process of "Time-series registration" is on the demand of the developers in this field of work, since it has not been introduced before in any open source software society and it is considered as a novelty.

1.3. CAD for breast cancer detection in IR imaging

According to American Cancer Society's report on Cancer Facts and Figures [12], breast cancer is the most commonly diagnosed cancer in women, accounting for about 30 percent of all cancers in women. In 2004, approximately 215,990 women in the United States receive a diagnosis of invasive breast cancer and 40,110 die from the disease. Figure 2 shows the growth in estimated new breast cancer cases in women since 2001. On the other hand, research [12] has shown that if detected earlier (tumor size less than 10mm), the breast cancer patient has an 85% chance of cure as opposed to 10% if the cancer is detected late. Other research also shows evidence of early detection in saving life [17], [18]. Many imaging modalities can be used for breast screening, including mammography using X-ray, IR, MRI, CT, ultrasound, and PET scans. Although mammography has been the base-line approach, several problems still exist that affect the diagnostic accuracy and popularity. First of all, mammography, like ultrasound, depends primarily on structural distinction and anatomical variation of the tumor from the surrounding breast tissue [18]. Unless the tumor is beyond certain size, it cannot be imaged as X-rays essentially pass through it unaffected. Secondly, the mammogram sensitivity is higher for older women (age group 60-69 years) at 85% compared with younger women (<50 years) at 64% [18] whose denser breast tissue makes it more difficult for mammography to pick up suspicious lesions. Thirdly, patients gone through mammography screening are exposed to X-ray radiation which can mutate or destroy the tissue they penetrate. A new study in the British medical journal [19] shows that screening actually leads to more aggressive treatment, increasing the number of mastectomies by about 20% and the number of mastectomies and tumorectomies by about 30%. Finally, mammography is relatively expensive nowadays and is less convenient to take. Even though other modalities like MRI and PET scan could provide valuable information to diagnosis, they are not popularly adopted for various reasons including high cost, complexity and accessibility issues [19]. Compared to mammography, MRI, CT, ultrasound, and PET scans which are also called the after-the-fact (a cancerous tumor is already there) detection technologies, IR imaging is able to detect breast cancers 8-10 years earlier than mammography [18], [19]. In [20] reported that the average tumor size undetected by IR imaging is 1:28cm vs. 1:66cm by mammography. In addition, IR imaging is non-invasive, non-ionizing, risk-free, patient-friendly, and the cost is considerably low. These features, together with its early detection capability, have enabled IR imaging a strong candidate for complementary diagnostic tool to traditional mammography.

Computer-aided diagnosis (CAD) has been playing an important role in the analysis of IR images, as human examination of images is often influenced by various factors like fatigue, being careless, etc. The detection accuracy is also confined by the limitations of human visual system. On top of all these factors, a shortage of qualified radiologists also put an urgent demand on the development of CAD technologies. Currently, research on smart image processing algorithms on IR images tends to improve the detection accuracy from three perspectives: smart image enhancement and restoration algorithms, asymmetry analysis of the thermogram including automatic segmentation approaches, and feature extraction and classification.

All objects with a temperature above absolute zero (-273 K) emit infrared radiation from their surface. The Stefan-Boltzmann law, also known as Stefan's law, states that the total energy radiated per unit surface area of a blackbody in unit time (blackbody irradiance), is directly proportional to the fourth power of its absolute temperature. This law can be mathematically expressed as:

$$E = \sigma T^4 \qquad \text{(Equation 1.1)}$$

where
E = total emitted radiance in W/m^2
σ = 5.6697 × 10-8 W m^{-2} K^{-4} (Stefan-Boltzmann constant)
T = absolute temperature of the emitting material in Kelvin.

In order to maintain a constant temperature within the human body, the excess heat produced during metabolic activity is dissipated in part, in the form of infrared radiation. The wavelength of the radiation that leaves the surface of the skin at any given point is proportional to the local temperature of the skin at that point. Infrared rays are found in the electromagnetic spectrum within the wavelengths of 0.75 micron - 1mm, and the human skin emits infrared radiation mainly in the 2 - 20 micron wavelength range, with an average peak at 9-10 microns. Since the emissivity of human skin is extremely high (within 1% of that of a black body), sensors in medical systems can measure infrared radiation emitted by the skin and convert it directly into precise temperature values using the Stefan-Boltzmann law. Each calculated temperature is encoded with a different color to generate a temperature map.

Thermographic assessments must take place in a controlled environment. The principal reason for this is the nature of human physiology. Changes from a different external environment, clothing, etc. can produce undesirable thermal effects. According to a report by [20], abstaining from sun exposure, cosmetics and lotions before the procedure, along with 15 minutes of acclimation in a florescent lit, draft and sunlight-free, temperature and humidity-controlled room maintained between 18-22 °C, and kept to within 1 degree of change during the procedure, is necessary to produce a physiologically neutral image free from interference.

1.4. Time-series image registration

Image registration is seen as an optimization problem, having a cost function that consists of a similarity measure between two images namely, fixed (reference) and moving (target) images (Equation 1.2). By assuming two corresponding points on two images the similarity measure between the points is optimized to find the best optimum transformation in order to compensate the displacement by mapping the domains on the moving image onto fixed image.

$$\mathrm{C}(T) = -\mathrm{C}_{similarity}\left(I(t_0), T\big(I(t)\big)\right) \qquad \text{(Equation 1.2)}$$

Where, $I(t_0)$ is the fixed image and $I(t)$ is the moving image. T represents the transformation function and $\mathrm{C}_{similarity}$ represents the similarity applied between two images. Final output of registration procedure which is the product of aligning two images is called “warped image”.

In time-series registration method, different frames inside a 3D thermogram are aligned, where the first frame is chosen as fixed and all the rest sequential frames as the moving image.

In breast dynamic infrared images, intensities directly correspond to temperature, hence the similarity metrics must minimize the geometric displacement of the pixels, instead of the pixel intensities, otherwise leads to losing information.

The solution of optimization problem in registration is transformation parameters or Deformation Fields (DF), which is the displacement found between the fixed and transformed corresponding point. As shown in Figure 1.6, DF can be displayed as a vector field to show the movement/displacement at each frame. DF is also exploited to evaluate how successful the registration is performed.

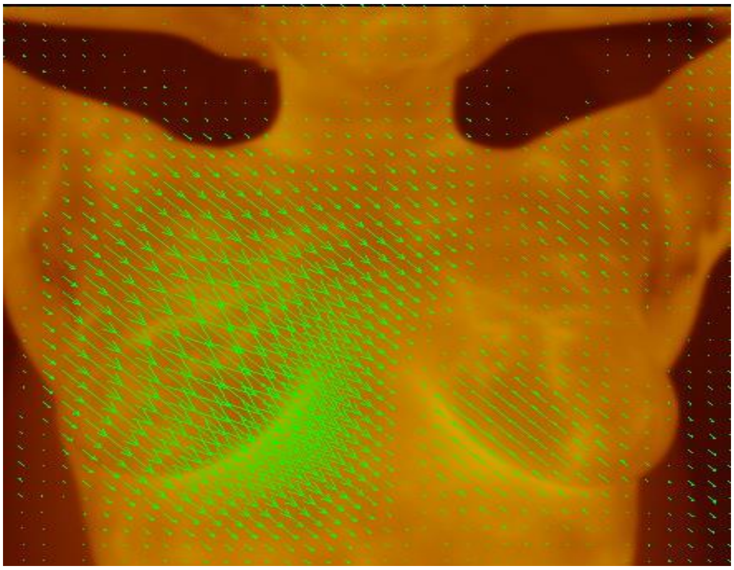

Figure 1.6. DF as outcome of registration process has been overlaid on fixed images belonging to current frame of one of our subjects. Parts of the body with burden of vectors represent a large movement of the patient during DAT acquisition process.

Let's simulate one iteration of the deformable registration procedure. The idea relies on passing the physical or pixel-wise coordinate parameters (x,y,z) belonging to fixed image to each term of the cost function which is composed of similarity metric function and a regularization function(s). The cost function searches the best alignment between two images depending on type of the similarity metric. For example if we have chosen the intensity based Sum of Squared Difference (SSD) between two images, it will utilize each coordinate parameters of the fixed image and find the corresponding point on the moving image and compute the squared difference between those points. The role of the optimizer is to minimize this difference.

The regularization function computes the displacement (Deformation Field) between two images at each iteration to compensate the irregularities and misalignment occurred. When the final value of the cost function is calculated, it is passed to the optimizer.

Then based on the "stopping criteria" defined for the optimizer, it evaluates the value received at that specific iteration to whether continue the optimization procedure or it should be stopped by that point. This optimization iteration is done until the optimizer meets the stopping criteria and the distance between two points in term of intensity and the physical coordinate has been set to minimum. In this point the finally obtained transformation parameters are considered as the most optimum and the best for aligning two images.

Eventually using the obtained optimized transformation parameters, we obtain the warped image. This stage is done through the resampling of the moving image with respect to the optimal transformation parameters. (Figure 1.7)

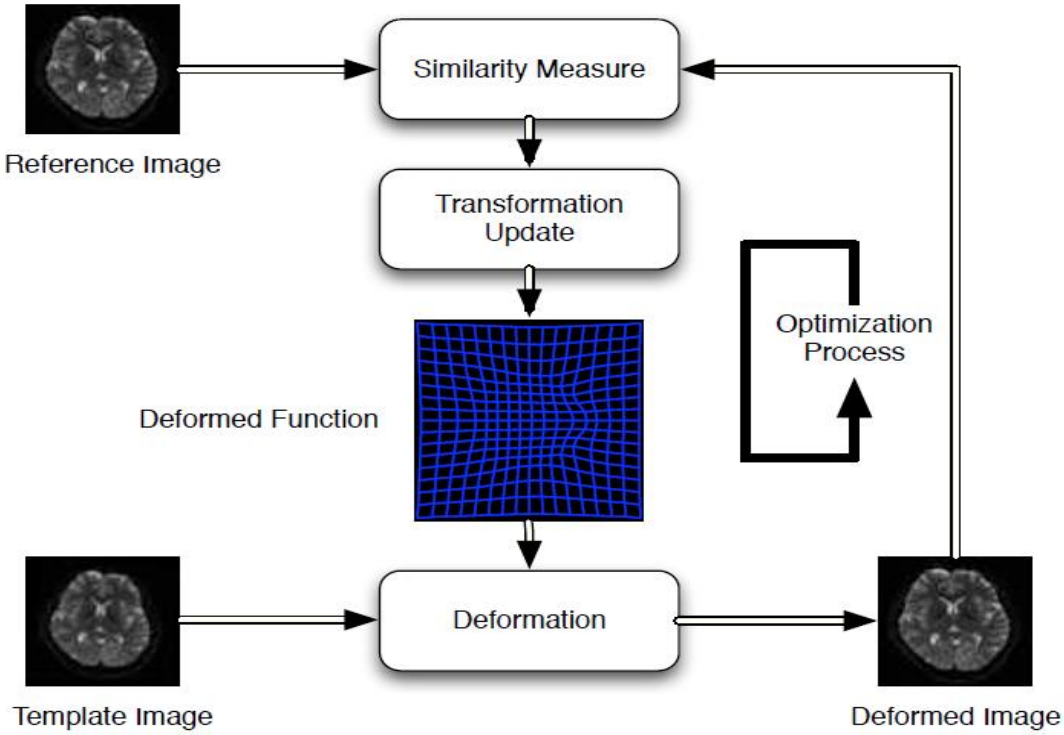

Figure 1.7. The whole procedure of the image registration [12].

Prior to experiments, breast regions in all frames are segmented from the background area, using a semi-automated algorithm developed by N. Scales et al. [10] that employs Canny edge detection and the Hough transform to detect the symmetric breast boundaries and isolates the region of interest. Breast segmentation was checked and altered where necessary using an algorithm embedded in the software 3D Slicer [11], and based on multiple label mapping and Otsu’s thresholding. Thus, only body and breast region are registered. This reduces the computational time and improves the overall accuracy of the algorithm. Unsharp masking is applied to negate the noise and oversmoothness of interpolation. The general pipeline of the method is demonstrated in Figure 1.8.

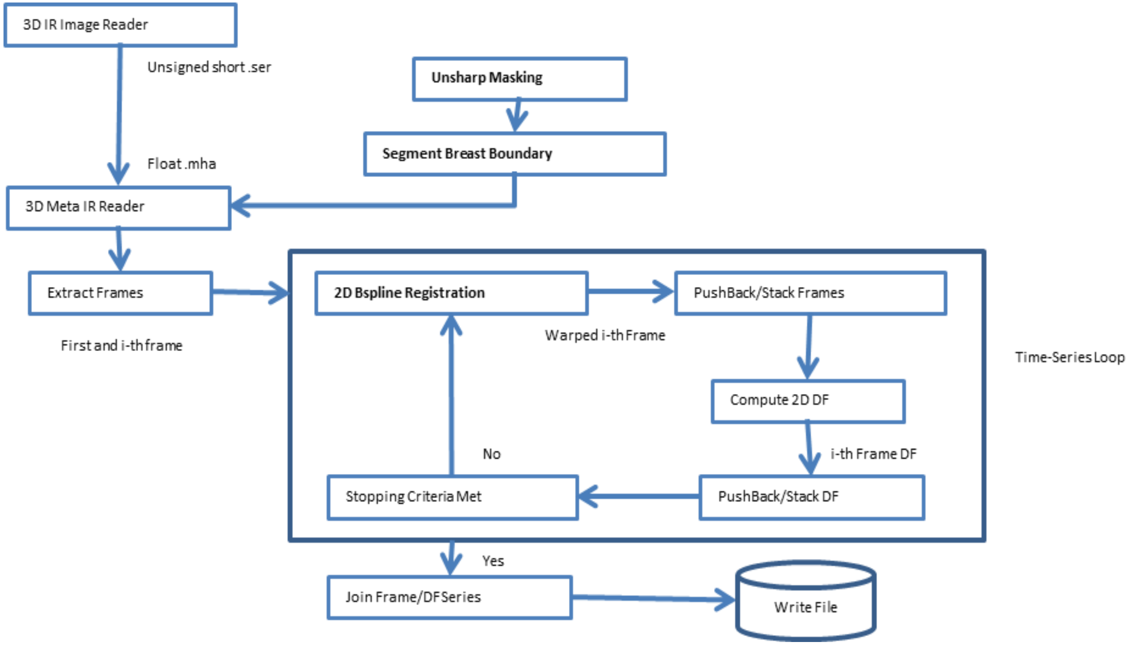

Figure 1.8. General pipeline of 3D time-series registration method.

1.5. Registration evaluation methods

Evaluation of non-rigid image registration algorithm and the final result are a hard task since point-wise correspondence between two fixed and warped or fixed and moving images are typically not known. Many researcher communities have been working to define and exploit a standard benchmark and a framework to assess deformable registration algorithms. However there is not a unique and singular application to evaluate all of the registration methods for all kind of images and modalities.

Generally there are two types of ways to evaluate the final database of registration results. The first one is to profit the analytical statistical measures to evaluate the differences between fixed and warped vs. fixed and moving image. Also the final deformation field (transformation) can be evaluated, either using a ground truth deformation field or by computing the Jacobean determinant, inverse consistency, etc.

The second way is to use a standardized database to analyze and assess final results. In the following both methods are briefly described.

The following four main statistical methods are usually used to assess the performance of registration:

1- Structure overlap

This kind of statistics measures how well the labeled volumes or surfaces of source image and target image agree with each other after registration. In this method the percentage of overlap of the whole or part of the desired region of the image is calculated before and after registration. The major point which has to be taken care in this kind of evaluation is to use accurate contours for the evaluation. This is because usually a meta 3D/2D image contains extreme elements which are unnecessary for the evaluation of the only patient area. Hence those parts in the image must be masked or cropped. Thus defining a proper contour over the patient area of the image increases the accuracy of the final evaluation.

Some of these methods such as Percentage of overlap, edge overlap, etc., are investigated in the next chapter quite in detail both in term of theory and in term of implementation.

2- Intensity based differences error

These measure intensity difference between deformed and target intensity images. Examples of these errors include intensity variance (RMS error), mutual information and average volume method (mean and median).

3- Deformation field statistic error

In this method the specification of the final deformation field or the transformation are evaluated. In case of availability of the synthetic deformation field, the difference between the finally obtained deformation field of the registration and the synthetically applied transformation are evaluated.

4- Landmark error

These statistics measure the distance between deformed landmarks and corresponding target landmarks. Distance between two point sets can be measured using Euclidean distance, closest distance or any other suitable metric.

The other method to evaluate the registration performance is to use the benchmarks provided by the research communities for the assessment. These research groups provide the community with images to register and then evaluate the results. The “Retrospective Image Registration and Evaluation Project" [21] led by Jay West Fitzpatrick of Vanderbilt University took this approach to evaluate inter-modality registration algorithms. A common set of images were used to evaluate the performance of registration algorithms. Researchers registered the images with their own registration algorithms and then send an ASCII codes containing the original and transformed points back to Vanderbilt. Registration algorithms were evaluated using the target registration error.

Castillo et al. [24] evaluated deformable image Registration (DIR) spatial accuracy using large sets of expert-determined landmark point pairs. Each of their data sets has associated with it a coordinate list of anatomical landmark point sets which serve as a reference of evaluating DIR spatial accuracy within the lung. They provide published DIR spatial accuracy results on their website (http://www.dir-lab.com). Results are reported as mean 3D Euclidean magnitude distance between calculated and reference landmarks.

If ever there is rarely a “Gold Standard" or “Ground Truth” correspondence map that could be a best way to judge the performance of a registration algorithm.

The website (http://www.vmip.org/) set up by Pierre Jannine directs people to papers and references about validation and evaluation in medical imaging processing, and a list of validation data sets.

Chapter 2 : Methods and Implementation

2.1. Data Acquisition

The DAT process starts with the patient acquisition. We use an AIM256Q camera (long wave quantum well infrared photodetector, 256 × 256 pixels, produced by AEG Infrarot-Module GmbH, Germany) to acquire 10s of given time. The heat radiated from the breast (ROI) is captured and digitized as 50 frames (images)/s. Therefore, for the total 10s we acquire 500 thermal images from the breast. The sample thermograms are 3D sequential images, comprising 500 frames, with dynamic ranges of 14 bits identifying the final thermal texture map as well as the intensity values are sub-sampled by 14. Element/pixel size (Spatial resolution) is 1.5 mm, turns out be 38×38 cm Field Of View (FOV), hence the image resolution is 256×256×476 with the 3rd dimension belonging to number of slices/frames. The maximum intensity value for un-subsampled images is close to 65000 (radiated-heat unit) and for subsampled images is less than 1.

The first acquisition using the camera was performed where we acquired 4 normal patients, each 3 experiments, thus 12 samples are acquired as a normal cases to perform the analysis. A Parallel cable is used on EPP port for downloading each 3D thermal image from the camera to the PC and it takes less than 2 minutes. It took 50 minutes to acquire 12 cases.

All the thermograms were registered using the aforementioned methods. We conducted a nonparametric Friedman test to compare the results obtained from each method in a statistical manner. Then in order to highlight which method has significantly smaller error, a Post-hoc analysis was performed through an Inter-subject analysis which is demonstrated in the next section. Figure 2.1 represents samples of the first acquired frame for each subject.

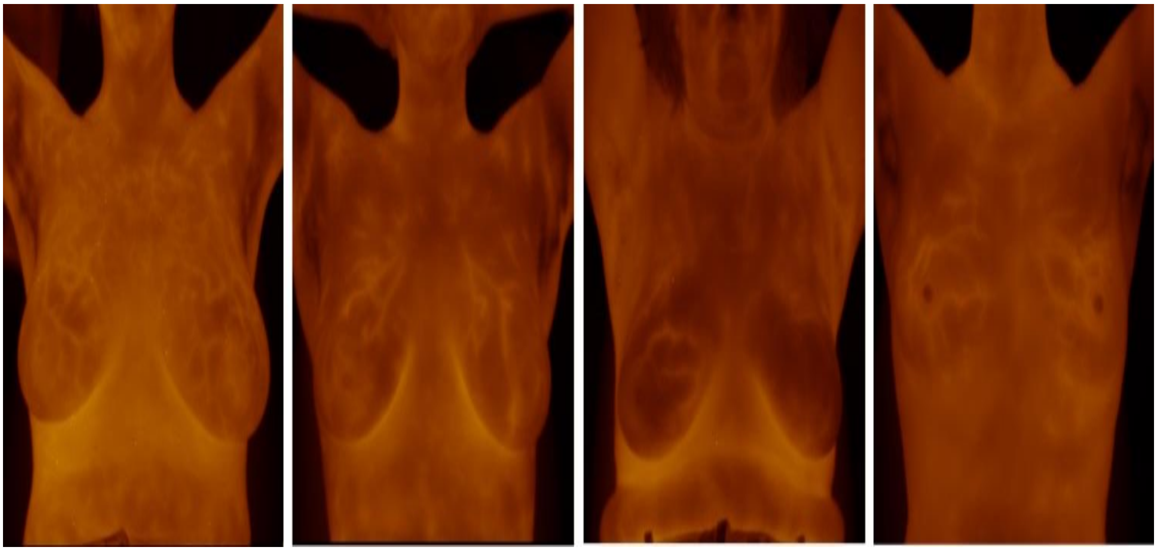

(Subject 1) (Subject 2) (Subject 3) (Subject 4)

Figure 2.1. Current frame belonging to all the subjects are presented. Each subject is acquired three times, hence in total we are provided with 12 datasets in order to analyse movement of the body through image registration and further spectral analysis.

2.2. Breast Segmentation

After acquisition, in order to reduce the non-desirable artifacts, extra analysis and computational time of the abovementioned algorithms, we segment the region of interest in the each frame of the thermograms. Very few works have been done in this field due to a partially smoothed low frequency components and high degree of noises and artifacts in the thermograms. In the literatures, the thermograms are segmented first by an operator. Then breast quadrants are derived automatically based on unique point of reference, i.e. the chin, the lowest, rightmost and leftmost points of the breast. Recently few works addressing the automated segmentation have been introduced where the identification of asymmetry by deploying Image Segmentation, Pattern Recognition and Feature Extraction are considered as the basic methods to extract the region of interest. There are several ways to performing the segmentation: “threshold-base”, “edge-base” and “region base”.

The most cited work belongs to [26], which the idea is based on the fact that in a relatively symmetric image, a small asymmetry could indicate a suspicious region. Hence, edge base segmentation is performed by first Canny edge detection to identify the four dominant curves in the edge image which is called “feature curves” including the left and right body boundaries and the two lower boundaries of the breast. (Figure 2.2) Then the asymmetry analysis has been performed by two methods of automated breast segmentation and tumor classification on the images where we are interested in the former method in this phase. In this method simply using the Hough transform the parabolic and the lower part of the breast is detected.

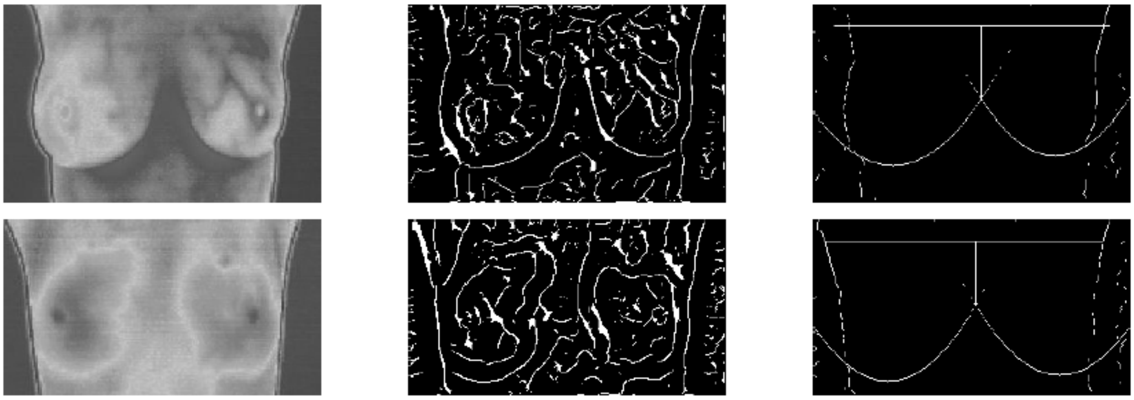

Figure 2.2. Thermal breast segmentation done using edge based method in [12].

There is another work having done by [23], which the use the same edge base semi-automated segmentation while they consider more boundaries of the breast by taking into account the detection of the region with highest curvature in the left and right body edges as well as estimation of the top breast boundary using a number of empirical rules and body regions.

2.3. DAT specific registration methods

We implemented three types of automated linear/non-linear intensity based registration methods. There are properties specified to infrared images which have to be taken into account. Since in thermal images, intensities directly correspond to temperature, hence the similarity metrics must only focus on minimizing the geometric displacement of the pixels directly, instead of the pixel intensities. Therefore, choosing optimizers to minimize the metrics such as MSE of the pixel values ruins the whole registration process, leading to losing information.

2.3.1. Linear Affine registration

First, affine registration algorithm with linear transformation function described by rotation, translation, shearing and scaling of the moving image is implemented in which only global pose differences are compensated. Likewise, Affine method parameterizes the transformation by locally linear deformations [22]. The registration parameters are listed in Table 2.1. Mattes Mutual Information (MMI) is used for similarity measure which is optimized by Gradient Descent (GD) optimization method.

Evaluating the linear registration is significant, since in many applications the sequences are not aligned in phase and single level linear registration could be satisfactory. Therefore choosing a suitable linear registration, satisfies evaluation criteria even prior to a deformable registration and reduces the complexity.

In rigid registration a 6 degree of freedom transformation matrix describes rotation and translation parameters to be applied to the moving image. This means that φ (the transformation function) is parameterized with six numbers: three translation and three rotation parameters. A linear transformation is such that φ can be written as a 3×3 matrix A (9 parameters).

$$\varphi(x) = Ax \qquad \text{(Equation 2.1)}$$

In the affine registration, the transformation matrix has 12 degree of freedom to describe shearing and scaling of the moving image. In this case phi is calculated as

$$\varphi(x) = Ax + b \text{ (Equation 2.2)}$$

(b belongs R^3) [26]. Figure 2.3 depicts the concept of linear affine registration in which the transformation functions only consist of linear transformation that compensate general linear deformations.

Figure 2.3. General concepts of Affine registration in which the transformation functions consist of only linear transformation.

Likewise the previous algorithm, image moments are described as initialization. Evaluating the linear registration along with the non-linear registration could be significant, since in many applications the sequences are not aligned in phase and performing the single level linear registration could be satisfactory in terms of final clinical evaluation. Therefore choosing the most suitable linear registration for an application, might satisfy both technical and clinical evaluation criteria even prior to applying a deformable registration and reduce the complexity and computational time.

The transformation matrix has 12 degree of freedom to describe shearing and scaling. In order to compute a reasonable value for the initial center of rotation and the translation, the initializer is set to use the center of mass of each image as the initial correspondence correction. Centered rigid with 6 degree of freedom transformation matrix describes rotation and translation parameters. The CenteredRigid2DTransform supports two modes of operation. In the first mode, the centers of the images are computed as space coordinates using the image origin, size and spacing. The center of the fixed image is assigned as the rotational center of the transform while the vector going from the fixed image center to the moving image center is passed as the initial translation of the transform. In the second mode, the image centers are not computed geometrically but by using the moments of the intensity gray levels. The center of mass of each image is computed using the helper class ImageMomentsCalculator. The CenteredRigid2DTransform is initialized by 5 parameters, indicating the angle of rotation, the center coordinates and the translation to be applied after rotation. The initialization is done by the CenteredTransformInitializer. The transform can operate in two modes, one assumes that the anatomical objects to be registered are centered in their respective images. Hence the best initial guess for the registration is the one that superimposes those two centers. This second approach assumes that the moments of the anatomical objects are similar for both images and hence the best initial guess for registration is to superimpose both mass centers.

2.3.2. Nonlinear parametric Bspline registration

Next, nonlinear parametric multi-level/multi-resolution Bspline method [23] is implemented and applied. In a multi-level/multi-resolution registration, the idea is to first perform a linear registration to roughly align the frames. Then we exploit the obtained transformation function (bulk transformation) to characterize the further non-linear Bspline registration which consists of coarse grid to cover the global anatomic deformations and fine grid resolution to compensate the local motion with respect to number of Bspline grid points.

Categorizing the methods by the level/resolution of the registration, in a multi-level/multi-resolution registration, the non-linear characterized Bspline registration is followed by the linear registration in order to roughly align the frames, while the non-linear registration part is divided to coarse and fine resolution with respect to number of bspline grid points. The multi-resolution registration helps to localize the final alignment. Cost functions and registration parameters for each method are presented in Table 2.1. For any point x,y,z part of the moving image the B-Spline transformation is computed from the positions of the surrounding 4×4×4 control points.

$$T(x,y,z) = \sum_{l=0}^{3}\sum_{m=0}^{3}\sum_{n=0}^{3} B_l(u) + B_m(v) + B_n(w) CP_{i+l,j+m,k+n} \qquad \text{(Equation 2.3)}$$

Where T is the transformation and i,j,k represents the index of the control point cell containing the point (x,y,z) and u,v,w are the relative positions of point (x,y,z) inside that cell in the 3D space. The control point at a specific location is represented by $CP_{i+l,j+m,k+n}$.

Trans.	Sim.	Opt.	Lvl./ Res.
Affine	[a]MMI	[b]GD	-
Bspline	MMI	[c]LBFGS	Multi/Multi
Demons	[d]GMS	Iterative	Single /Multi

Table 2.1. Classification of cost function exploited for implemented linear and nonlinear registration methods. *Sim.=similarity measure, Opt. = optimization method, Lv1/Res. = Level/Resolution, [a]Mattes Mutual Information, [b]Gradient Descent, [c]Low-memory conjugate gradient descent. [d]Geometric-Mean Squared Error.*

BSpline transformation function characterizes the displacements (indicated by the arrow in Figure 2.4) by defining grids on images, between deformed points on moving image (blue points) and original points on fixed image (red points) [25]. During the registration process, optimization function maximizes the similarity metric priori indicated, in order to obtain the most optimum transformation and appropriately align the images. Cost functions and registration parameters are presented in Table 2.1. We deployed the best combination of similarity metric as MMI and optimization method by minimizing pixel physical disparity using LBFGS optimization method (Table 2.1).

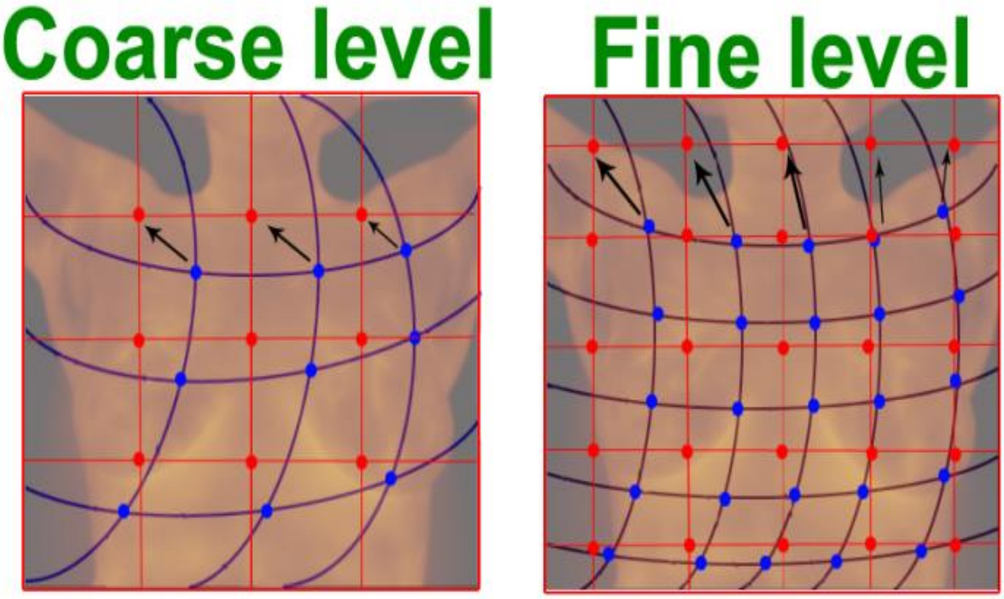

Figure 2.4. Each control points acts as an automated marker on the image. Since it is polynomial it can be derived to N times, and well fits the optimization functions. Number of control points affects the level of registration from coarse to fine grid level. Therefore, it covers the local motion.

The goal of this phase is to properly realign the thermal images composing the sequence to attenuate motion artifacts. Realigning the 500 frames is based on the fact that during the acquisition of the infrared sequence, the patient's breast moves non-rigidly due to physiological (breathing, heart activity, etc.) and random movements. These movements, associated with the thermal gradients of the observed skin surface, generate artifactual fluctuations of the local temperature that, in turn, act as noise superimposed onto the temperature fluctuations to be studied. Likewise, due to respiratory and motion artifacts, the direct comparison of the temperature values that a pixel assumes along the sequence becomes difficult. In fact, the small temperature changes due to blood perfusion, of the order of 10–50 mK, which constitute the signal of interest in the time domain, are superimposed onto large temperature fluctuations due to the subject's motion, which represent noise. Hence, before extracting the time series describing temperature fluctuations, it is fundamental to realign the thermal images to attenuate motion artifacts.[27]

Therefore in this project in order to compensate the patient's movement during the image acquisition, we deployed a Deformable Image Registration (DIR) application to remove the movements. We tried 2 deformable registration methods and 1 linear registration method on the dataset and tested both deformable registration and non-deformable (linear) techniques using automated/non-marker based ITK (Insight Toolkit Algorithm and libraries) [11] and the results shows firstly deformable registration has reached to a better result than the linear or rigid registration due to the deformable movements and the horizontal and vertical curves that we encountered and secondly it is more reliable than the feature based (marker base) registration, since it is done automatic, and does not need human expert intervention. It uses the B-Spline nonlinear transformation to characterize the non-linear deformations on the image to construct the final deformation field which warps/recovers the deformed image. After performing the experiments, the most optimized registration parameters in order to register the 500 frames of thermal breast images are reported in Table 2.2. For registering each frame it takes 2 seconds, thus for 500 frames, it takes 16 minutes on an Intel Centrino 2 core 2.27 GHz CPU and 3GB RAM PC.

Registration Parameters	**Parametric BSpline Deformable Registration**
Number of Iterations of Optimizer	10
Number of Grid control points of Bspline basis function	8
Number of histogram bins on histogram-based similarity metric	100
Time (s)	2 s
Final performance evaluation in term of cross correlation (percentage out of 1)	0.72 / 1.0

Table 2.2. Most optimized registration parameters in order to register the 500 frames of thermal breast images. For registering each frame it takes 2 seconds, thus for 500 frames it takes 16 minutes on Intel Centrino 2 core 2.27 GHz CPU and 3GB RAM PC.

2.3.3. Symmetric diffeomorphic Demons registration

Finally symmetric diffeomorphic Demons registration method is implemented [28]. In the non-parametric demons, by using gradient symmetric forces, the DF is obtained and it is warped onto the moving image, by minimizing the following energy functional:

$$E(s,c) = \frac{1}{\delta_i^2} Sim(F, M^\circ c) + \frac{1}{\delta_x^2} dist(s,c)^2 + \frac{1}{\delta_T^2} Reg(s) \quad \text{(Equation 2.4)}$$

$Sim(F, M^\circ c)$ represents geometric pixel disparity metric of fixed and moving image, $dist(s,c)^2$ considers a correspondence error between transformation c and deformation field s as Gaussian noise, hence as depicted in Figure 2.5 a Gaussian smooth kernel is applied on DF as a regularizer along with smoothness degree of deformation $Reg(s)$ leading to well-posed framework as well as a smoother vector field. δ_i^2, δ_x^2, δ_T^2 maintain the trade-off between the three terms in the cost function. Demons algorithm assumes pixels representing the same homologous point on an object have the similar intensity on both the fixed and moving images, hence well suited for the time-series thermogram registration. Significant parameters are listed in Table 2.3.

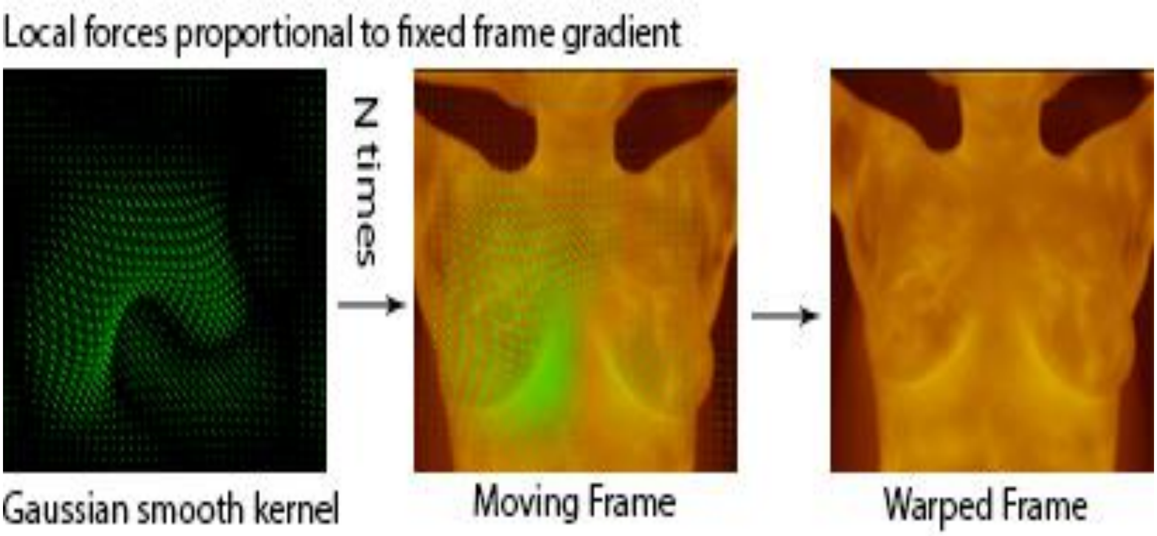

Figure 2.5. First, velocity field is obtained using gradient symmetric forces that is applied on the moving frames to compensate the dissimilarities. Gaussian smooth kernel is deployed as additional regularizer. Fits for time-series sequential thermal registration.

Label	Iteration number	Max step length	Grid points number	Reg. Time (min)
Affine	200	0.1	-	45
Bspline	[a][20, 50]	10	[b](15,30)	15
Demons	40	-	-	15

Table 2.3. Registration parameters. Registrations are performed with Intel Core 2Duo 2.27 GHz CPU, 3GB RAM. [a][linear level, non-linear level], [b](coarse stage, fine stage).

In the non-parametric demons, by using Symmetric Forces registration, the DF is obtained and it is warped onto the moving image while match the histograms between source and target frames. By exploiting multiple level pyramid registration approach, the registration process is fined and localized. The demons algorithm relies on the assumption that pixels representing the same homologous point on an object have the same intensity on both the fixed and moving images to be registered, hence supposed to be well suited for the time-series sequential thermogram registration. Therefore, number of bins where the histogram is matched could be considered as the registration parameters.

2.4. DAT Registration evaluation methods

The fundamental issue for assessing the accuracy of registration relies on quantified comparison of similarity between fixed and moving frames before registration and fixed and warped frames after registration. We implemented three types of the most robust registration evaluation method in order to both quantitatively and qualitatively evaluate the warped 3D thermograms.

2.4.1. DAT specific Breast Boundary Overlap

Aligning the boundaries of the breast correctly is one of the most fundamental expectations of the breast thermogram registration. As a DAT specific evaluation method, "*symmetric alignment of breast boundaries assessment"* of every frame is implemented in order to increase the accuracy and the reliability of the evaluation.

Breast boundaries in all the frames are segmented using Canny Edge Detection and strong gradient in every direction are obtained as a scalar value. Sum of squared differences of gradient values are calculated between fixed frame and every warped frame after registration divided by the number of voxels as breast boundary difference (Equation 2.5).

$$Boundary_{difference} = \frac{1}{n}\sum_{i=2}^{m}(I_{fb} - I_{wb})^2{}_i \qquad \text{(Equation 2.5)}$$

Where I_{fb} and I_{wb} represent gradient values of breast boundary on fixed and warped images respectively, i is the frame number, m is the total number of frames and n is the number of voxels in the images.

Then center of mass (C.O.M) of the image and both left and right breasts were determined. Euclidean distances from C.O.M of the image to C.O.M of the left breast and to the right breast were determined for fixed and every warped frame (see Figure 2.6). Eventually, as shown in Equation 2.6, sum of squared error of the C.O.M distances between fixed and warped frames are obtained as center-of-mass difference.

$$COM_{distance} = \frac{1}{n}\sum_{i=2}^{m}\left[\left(I_{fR} + I_{fL}\right) - \left(I_{wR} + I_{wL}\right)\right]^2{}_i \qquad \text{(Equation 2.6)}$$

Above I_{fR} and I_{fL} represent Euclidean distance of right and left breast from the C.O.M of the image respectively for the fixed frame and the same variables are defined for warped frames as $I_{wR}\ and\ I_{wL}$.

Finally as stated in the following equation, absolute difference of the two latter parameters determined the measurement of breast boundary overlap (BBO) as which the final value should be close to zero.

$$Breast\ Boundary\ Overlap[I,W] = \left|COM_{distance} - Boundary_{difference}\right| \qquad \text{(Equation 2.7)}$$

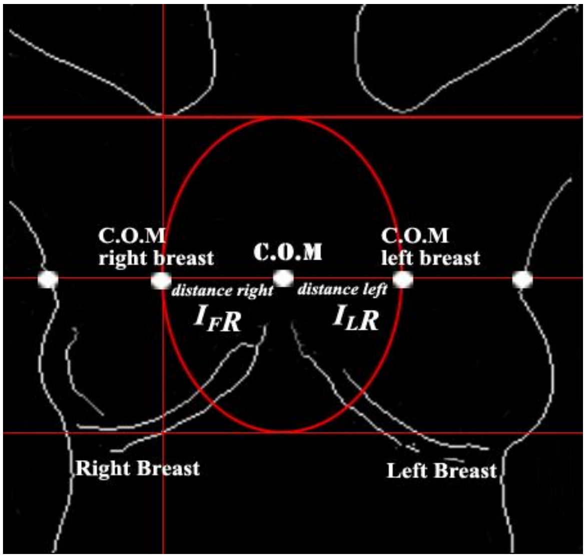

Figure 2.6. A schematic view of how to obtain Breast Boundary Overlap as one of the DAT specific evaluation metrics is depicted. C.O.M stands for centre of mass which are calculated for the whole image and each left and right breasts.

2.4.2. Normalized Mutual Information

Image difference residual is calculated via Normalized Mutual Information (NMI) to evaluate the correspondence of fixed and all the moving frames for all the sequentially warped thermograms. Using the {JoinImageFilter} we can obtain joint histogram of each image at first and then by calculating the joint entropy among two images, the mutual information is obtained. By simply adding entropies of each image and subtracting it from the joint entropy we can obtain mutual information. [30]

Mutual Information = Entropy of image1 + Entropy of image2 – Joint Entropy

For evaluation of our second data type of clinical patients we use Normalized Mutual Information (NMI), where the value of Mutual Information gets divided by the mean entropy of the input images as follows:

Normalized Mutual Information =
2.0 * (Mutual Information) / (Entropy of image1 + Entropy of image2)

2.4.3. Jacobian determinant of the transformation

In order to analyze how physically logic the registration method is, an application to obtain minimum Jacobian determinant of the transformation (Deformation Field) for each warped frames of the sequences is implemented [31]. This metric investigates on the singularities of the DF. If Jacobian value for each point is smaller than 1 local contraction has taken place and all the points are singularities in the DF, indicating the irregularities in the transformation [32]. Hence, the overall percentage of negative Jacobian values on all the sequential DF is obtained as a quantitative evaluation metric. The Jacobian matrix is second order matrix of the deformation.

$$J_{\varphi}(x) = \begin{matrix} \frac{\partial \varphi_1(x)}{\partial x_1} & \frac{\partial \varphi_1(x)}{\partial x_2} & \frac{\partial \varphi_1(x)}{\partial x_3} \\ \frac{\partial \varphi_2(x)}{\partial x_1} & \frac{\partial \varphi_2(x)}{\partial x_2} & \frac{\partial \varphi_2(x)}{\partial x_3} \\ \frac{\partial \varphi_3(x)}{\partial x_1} & \frac{\partial \varphi_3(x)}{\partial x_2} & \frac{\partial \varphi_3(x)}{\partial x_3} \end{matrix}$$

The Jacobian matrix encodes the local stretching, shearing and rotating of the deformation field. Useful measures that can be derived from the matrices are the determinants, which indicate relative volumes before and after spatially transforming. A region of negative determinants would indicate that the one-to-one mapping has been lost.

If φ_c is the deformation that results from the composition of two deformations φ_B and φ_A (i.e. $\varphi_c = \varphi_B.\varphi_A$), then the resulting Jacobian field can be obtained by the matrix multiplication $J\varphi_C = (J\varphi_B.\varphi_A)\, J\varphi_A$. This leads to a similar scaling and squaring approach that can be used for computing the Jacobian matrices of deformations.[33]

In practical approach we have written a program to evaluate the jacobian determinant of each voxel of our final deformation fields using two following ITK filters.

itk::DisplacementFieldJacobianDeterminantFilter<DeformationFieldType, PixelType>

Computes a scalar image from a vector image (e.g., deformation field) input, where each output scalar at each pixel is the Jacobian determinant of the vector field at that location. This calculation is correct in the case where the vector image is a "displacement" from the current location. The computation for the jacobian determinant is: $\det\left[\frac{dT}{dx}\right] = \det[I + \frac{du}{dx}]$. [33]

itk::MinimumMaximumImageCalculator<ImageType>

This calculator computes the minimum and the maximum intensity values of an image. It is templated over input image type. To compute Maximum or Minimum value ComputeMaximum() (ComputeMinimum()) functions can be called, otherwise Compute() will compute both. [33]

This application is based on [33] and it calculates the jacobian determinant of the first partial derivative of the transformation. It computes the minimum and maximum jacobian value in the whole vector field so that we can figure out whether we have any negative jacobian value for any voxel or not. It also computes the percentage of voxels which its jacobian is less than 1, more than 1 or equal to 1. It also gives us the final jacobian image applied on the vector field. (Figure 2.7)

In a Deformation Field, Jacobian values near 1 shows no local volume change in term of quantification and in the jacobian image it is in grey, values lower than 1 show volume decrease and are dark grey to black, and values above 1 (volume increase) are light grey to white. [33]

If we have the bigger percentage of jacobian values equal to 1 in any vector field, it might be more consistent, non-singular and invertible. Also in term of minimum jacobian value in the jacobian image, the positive and bigger number we have, the smoother deformation we will obtain. That is because we go far away from the zero and negative values. In contrast in term of maximum jacobian value the smaller number we have the smoother vector field we will expect.

This application is very useful, since using this application, user can brightly obtain the ability of the invertibility of its final deformation field and it shows to the user the potential of having negative jacobian in the transformation which help for the final evaluation of the deformation field.

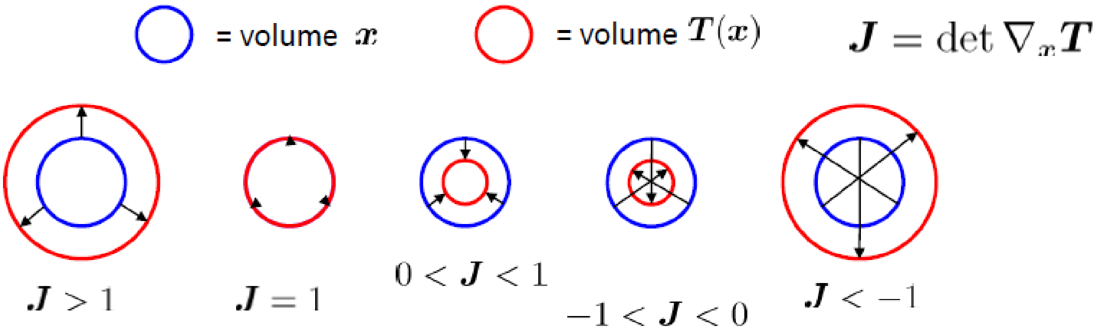

Figure 2.7. Volume increase, decrease and no volume change after evaluating Jacobian determinant of the final deformation. [33]

Chapter 3 : Results

3.1. Comparing the implemented methods

In table 3.1, the results for every subject are summarized. The average NMI for Affine, BSpline and Demons registration applied on the entire subject is 0.70±0.03, 0.74±0.03 and 0.81±0.09 respectively (out of 1). Also average BBO for Demons registration was 0.026±0.006 (smaller better) which is the lowest and close to zero among the methods.

In the last column of table 3.1, percentage of negative Jacobian values for each method applied on the entire subject is presented in which for Demons method the whole values are zero indicating that the smoothness of DF is guaranteed.

In order to statistically assess the difference between each obtained results, we performed nonparametric Friedman test evaluating both BBO and NMI for every method. Both metrics have chi-squared values equal to 20 ($P<0.001$, df = 2), that rejects the null hypothesis and proves the existence of large difference among the results. To figure out where the critical difference in the results from three methods resides, a Post-hoc analysis is also performed through an inter-subject evaluation presented in Figure 3.1 in which for each method, distribution of errors with respect to all cases is shown. The latter figures indicate the significant difference that exists among the group of results, belongs to Demons registration, which acts as the best method for thermogram time-series registration.

Metrics	AVG-BBO			AVG-NMI			AVG-JAC		
Subjects/Methods	^{a}Aff.	^{b}Bsp.	^{c}Dem.	Aff.	Bsp.	Dem.	Aff.	Bsp.	Dem.
Subject1_1	0.063	0.11	0.036	0.68	0.68	0.79	4.20	0.4	0
Subject1_2	0.067	0.07	0.025	0.67	0.73	0.80	4	3	0
Subject1_3	0.059	0.08	0.029	0.71	0.75	0.81	3.8	0.2	0
Subject2_1	0.074	0.066	0.025	0.72	0.76	0.81	10	1.2	0
Subject2_2	0.076	0.035	0.030	0.67	0.73	0.80	7	4	0
Subject2_3	0.088	0.068	0.025	0.70	0.75	0.82	4.3	0	0
Subject3_1	0.053	0.054	0.023	0.67	0.72	0.81	7.8	3.8	0
Subject3_2	0.09	0.061	0.031	0.73	0.76	0.82	8	0.9	0
Subject3_3	0.072	0.042	0.032	0.75	0.77	0.81	10	1	0
Subject4_1	0.069	0.056	0.028	0.75	0.77	0.81	3.2	2.9	0
Subject4_2	0.069	0.066	0.011	0.73	0.75	0.82	2.1	0	0
Subject4_3	0.066	0.037	0.022	0.7	0.77	0.82	5.9	1.1	0
Average	**0.07**	**0.062**	**0.026**	**0.70**	**0.74**	**0.81**	**5.85**	**1.54**	**0**
Standard Dev.	**0.01**	**0.02**	**0.006**	**0.029**	**0.026**	**0.009**	**2.66**	**1.47**	**0**

Table 3.1. Quantitative numerical values resulted from each registration method are presented here for every subject. Average NMI and BBO values obtained from all the frames of each subject proves that Demons method is pioneer in terms of both similarity of the warped frames as well as smoothness of DF indicated by absence of negative Jacobian value. Likewise, small value for standard deviation in the Demons method obtained from all the metrics proves that diversity in the results is very small. ^{A}Affine, ^{b}Bspline, ^{c}Demons

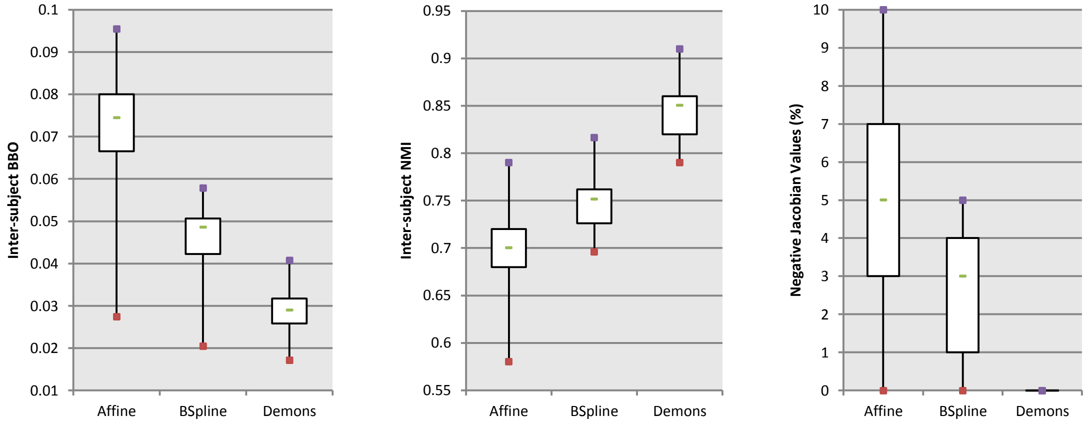

Figure 3.1. In order to perform a Post-hoc analysis for nonparametric Friedman test (*P*<0.001, *df* = 2), box plots representing distribution of errors on the obtained results from provided metrics for all the methods (inter-subject evaluation) are presented. The analysis shows there is a critical difference in the groups of Demons method for every experiment acting as the best method in our experiments.

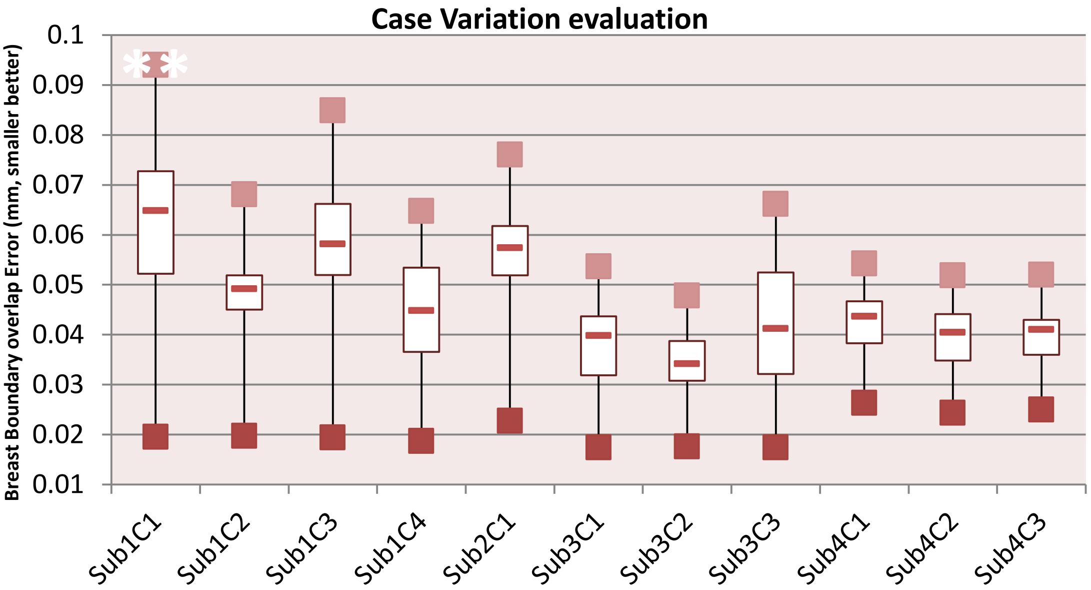

Figure 3.2. Case variation error on all the methods performed on all the cases.

Based on breast boundary overlap error, we evaluate how well the dynamic frames of each case within the subjects are aligned apart from the registration method. Hence the distribution of the errors belonging to all the methods performed to each individual case is assessed, helping to know which case has the least movement and better recovery. Figure 3.2 shows the error distributed on each case.

Label	Intra-Subject			Inter-Subject		
	Avg NMI Error	Avg Breast Boundary	Avg Singularity error	Avg NMI Error	Avg Breast Boundary	Avg Singularity error
Affine	0,68	0,13	14%	0,69	0,14	7.6%
BSpline	0,75	0,043	7%	0,75	0,044	3.5%
Demons	*0,85*	*0,0013*	*0%*	*0,84*	*0,0011*	*0%*

Table 3.2. Intra-subject and inter-subject overall results obtained from registration methods on all the cases.

In the table above, we summarized the Intra-subject and inter-subject overall results obtained from registration methods on all the cases. As can be seen, Demons method excels in all the evaluation methods with 0% of negative jacobian values and average breast boundary overlap close to zero.

3.2. Pre and Post Registration comparison

As mentioned in the previous section, in thermogram registration the criteria are to evaluate each moving frame both in terms of image similarity and anatomical consistency of the transformation with respect to the fixed frame. We evaluated BBO and NMI for every frame of only subject 1 and 2 (Figure 3.3 and 3.4) for the sake of comparison between before and after registration. Figure 3.3-(a) shows BBO error metric obtained from affine registration applied on Subject 1 (top row) and Subject 2 (bottom row). Also for Panel (b) and (c) the same metric is used to assess the results from Bspline registration and Demons method respectively. Demons method has the lowest values for every frame of both subjects with smoothly distributed values.

On the other hand, Figure 3.4 Panels (a), (b) and (c) present the result on the same subjects (top and bottom row) for NMI values resulted from Affine, Bspline and Demons method respectively. Similar to BBO, Demons method excels for NMI values with the highest and smoothest distribution of the values. These results coincide to the quantitative results in table 3.1.

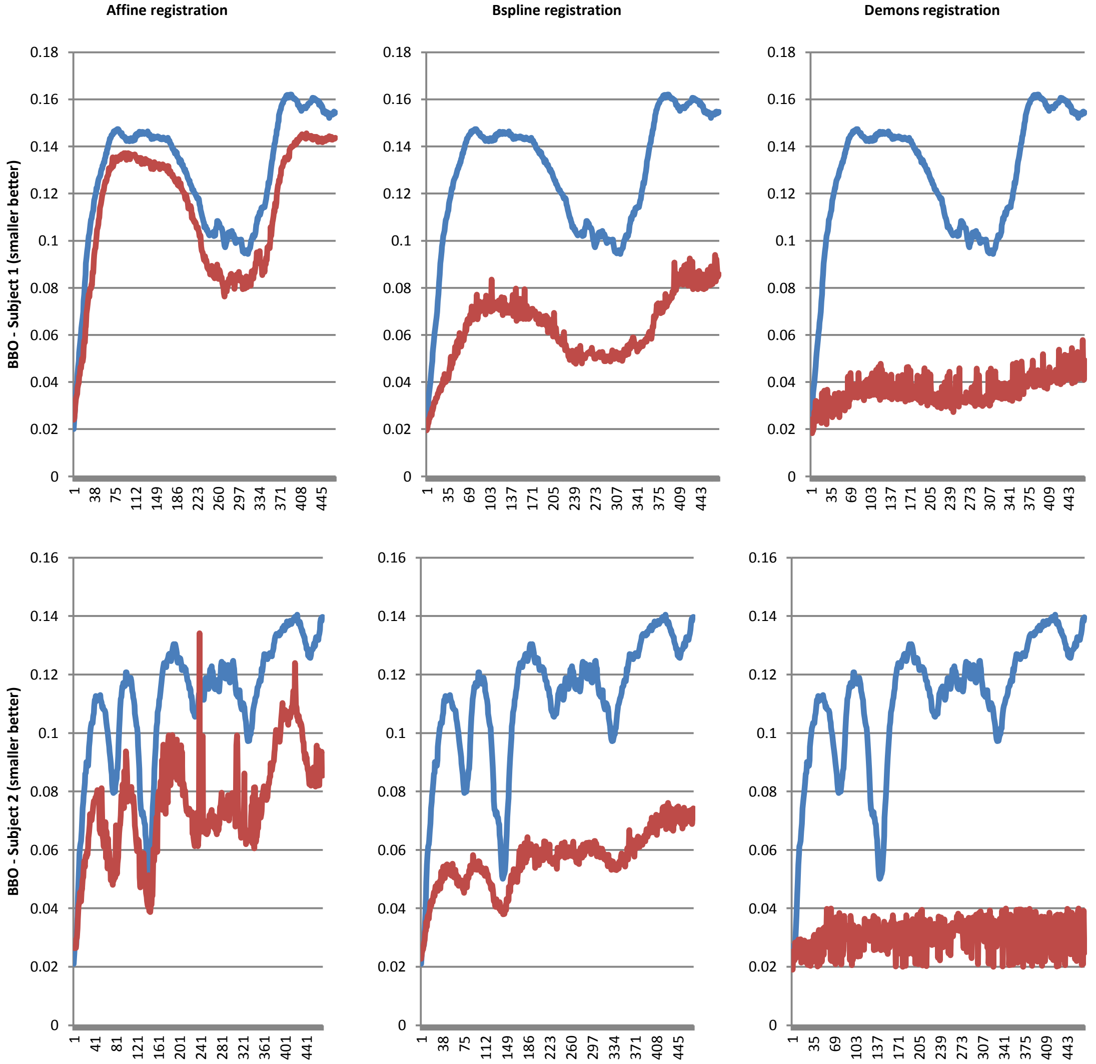

(a) (b) (c)

Figure 3.3. BBO metric is used to evaluate and compare each method applied before (blue line) and after (red line) registration for every frame belonging to Subject 1 (top row) and Subject 2 (bottom row). X axis represents number of frames from 1 to 476 and Y axis represents BBO error values (smaller better). Evaluated methods are presented as Affine, Bspline and Demons respectively from left to right for panels (a), (b) and (c). Demons method shows the lowest differences error for BBO comparing to other methods.

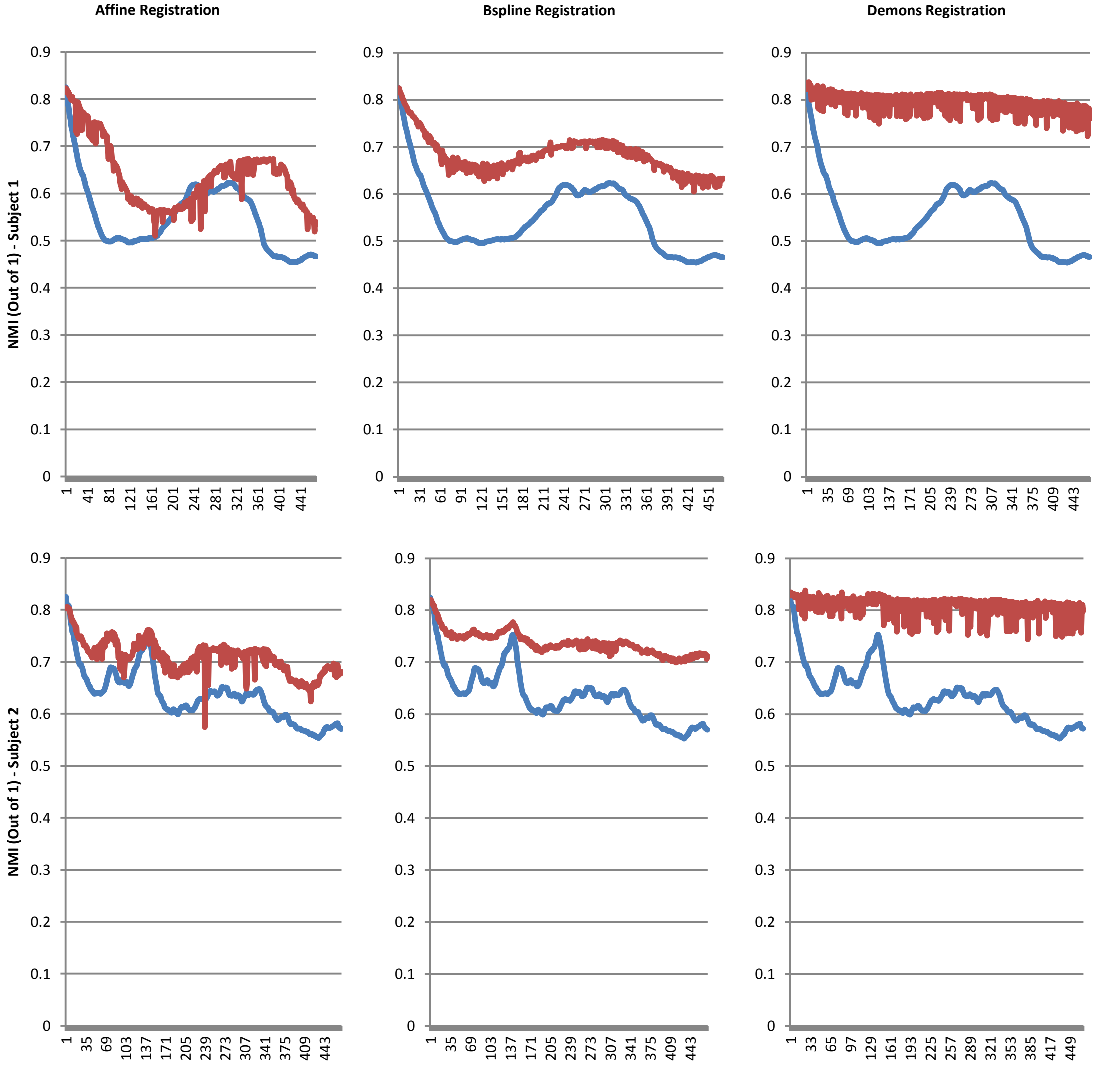

(a) (b) (c)

Figure 3.4. Same as Fig. 3.3, here NMI metric is used to evaluate and compare each method applied before (blue line) and after (red line) registration for every frame belonging to Subject 1 (top row) and Subject 2 (bottom row). X axis represents number of frames from 1 to 476 and here Y axis represents NMI values (larger better). Evaluated methods are presented as Affine, Bspline and Demons respectively from left to right for panels (a), (b) and (c). NMI values for Demons registration is the highest comparing to the others, and the values for each frame is stable.

3.3. Spectral analysis of temperature modulation

The goal in this phase is to obtain final Power Spectral Density (PSD) image. Information on the local blood perfusion is obtained from the spectral analysis of the time series at each image pixel. In spectral analysis of thermograms, the range of frequency which is analyzed is between 0.1 Hz and 1 Hz. The former 0.1 Hz frequency belongs to the vasomotor frequency, change in diameter of the blood vessels caused by vasodilation and vasocontsrictions in the arteries and arterioles. The latter frequency 1 Hz is the heart rate called cardiogenic frequency.[34] Those are in very low-frequency range, shows the change in the temperature is very low and sudden change in frequency must be captured during the frames. In order to obtain the final 2D PSD image, the following sequential methods are applied on the registered thermograms:

1- First two pre-enhancement filtering are applied on each frame of the image: Median and Average filtering in order to remove the noises and smooth the image while preserve the high frequency components of the image.

2- For each pixel of each frame, we filter the signal using Yulewalk low pass Infinite Impulse Response (IIR) filter with order of 15 and cut-off frequency at 10 Hz, (changes the amplitude of each frequency components) removing mean value and make PSD estimation using classic periodogram. We use sampling frequency of 50 Hz and 512 number of FFT points to calculate the PSD estimate. Likewise in order to preserve the phase of the frequency components which changes the time order of the samples from forward to backward, we use Zero-Phase filter to prevent the phase disorders.

3- Then we compute the FFT on the intensity/temperature-time series of the pixels to obtain the fluctuation/changes in the temperatures and indicate the high/low frequency components of the frames. Finally we estimate the PSD, out of computed FFT of every corresponding pixels belonging to all the frames. In this part, we apply band on the frequencies to which the PSD is computed. As mentioned the band is from 0.1 Hz to 4 Hz, which we consider the ambient noises as well. PSD can be computed as the Square Magnitude of FFT scaled spectrum divided by the sampling period (Periodogram).

   If we calculate PSD for every row of the frequencies, we obtain a PSD based 2D image as shown in the last part.

After obtaining PSD image, there are several aspects/components/parameters regarding the thermal spectral analysis of the obtained thermograms which could be analyzed and evaluated in order to “detect” cancerous region/Tumor detection or to estimate the tumor contour from the breast skin surface temperature or any other tumor parameters.

In the final PSD image, the difference of the suspicious region/lesion/cancer and the artifacts cannot be well distinguished. Both belong to high frequency component of the image but in different domain. The suspicious region belongs to high frequency, due to sudden change in the temperature of the region and because of the vast frequent change in the temperature during the acquisition time. Motion artifacts are then particularly relevant in areas in which a strong spatial gradient of temperature is present. Distinguishing the latter two objects is considered as an issue.

Skin temperature fluctuations affect the signal of interest, thus applying registration on dynamic thermogram images improves the spectral analysis of temperature modulation and reduces percentage of false positive in the further diagnosis. PSD images are used for prognosis of breast cancer in which the high frequency components of the temperature values are highlighted. We obtained information on the local blood perfusion from the spectral analysis of the time series at each image pixel on Subject1-case1 by means of comparing the final spectral image with and without applying registration as shown in Figure 3.5. The range of analyzed frequency is between 0.1 Hz (vasomotor frequency) and 1 Hz (cardiogenic frequency) [34]. High frequency components of the image, where the power of the time-temperature signal is higher due to larger temperature fluctuation, is highlighted by dark red (Figure 3.5-a). On the contrary, spots with lower temperature modulation indicating smoother signal without unnecessary noises is shown in lighter blue (Figure 3.5-b).

Followed by the PSD image, Time-temperature signal belonging to an arbitrary spot before and after registration is also shown in Figure 3.6. Y axis represents temperature in the previous spot which is equal to down quantized pixel intensity values.

Non-registered signal in the left panel shows a great variation in the temperature values ranging from 0.6 to 0.7 during 10s acquisition, showing a huge fluctuation. However in the right panel after registration, the vertical axis has been magnified in order to emphasis that the signal is quite stabilized with a lower frequency and the intensities alter in a smaller scale between 0.61 and 0.62.

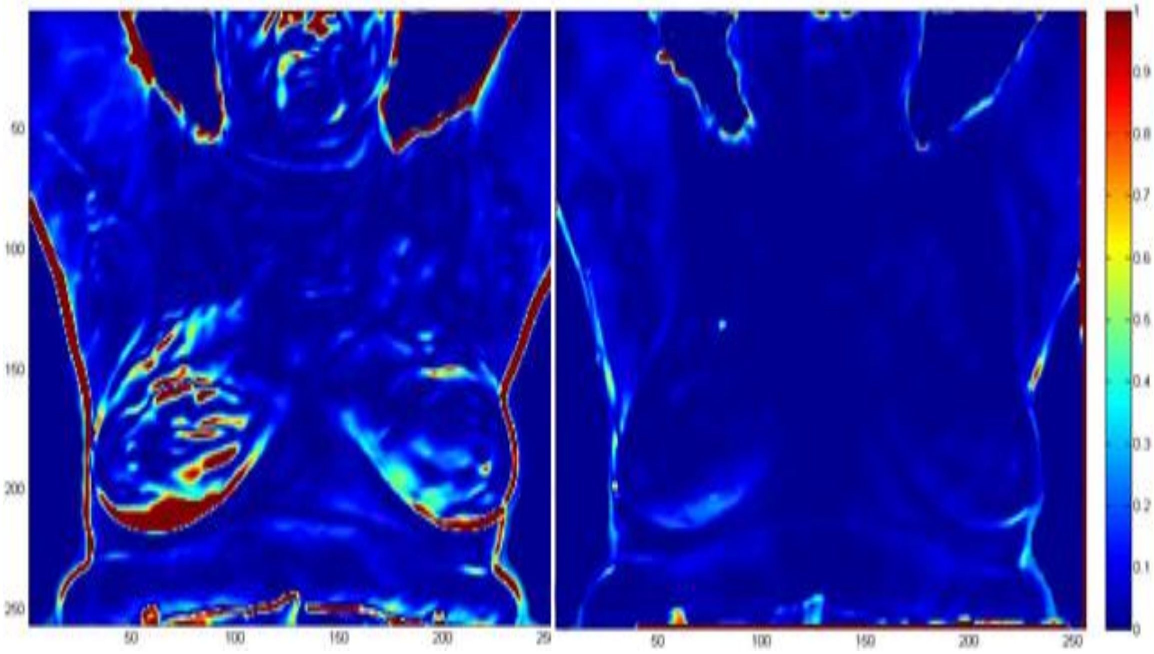

(a) (b)

Figure 3.5. Final 2D spectral image obtained from PSD values of each pixel without (a) and with (b) registration. High frequency components of the temperature values for every pixel is shown as darker red and low frequency component with lighter blue. Unnecessary noises are removed after registration (b), leading to a smoother image that helps in the further diagnosis.

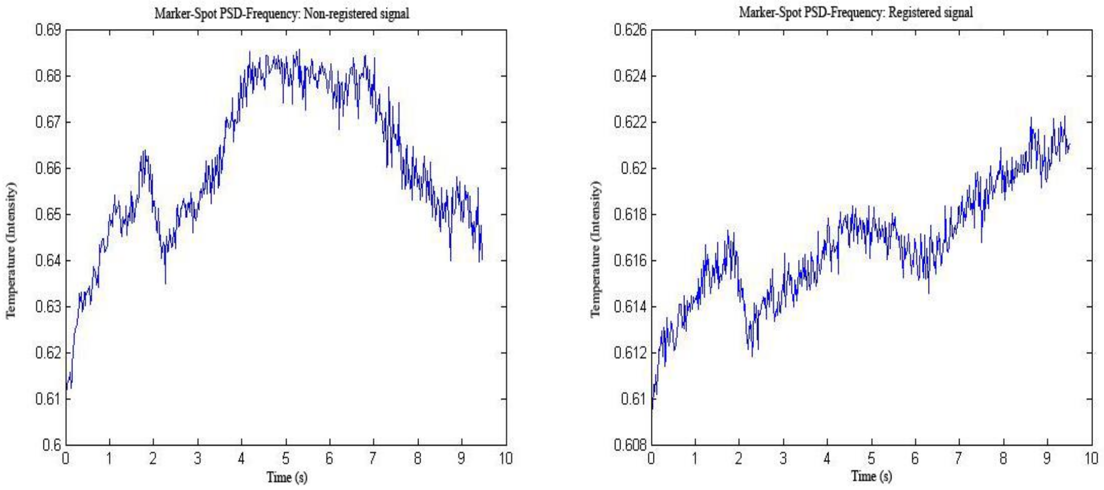

(a) (b)

Figure 3.6. Time-temperature series of an arbitrary spot in Subject1-case1 belonging to before (a) and after (b) registration. Acquisition time is 10s and vertical axis for panel (b) has been magnified in order to emphasis that the scale of temperature variation is smaller after registration.

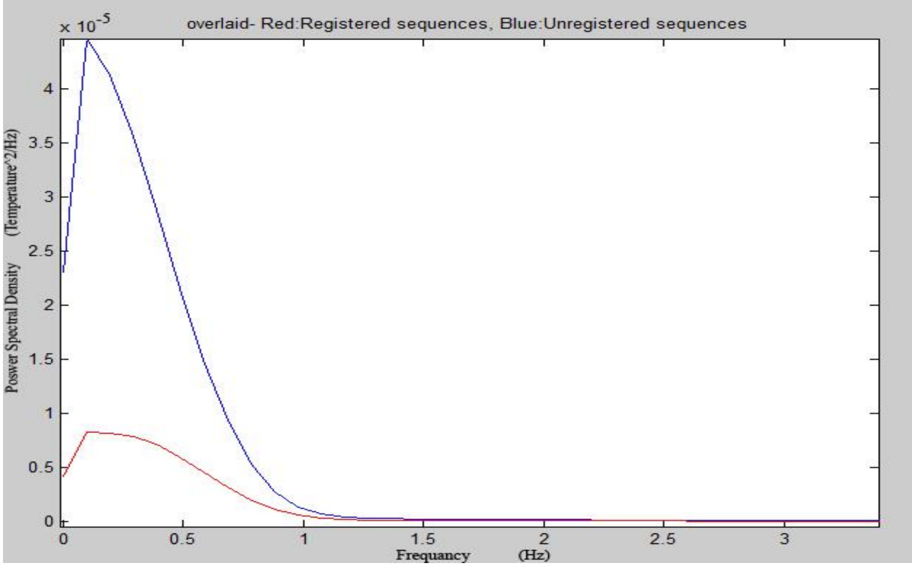

Figure 3.7. PSD-frequency graph of the latter time-temperature series for with (red) and without (blue) registration are overlaid. As expected, frequency range is limited between 0.1 and 1 Hz and PSD values for the registered signal has lower peak thus more stabilized comparing to non-registered curve.

Finally in Figure 3.7, PSD-Frequency curve of the latter time-temperature signal belonging to before and after registration is overlaid for the sake of comparison. Peak of the PSD value for registered signal is lower and smoother comparing to the nonregistered signal showing lower power of the frequency component of the signal leading to stability and constancy in the temperature oscillation during time variation.

Chapter 4 : Discussion and Conclusion

4.1. Discussion

The frequency of the any pixel (modulation change), could be staying static and we have the phase shift or out of phase condition. Could be initial frequency angel of the sinusoidal wave and we only have change in the angel. We have geometric changes, not change in the distance.

$$x(t) = A.\cos(2\pi f t + \varphi) \qquad \text{(Equation 4.1)}$$

$$y(t) = A.\sin(2\pi f t + \varphi) = A.\cos(2\pi f t + \varphi - {}^{\pi}/_{2}) \quad \text{(Equation 4.2)}$$

Considering the temperature in a point at a given time, total derivative of temperature with respect to time is proportional to velocity of skin portion, hence Demons method, calculates the 2D velocity in the image, approximating image motion from sequential time-ordered images, which also guarantees the similarity of warped frames.

Demons method computes a deformable registration based on intensity changes and is derived from the work by Thirion10. The registration is driven by the concept of optical flow and was initially used in computer vision research. Optical flow calculates an image velocity approximating image motion from sequential time-ordered images. The demons algorithm is based on gradient calculations from the fixed image to determine the demons force required to deform the moving image. The diffusion model assumes that so-called “demons” at every voxel from the fixed (reference) image are applying forces that push the voxels of the moving image into matching up with the fixed image.

The inputs to the registration are a moving image m and a fixed image f. We assume that f and m are consecutive “snapshots" of an image function I(x,y,z,t) for which the brightness values of corresponding anatomy are constant. Explicitly including time as a variable gives

I(x(t),y(t),z(t), t) = constant

and f = I(x(t0),y(t0), z(t0), t0), m = I(x(t1),y(t1), z(t1),t1). The optical flow velocity can then be written as

$$\vec{v} = \frac{(m-f)\vec{\nabla} f}{\left|\vec{\nabla} f\right|^2 + K^2(m-f)^2} \qquad \text{(Equation 4.3)}$$

In optical flow, v is considered to be a velocity because the images are two successive time frames; v is the displacement during the time interval between the two image frames. f ∇r represents the relationship between the neighboring points in the fixed image (such as an edge), K is the reciprocal of the diagonal of a pixel (units of 1/mm) and the (m-f) term represents the differential force of the interaction between the fixed and the moving images.

Equation (4.3) is calculated iteratively; after each iteration, the optical flow computation is followed by regularization of the deformation field using a Gaussian filter.

In order to qualitatively evaluate the methods, Figure 4.1 illustrates the sequential final DF obtained for Subject1-case1 overlaid on the warped frames. Comparing the DF in each method, vectors in affine registration shows a disordered and irregular pattern conveying misalignment and failure in compensating the physical distance of corresponding points. Likewise, movements of the lower part of the body have not been compensated and remain in the same structure.

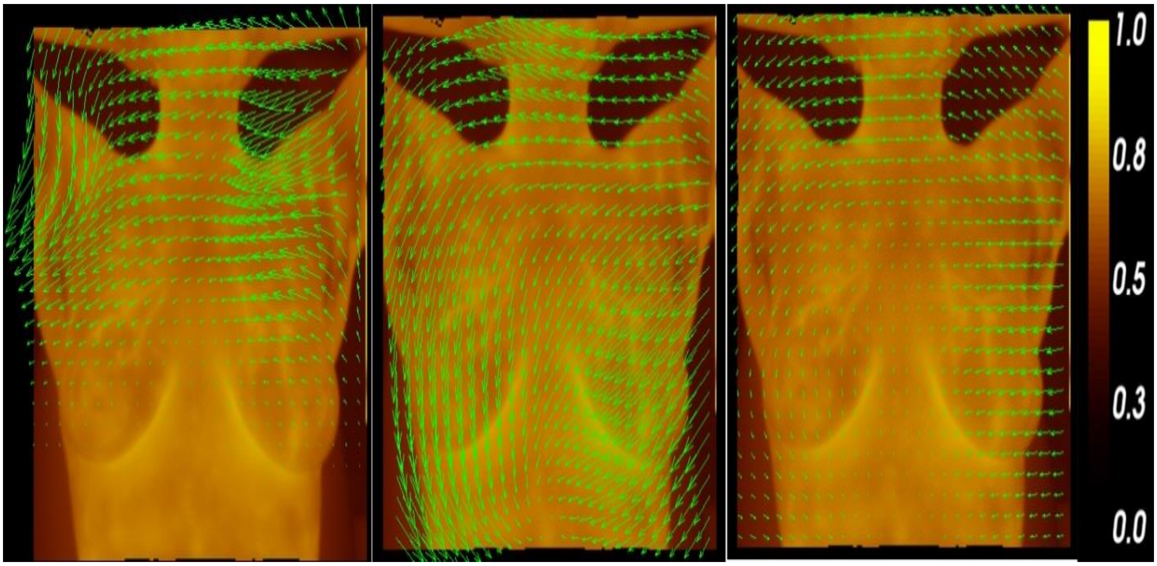

(Affine) (Bspline) (Demons)

Figure 4.1. DF overlaid on warped images belonging to current frame of Subject1-case1, in order to show the smoothness of final DF yielded for each method. Demons resulted with the least irregularity in DF along with the shortest vectors of displacements proving that misalignment of the warped frames is well compensated.

This is because nonlinear deformation of the body movement is neglected and transformation mapping of two images only contains straight lines and points leading to compensation of only rigid body motion.

However in Figure 4.1, vectors in Bspline registration have covered movements in every part of the body, although there are unorganized directions as well as large magnitudes of the vectors due to the fact that image similarity function does not uniquely determine the correspondence between two image volumes. Here despite of developing multi level/resolution registration to keep the localization during the process, however similarity cost functions have many local minima due to the complexity of the images being matched and the dimensionality of the transformation [22]. The latter issue leads to uncertainty in the physiological consistency of deformation between two images. The problem is usually resolved by including a regularization function into the cost function in order to reduce the irregularities in the deformation field.

Demons registration has resolved both latter problems and yielded smaller BBO error and higher NMI values (Figure 3.4). Basically in Demons algorithm, histogram matching is very crucial since we could have different scales of gray levels between the reference frame as the very first frame and the further frames with large movements. Hence, it assumes that the corresponding points on both images remain the same intensity value which acts significant in application of DAT breast cancer detection where temperature parameters play the main role.

DF in the Demons method is the smoothest comparing to other methods, due to the fact that considering the temperature in a point at a given time, total derivative of temperature with respect to time is proportional to velocity of skin portion [22]. Demons method, calculates the 2D velocity in the image, approximating image motion from sequential time-ordered images, which also guarantees the similarity of warped frames. Moreover, it computes optical flow at every pixel and assumes motion displacement but no intensity error, and uses Gaussian kernel to smooth the deformation field after each iteration.

$$\frac{\partial T}{\partial t} = \frac{\partial T}{\partial t} + (\vec{v}.\nabla)T \quad \text{(Equation 4.4)}$$

$$\vec{v} = \frac{(I_m - I_f)\nabla I_f}{|\nabla I_f|^2 + (I_m - I_f)^2} \quad \text{(Equation 4.5)}$$

Equation 4.3 shows that Change of Temperature is proportional to velocity of the skin portion and Equation 4.4 demonstrates Velocity field applied on moving frames by Demons method.

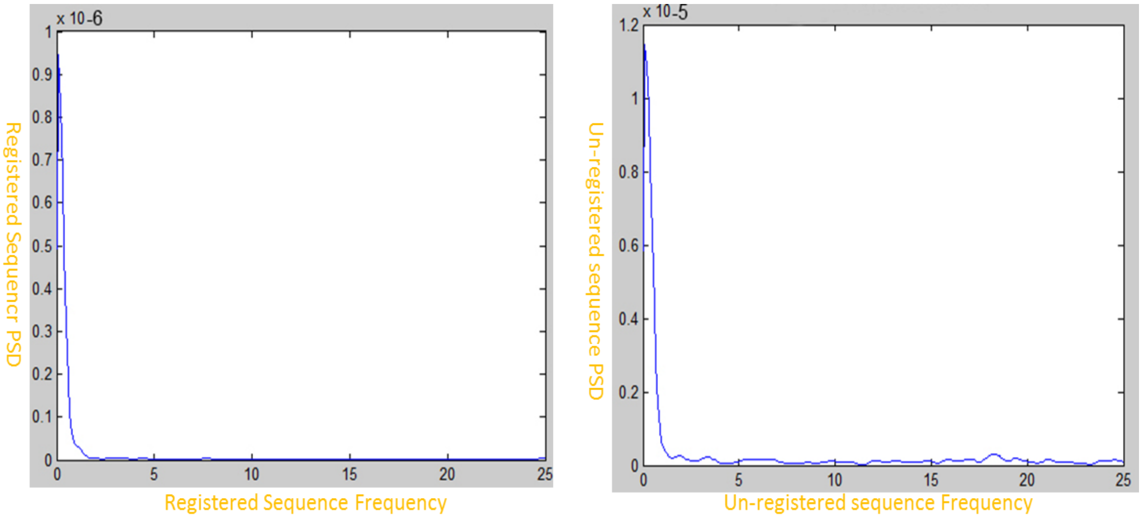

(a) (b)

Figure 4.2. Obtained Power Spectral Density and frequency series of a random point comparing the stabilization before (b) and after the registration (a).

In the above figure we obtained Power Spectral Density and frequency series of a random point comparing the stabilization before (b) and after (a) the registration. Stabilized PSD-frequency curve before the registration represents smoother curve with less irregularities while unnecessary noises are removed due to lower distribution of power over the confined frequency range thanks to stabilization conducted by image registration.

Eventually, we can deduce that the main criteria to obtain the best warped frames similarity and smoothness of deformation fields in a 3D time-series dynamic breast infrared images are dependent upon the local geometric variations of the images as well as the registration parameters. In terms of pre and post registration comparison by means of spectral analysis of the temperature modulation, vessel modulation has very low-frequency range limited between vasoconstriction, vasodilation and cardiogenic frequency; hence sudden change in frequency due to movement of the body as well as ambient noises must be captured through the frames. Obviously, in the registered image (Figure. 4.2-a), temperature fluctuation of each point is less on the time-series frames, leading to smoother spectral image with less irregularities while unnecessary noises are removed due to lower distribution of power over the confined frequency range thanks to stabilization conducted by image registration.

We believe implementation of marker-less 3D time-series registration algorithms and finding the most optimized registration parameters specifically for dynamic infrared images which has not been done before can ease the patient acquisition procedure by making it user-independently and compensate the patient movement as well as ambient noises; thus clearer time-temperature signal of interest can be transformed for the advance spectral analysis of temperature modulation for the following breast cancer prognosis. It is expected that registration strategy and its characteristics introduced in this paper, plus the obtained results may be used in future design optimization of many DAT framework and DIRI applications.

However there are some limitations on the implementation and deployment of the algorithms. The major problem resides on the complexity of the methods in terms of implementation. Considering each method, large numbers of parameters are involved e.g. number of histogram bins of MI as similarity metrics, max/min step length of the optimization functions and cost function convergence tolerance. This issue makes the procedure nontrivial. Likewise, there is a computational burden during the deployment of the implemented methods, thus in some points a parameter tuning is required in order to reduce the calculation cost. For this purpose porting the implementation from CPU to GPU enabled environment can advance computational pace.

4.2. Conclusion

Respiratory motion can be a significant effect when applying breast infrared thermography. Manual marker-based registration methods have been used in the previous works to resolve the patient movement along with ambient noises during the thermogram acquisition, but there are drawbacks e.g. difficulty in manually placing the markers, optimal number of markers obstructing the acquisition procedure. Likewise, unnecessary noises in the time-temperature signals lead to inaccurate further spectral analysis of the temperature modulation.

We implemented time-series image registration techniques in ITK, comprising linear affine and nonlinear Bspline as well as Demons registration method. The methods are both quantitatively and qualitatively validated by robust evaluation metrics, i.e. Normalized Mutual Information, Breast Boundary Overlap and Jacobian determinant of the transformation. Spectral analysis is also performed to compare the signals of time-temperature series on each pixel before and after registration. Based on the results along with nonparametric Friedman test and the further Post-hoc analysis, we deduced that Demons registration due to homologous symmetric forces enforcing the pixel geometric disparities to be shortened on all the frames, excelled in terms of both frame similarity and smooth DF, comparing to other methods. Likewise, registered spectral image was smoother because of stabilized noiseless low frequency components of each pixel that helps in the further prognosis of breast cancer.

Finally, obtaining optimal DAT registration parameters is considered as a future work.

THIS PAGE WAS INTENTIONALLY LEFT BLANK

Section 2: Preoperative Computer Aided Diagnostic System for Carotid Artery Stenting simulation using Finite Element Analysis

Chapter 5 : Introduction to Carotid Arterial Stenting

5.1. Calcified carotid atherosclerotic plaque and Agatston score

Understanding mechanical and material behavior of arteriosclerotic cardiovascular disease in terms of both atherogenesis and thrombogenesis that lead to ischemic stroke has been in debate. Carotid artery stenting (CAS) of cervical carotid artery stenosis has been increasingly used as an alternative to carotid endarterectomy (CEA). Realizing mechanism of plaque rupture inside intracranial carotid artery in order to predict the pre-operative interaction of plaque/stent/balloon and the arterial wall in an interventional treatment of CAS operation could prevent a high risk of stroke. Histology of atherosclerosis plaques in an advanced stage consist of different layers: fibrous cap, fibrotic intima, calcification, lipid pool and fibrotic media [35], [36]. In this work we specifically focused on carotid calcified plaques extracted from MDCT angiography. Although it has been suggested that calcifications stabilize the plaque fibrous and prevent the rupture [37], however when becomes larger and advanced, it causes plaque break [38]. Presence of calcification inside the fibrous cap indicates a hard and concentric plaque in which alters the mechanical properties of the plaque [39], [40]. Likewise there is a direct relationship between percent area of calcification and volume of plaque thus severity of occlusion [41].Two major problems exist in CAS angioplasty: (i)elastic and small plaques with early calcifications penetrate into the stent leading to “plaque protrusion”. (ii)stiff and large caps which contain advanced calcifications when being pushed by the stent/balloon lead to eventual arterial wall rupture or stent fracture during the operation. Investigation on clinical as well as mechanical behavior of fibrous cap, lipid pools and different arterial layers have been extensively performed [42], [43], however there is lack of probe into association of calcification and physiological phenomena that occurs during the development of atherosclerosis as well as susceptibility of the carotid plaque during CAS angioplasty. The aim of this work is to particularly explore on contribution of calcification in atherosclerotic plaque rupture and to find its maximum resistance when imposed by external pressure load during interventional CAS placement by exploiting Agatston Calcium score.

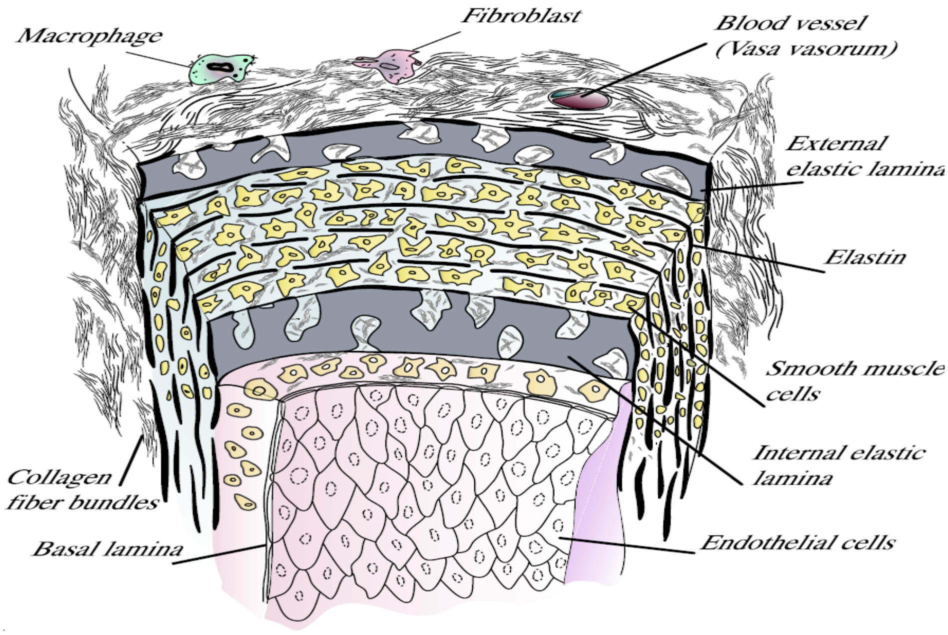

Figure 5.1. Schematic representation of an elastic artery. Adapted from Rhodin [9].

As illustrated in Figure 5.1, all blood vessels share some common characteristics, for example, they consist of three distinct layers or *tunicae*: The *tunica intima, tunica media* and *tunica adventitia*. In young human arteries the intima is a thin endothelial layer that lines the inside walls, and sits on a very thin (~80 nm) basal lamina of a net-like type IV collagen. In general, the endothelial cells tend to be elongated in the direction of the blood flow. They act as a semipermeable membrane, through which nutrients and chemical signals can reach the cells in the vessel wall from the bloodstream. The intima has also a key role in regulating the active response of the vessel: as a membrane, it is the conduit through which pressure regulating agents reach the media. Additionally, it is known that the intima produces NO (nitric oxide), which relaxes smooth muscle cells in the media and thus helps control the *vascular tone*. Despite its great functional importance, due to its small thickness in young arteries the intima is usually neglected when considering the different layer contributions to the global mechanical resistance of the vessel wall. The intima is separated from the media by the *internal elastica lamina*, a fenestrated sheet of elastin. The media is formed primarily by smooth muscle cells (SMC) that are embedded in an extracellular plexus of elastin and collagen (mainly types I and III) and an aqueous ground substance that also contains proteoglycans. Depending on the internal arrangement of the smooth muscle cells in the media, it is distinguished between *elastic arteries* and *muscular arteries*. The former tend to be large-diameter vessels close to the heart, and include the aorta, the main pulmonary artery, the common carotid and common iliac arteries. Their most characteristic histological feature is the so-called *lamellar unit*, a sandwich-like ‘sublayer’ of smooth muscle cells and thin elastic laminae. Histological sections of elastic arteries show concentric ring-like structures (Fig. 5.1), as many as 40 to 70 in thick vessels like in the human aorta, that are tied together by radially oriented collagen. In muscular arteries, the media appears as a single thick ring of smooth muscle cells. The SMC are embedded in a loose connective tissue matrix and arranged as a sequence of concentric layers of cells, which can reach numbers of 25-40 in larger vessels like in the femoral artery. Sometimes it is difficult to identify clearly between elastic and muscular arteries, due to the fact that abrupt changes do not occur in continuous structures like the vasculature. These transitions occur smoothly and the corresponding artery segments loose their characteristical lamellar structure progressively, as happens in the internal and external carotid arteries. Finally, the adventitia is the outermost layer of the vessel wall. It consists of a dense network of type I collagen fibers with scattered fibroblasts, elastin and nerves.

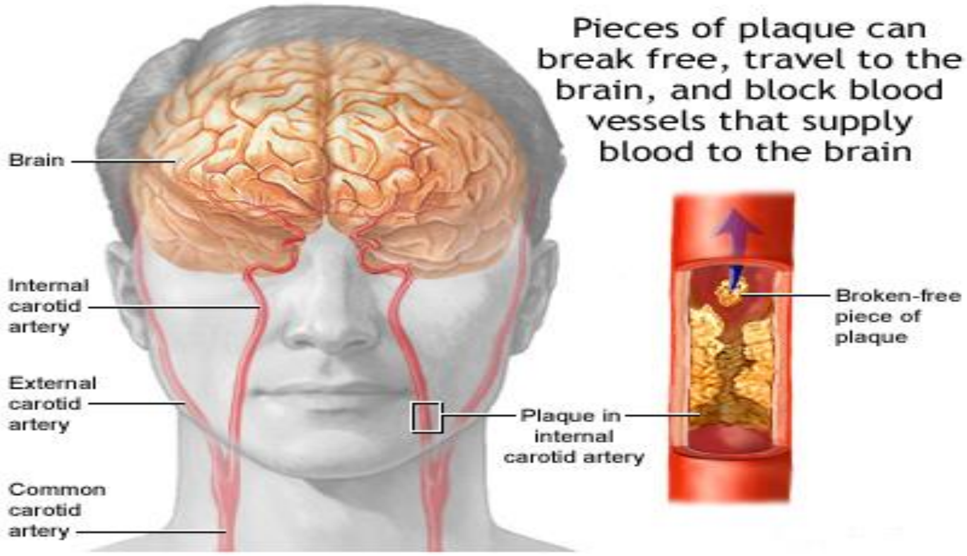

Figure 5.2. Many parts and sections of carotid arteries, in addition to plaque build-up progression inside the artery.

Figure 5.2, illustrates the build-up of plaque in the internal carotid artery may lead to narrowing and irregularity of the artery's lumen, preventing proper blood flow to the brain. More commonly, as the narrowing worsens, pieces of plaque in the internal carotid artery can break free, travel to the brain and block blood vessels that supply blood to the brain. This leads to stroke, with possible paralysis or other deficits.

Atherosclerosis is a local inflammatory disease of the arteries that primarily alters the conduit function by reducing the lumen, sometimes completely blocking blood flow. Atherosclerosis appears preferably at junctions and branches of conduit arteries (like coronary arteries and carotid bifurcation), always at sites of altered flow patterns. (Figure 5.3)

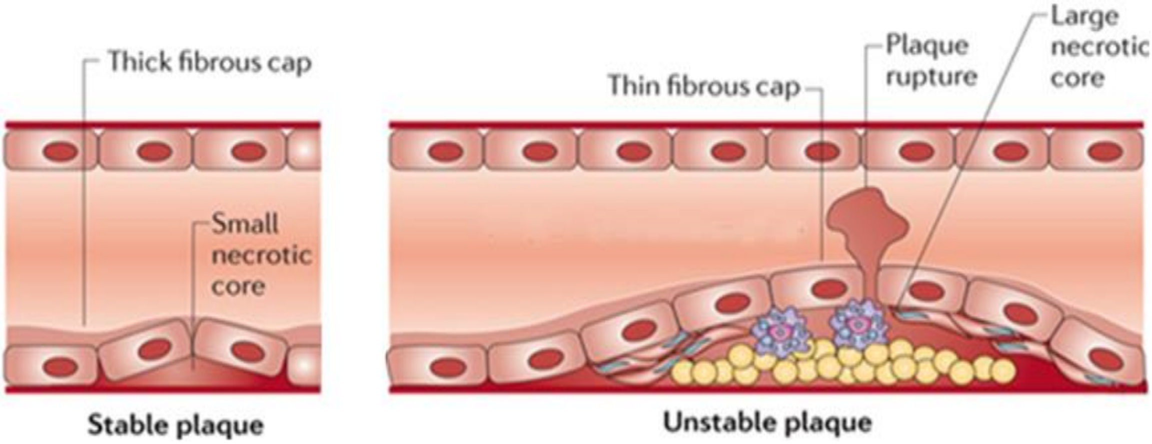

Figure 5.3. Progression of atherosclerotic disease. From the initial state, where LDL migrate through the endothelium in the intima (left side) to the beginning of intima thickening (right side). Illustration adapted from [44].

The natural history of atherosclerosis starts with the formation of fatty streaks by a specific trapping and retention of lipoproteins at lesion prone sites, due to an imbalance between the LDL (low density lipoprotein) concentration in the tissue with respect to the plasma. When this happens, the lipids are trapped in the extracellular matrix, in the basal zone of the intima. If this trapping is pathologic, there is an increase of leukocytes that adhere to the endothelial surface, supported by the expression of specific adhesion molecules. This is seen as the start of the inflammatory response. As a result, monocytes enter the artery wall and rapidly differentiate into tissue macrophages, subsequently transforming into foam cells by ingesting trapped and modified lipoproteins. Many of the foam cells within the lesion become activated to express a large number of additional factors that likely play important roles in the atherogenic process, from inducing anomalous behavior of healthy cells to providing a favorable biochemical environment for disease progression (Figure 5.3).

A more advanced lesion is hallmarked by the formation of a *fibrous cap* [44, 45]. In this process, smooth muscle cells migrate from the media to the intima and change phenotype, switching from being contractile to a cell type which proliferates and produces large amounts of connective tissues [46]. The fibrous cap acts as a protective shield for the underlying lipid pool, which has a necrotic core with interspersed microscopic calcium nodules. At this stage, there is a significant dysregulation of the vascular tone, likely due to a reduction in NO availability to the now atrophic media.

In the final stage, the atheromatous plaque described above may either become stable, in which case it only impairs blood flow, or unstable, where it is at risk of rupturing and developing its highly thrombogenic contents into the blood stream. It has been established that it is the plaque composition, rather than its size, that determines its instability [47, 48].

From this short description, it is obvious that the structure and the mechanics of the wall changes dramatically in the event of atherosclerosis.

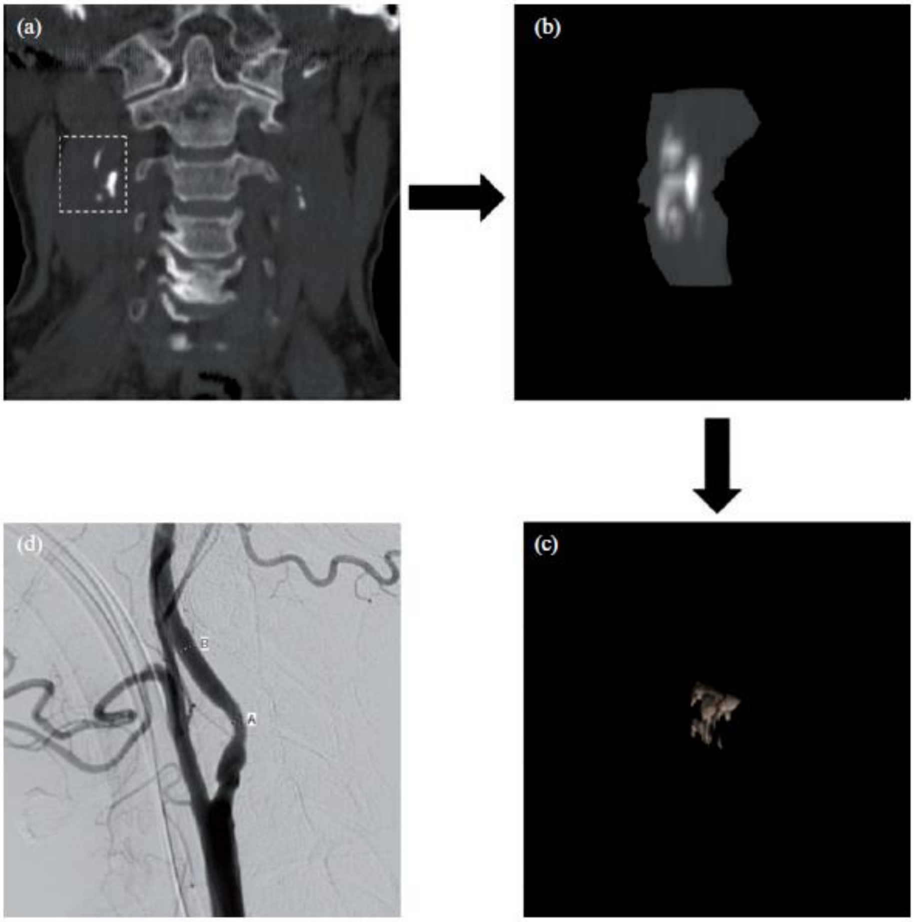

Figure 5.4. Calculation of plaque volume in a step-by-step fashion using the software and measurement of percent stenosis is demonstrated. (a) Manually drawn region of interest for sculpting is depicted on the coronal maximum intensity projection (MIP) image. (b) Calcified plaque on the sculpted MIP. (c) Volume rendered appearance of the plaque with automatic calculation of calcified plaque volume with a single button click, calculated to be 0.25cm^3 in this patient. (d) Calculation of percent stenosis on lateral view of carotid digital subtraction angiography.

In figure 5.4, we depicted calculation of plaque volume in a step-by-step fashion using the software and measurement of percent stenosis is demonstrated. (a) Manually drawn region of interest for sculpting is depicted on the coronal maximum intensity projection (MIP) image. (b) Calcified plaque on the sculpted MIP. (c) Volume rendered appearance of the plaque with automatic calculation of calcified plaque volume with a single button click, calculated to be 0.25cm^3 in this patient. (d) Calculation of percent stenosis on lateral view of carotid digital subtraction angiography. The luminal diameter was measured at the narrowest part (A), which was a post-bulbar location for this particular case; B corresponds to the luminal diameter in the distal cervical internal carotid artery with percent stenosis and was calculated using the following formula: Percent stenosis 5(B–A)/B, yielding a 55% stenosis for this patient.

The Agatston score is the EBCT-based scale used to quantify coronary calcification and has plentiful data to support its usefulness. It is based on the density measurements of the calcium. The Agatston score is reproducible to 15%–20%. The reason the Agatston score is accurate only to 15%–20% is that the density of the calcium is assigned a weighting factor (density score) in a stepwise manner that is not linear or continuous. As illustrated in Figure 5.5, an insignificantly different Hounsfield unit score could yield a significantly different density score. Because the Agatston score is a product of this density factor and the area of the calcium in the artery, a density score that is a factor higher will yield an Agatston score that is an order of magnitude different despite the fact that the Hounsfield unit scores for the calcium were very similar. For example, a Hounsfield unit score of 200 will result in a density factor of 1, whereas a score of 201 will yield a density score of 2. If the calcified area is 5 pixels, then the Hounsfield unit score of 200 will yield an Agatston score of 5 (product of a density score of 1 and a calcium area of 5 pixels). The Hounsfield unit score of 201 (not significantly different from a score of 200 as in the above example) will yield an Agatston score of 10 (product of a density score of 2 and a calcium area of 5 pixels) because the density factor was stepped up to 2 (Figure 5.5).
If we assume the area of the calcified plaque=4mm2 and Peak HU=270 the based on above equation Ca score for one slice = 8. Continuously, If slice thickness is 1 mm and number of slices over volume=220 the whole Ca Score of the plaque would be 220x8=1760.

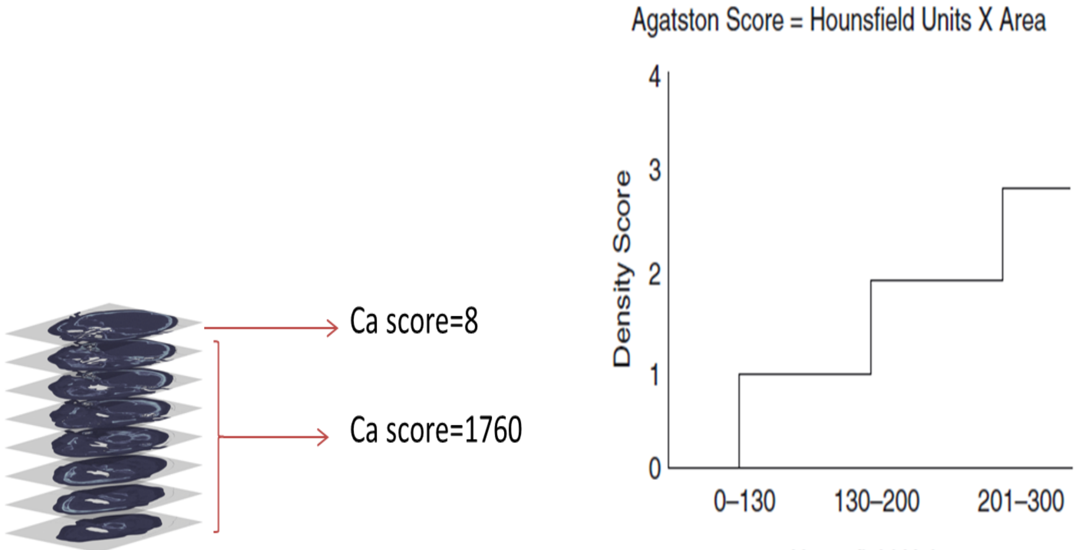

Figure 5.5. Stepwise relationship between Hounsfield units and the calcium density score as they relate to the determination of the Agatston score.

In the literature, [49] performed an elaborated study on preoperative simulation of CAS using Finite Element Method (FEM), by choosing single image based data to model the stent, vessel and the plaque. Two homogenous and non-homogenous material properties are defined based on constitutive law strain energy function and maximum stress obtained from each material properties are reported as 152 KPa and 91.3 KPa respectively. However plaque is considered as one body with no classification of different fibroatheroma layers and nonlinearity of atherosclerosis material characteristics are not fully perceivable. Chau *et al.* [42] investigated on post-expansion response of the slotted tube in the presence of plaque and artery. The configuration is not extracted from a patient-specific framework, thus it is a virtual design of the

CAS simulation. Material properties for plaque and artery are defined as linear isotropic. The maximum pressure load on plaque was specified as 2.65 MPa with max Von mises stress of plaque equal to 0.883 MPa. Wong *et al*. [43] performed an elaborated study on anisotropic and elastic mechanical impact of carotid calcified plaque in rupture using single model geometry by exploiting two dimensional structural analyses. Virtual simulation showed critical stress is lower for calcified plaques than that of non-calcified one emphasizing the stabilization of fibroatheroma plaque. Zhao *et al*. [44] conducted a single computational model of Finite Element Analysis (FEA) to simulate CAS procedure and compare the ultimate mechanical properties of soft and calcified plaque. Smaller stress distribution was reported in calcified plaque with respect to soft plaque due to energy absorption by calcification indicating the less arterial vulnerability. Another statistical study was performed by Yang *et al*. [45] that investigated on association of mechanical properties of carotid calcified plaque progression measured by wall thickness increase (WTI) on *in vivo* Magnetic Resonance Imaging (MRI) data. They found a negative linear correlation between WTI and plaque wall stress confirming that increase in plaque size leads to lower flow wall shear stress. They also performed linear regression analysis for predicting a patient-specific quantitative plaque growth functions.

5.2. Carotid Artery Stenting

In order to perform CAS, a small incision is made in the patient's groin, arm or wrist. A catheter is introduced into an artery in the body through this incision, and the physician advances it to the narrowed part of your carotid artery. Next, a special filter is delivered through the catheter and placed just beyond the narrowed section of the artery. This small filter is part of a system (embolic protection system) designed to catch and remove plaque and other particles that may be released during the procedure. After the embolic protection device is in place, the artery may need to be enlarged to make room for the stent. To do this, the physician places a small, deflated balloon through the catheter to the blocked area of the carotid artery. When the balloon is in the right place, it is inflated. This pushes the plaque buildup aside and reopens the artery to restore blood flow. The balloon is deflated and removed. Then a small metal mesh tube called a stent is placed in the artery and is expanded to prop the artery open and allow blood flow to the brain (Figure 5.6). After the stent is implanted, a balloon may be inflated inside the stent to better position the stent against the artery wall; then the balloon, filter and catheter are removed. The incision in the groin, arm or wrist is closed. The stent remains in place to help prevent future narrowing of the carotid artery.

Figure 5.6. Real size and shape of an angioplasty stent that is a small tube mesh.

The abovementioned procedure has been illustrated in the figure 5.7 (b) below by using a closed-cell stent. Panel (a) in Figure 5.7 depicts the angioplasty balloon expanded by the catheter inside the artery in order to press the atherosclerotic plaque.

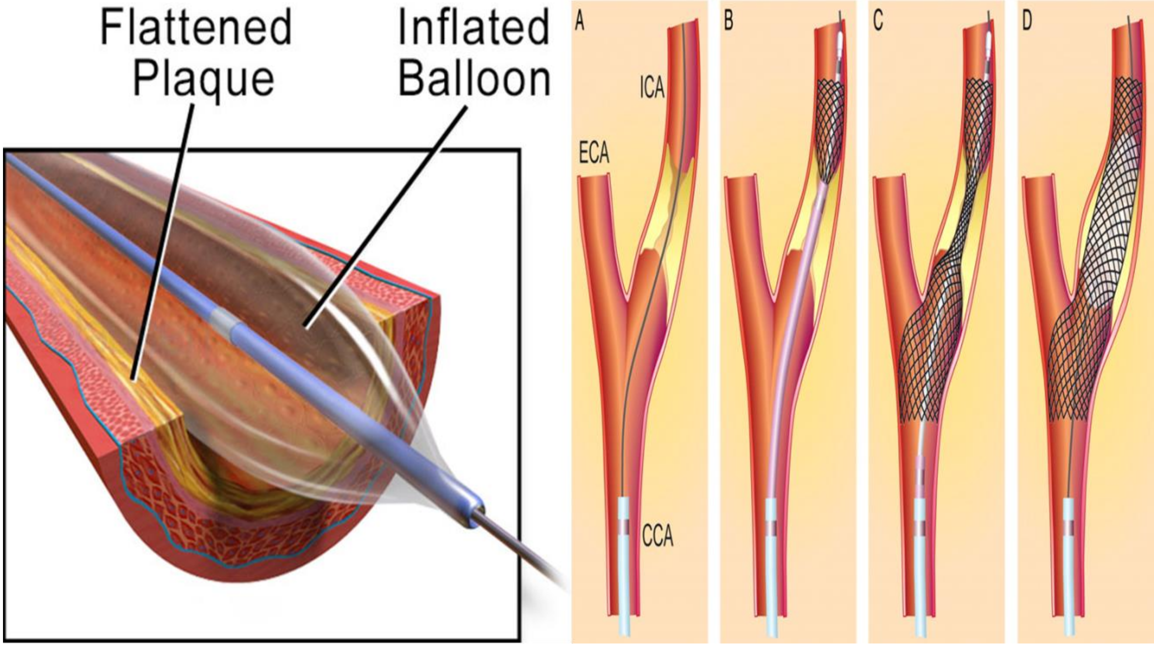

(a) (b)

Figure 5.7. (a)Angioplasty balloon inserted by the catheter is depicted inside the artery to push the plaque. (b) the whole procedure of carotid artery stenting is illustrated by a closed-cell stent.

5.3. Material and Mechanical parameters

First we have to prove how Ca score is related to hardness of the calcified plaque. We have to find a correlation between the Ca score, stiffness and hardness. Stiffness means elasticity and hardness means plasticity. Stiffness measures how linearly the stress that imposed on the plaque responds as strain and it elongates from the initial length. Stiffness is shown as young's modulus and it only depicts the elasticity of the plaque below the Yield strength. Hence the slope of the stress-strain curve represents young's modulus.

If one object goes beyond the yield strength without rupture then it has non-linear material model which is called plasticity. In the stress-strain curve after the yield point, the slope of the curve represents how plastic is the object and it is measured using Tangent modulus. The curve continues until reaches to Ultimate tensile strength which beyond that point the object ruptures or breaks (Figure 5.8).

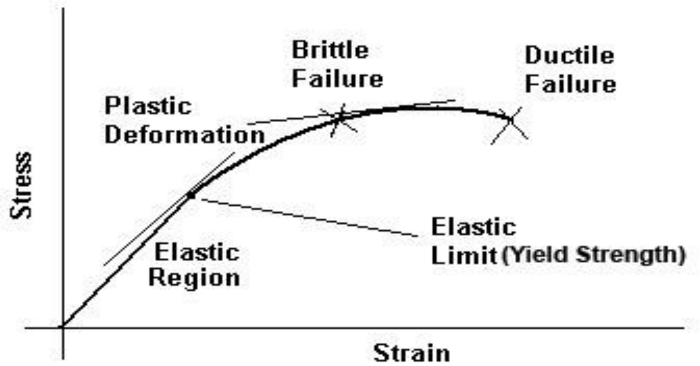

Figure 5.8. A general stress-strain curve that demonstrates elastic and plastic/linear and nonlinear domains of a parameter.

Since biomaterial objects such as tissues are non-linear materials, so we consider them having plasticity in behavior. Elasticity for the material is defined by young's modulus and Poisson ratio where plasticity is defined by yield strength and tangent modulus as mechanical parameters. We consider biomaterials as non-homogenous but isotropic in our analysis. Isotropic means the direction of the loads imposed on the plaques is not considered in our analysis and they all have isotropic and ubiquitous responds to the loads. Non-homogenous means we consider the calcified plaques composed as different composition, not one material, hence we define different density for each calcified plaque. Therefore in order to analyze hardness of the plaque, we must consider both its **Elasticity** and **Plasticity**. In Figure 5.9, the main concepts for Elastic modulus and evaluation of compressibility as Poisson's ratio have been depicted.

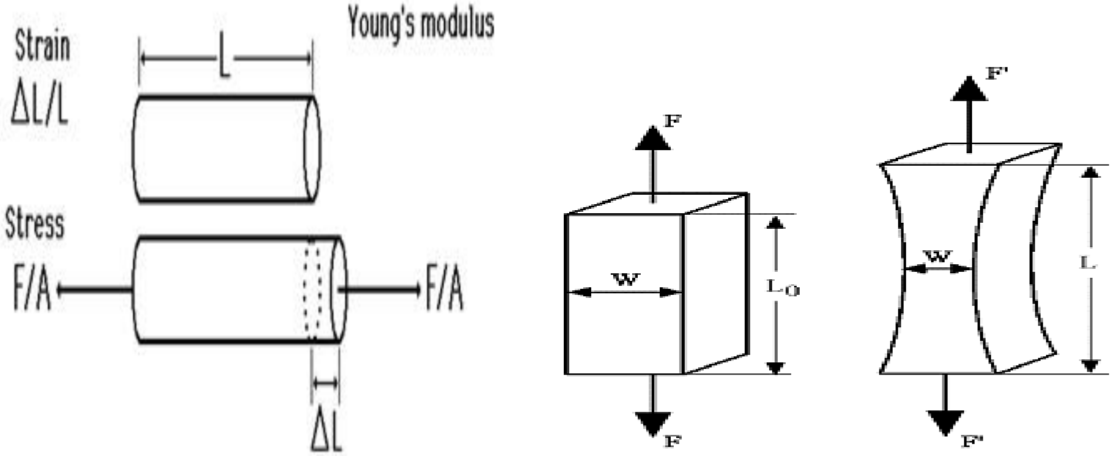

(a) (b)

Figure 5.9. (a) Depicts the main principle of Young’s modulus (Elastic modulus) and (b) Poisson’s ratio.

In the following equations the main equations in order to obtain the Young’s modulus of elasticity (Elastic Modulus) and Poisson’s ratio of compressity have been shown.

$$Young's\ Modulus = Elastic\ Modulus = E = \frac{stress}{strain} = \frac{F/A}{\Delta L/L} \qquad \text{(Equation 5.1)}$$

$$Poisson's\ ratio = \frac{(w-w_0)/w}{(L-L_0)/L} \qquad \text{(Equation 5.2)}$$

5.3.1. Volume score

Ca score is composed of three elements. HU, Area and Volume. Based on the fact that no significant correlation exists between percent area of calcification and the maximum stress thus stiffness [54], hence the element of volume and area do not influence hardness of the calcium. Also it has been suggested that it is the type of the calcification that leads to plaque rupture not the size [55]. Therefore, we conclude largeness of the plaque has no impression on the plaque rupture and its hardness.

5.3.2. Elasticity

It has been suggested that existence of the calcification leads to stiffness of the arterial wall, thus the aortic calcification is associated with aortic stiffness [54], [55]. It means high Ca Score must lead to higher stiffness, which means elasticity of the plaque changes with different Ca score. We have to assign different Young’s modulus to each plaque. Therefore, we can say there is a linear and positive proportion between Ca score and stiffness. Ca score is associated with stiffness.

Afterwards, we focus on the last element HU. We have to prove that higher HU means higher stiffness. There is not such equation relationship which states higher HU leads to higher stiffness specially in biomaterials because of their non-linearity in material behavior, but based on [57] we can statistically prove that higher HU leads to stiffer material in terms of young’s modulus. In [57] Cortical bone and Cancellous bone (Spongy bone) are analyzed in order to relate HU, Density and young’s modulus using linear and exponential regression empirically.

First, we used the method in [58] to obtain density of the calcified plaque base on its HU using the related and appropriate equations. Then we obtain the young’s modulus using the density that was obtained above via following equations to correlate the HU, density and young's modulus for each plaque [57]. I considered the cortical bone as the main tissue that form the bones, therefore it is dense and stiff which release chemical materials mainly **Calcium**. Spongy bone is less dense and soft and it combines with cortical bone to form the whole skeleton. The correlation range of HU and bone types is presented in the following chart [57].

- **a) Compact cortical bone → ≥1200 HU.**
- **b) Crestal cortical bone and coarse trabecular bone underneath → 700 ~ 1200 HU.**
- **c) Porous crestal layer of cortical bone and fine trabecular bone → 350 ~ 700 HU.**
- **d) Fine trabecular bone (mostly posterior maxilla) → 100 ~ 350 HU.**

$$HU \geq 1200 \ \rightarrow Considered\ as\ Cortical\ bone, E = 0.011 \times \rho - 9.212$$
$$100 \leq HU \leq 1200 \rightarrow Considered\ as\ Spongy\ bone, E = 0.005 \times \rho^{1.91}$$

ρ represents density and E young's modulus. HU is considered as peak HU, the same as Ca score. All the young's modulus for the calcified plaques are assigned based on above equations.

5.3.3. Plasticity

In definition, plasticity is defined as "resistance to deformation, rupture and penetration". Base on [55], the plaques that rupture have less ultimate tensile strength, means they rupture with less stress. On the contrary the plaques with higher ultimate strength, they resist in break, thus are harder (higher HU). In order to find relation between hardness and plasticity in this domain, we state that higher ultimate strength means most likely the plaque has higher yield strength and less elongation on break and yield, hence base on the following equation, Tangent modulus is increased and the slope of the stress-strain curve increases, that means the plaque behaves less plastic.

$$Tangent\ Modulus = \left(\begin{matrix} Ultimate\ Tensile\ Strength - \\ Yield\ Strenght \end{matrix}\right) \Big/ \left(\begin{matrix} Elongation\ at\ Ultimate\ strength - \\ Elongation\ at\ Yield \end{matrix}\right)$$ (Equation 5.3)

$$Elongation\ at\ Ultimate\ strength = {changed\ lenght\ at\ break}/{initial\ lenght}$$

(Equation 5.4)

$$Elongation\ at\ Yield = {yield\ strength}/{young's\ modulus}$$ (Equation 5.5)

On the contrary, if we follow the same logic, we can state that the softer plaque (lower HU and lower ultimate strength), leads to more plastic behavior of the calcified plaque (less steep slope). Higher Ca score means Higher HU and thus stiffer calcification that leads to higher young's modulus. In some states, it is harder in terms of elasticity. Higher Ca score means higher HU and with respect to above conclusion, it is harder with higher ultimate tensile strength thus less plastic. Finally, in the following Figure 5.10, stress-strain curves belonging to four patients are depicted. Top left graph belongs to patient 1 with the highest Ca score and HU, therefore it is harder and stiffer but less plastic as can be seen by the slope of the curves in both elastic and plastic domains. On the contrary, the bottom-left patient 4 has the least Ca score thus HU, and the slope of elasticity and plasticity is less, meaning it is less stiff and more plastic in behavior.

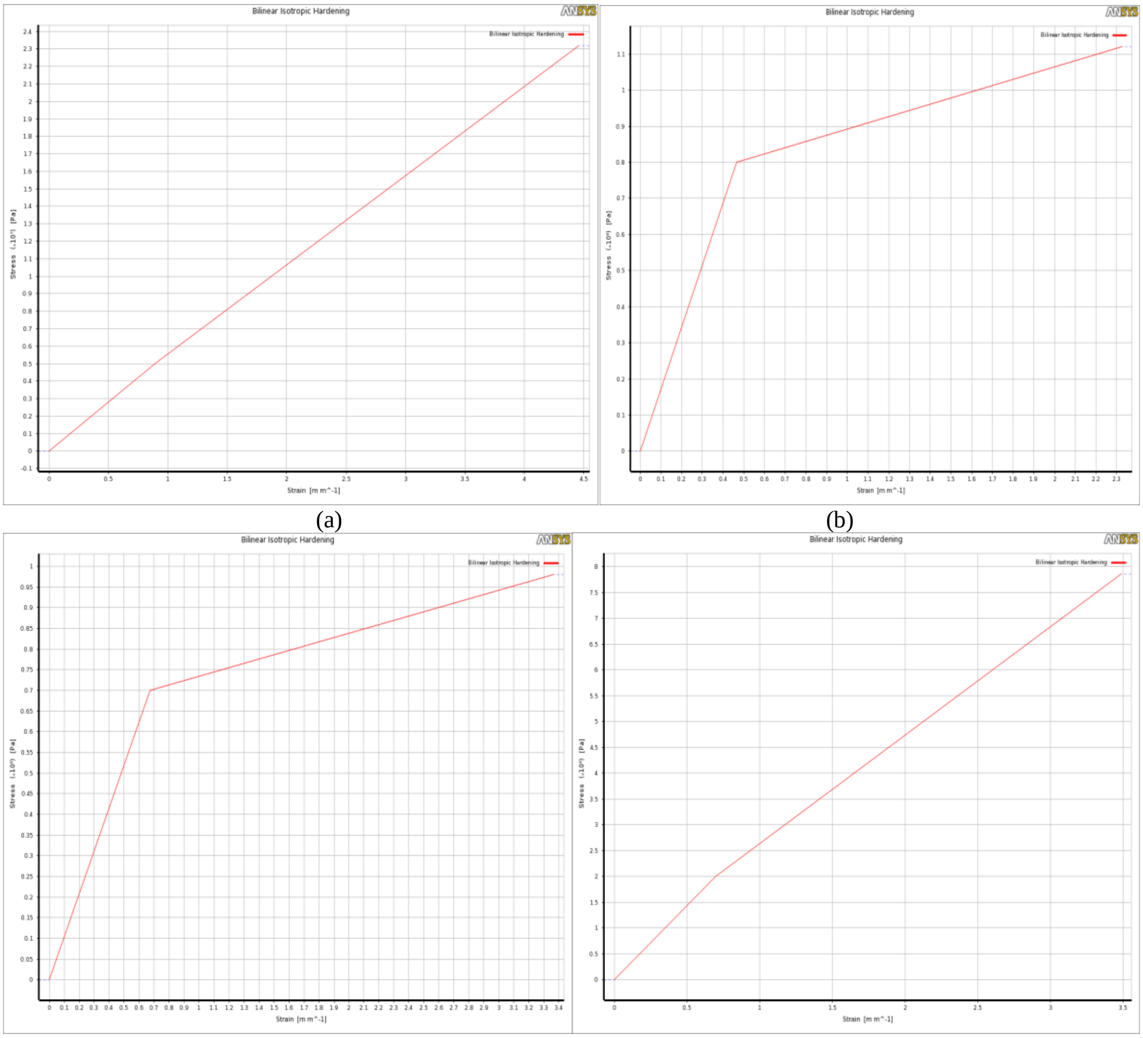

(a) (b)

(c) (d)

Figure 5.10. Stress-Strain curve belong to (a): Patient 1, (b): Patient 2, (c): Patient 3, (d): Patient 4.

5.4. Finite Element Method

The Finite Element Method (FEM), sometimes referred to as Finite Element Analysis (FEA), is a computational technique used to obtain approximate solutions of boundary value problems in engineering. Simply stated, a boundary value problem is a mathematical problem in which one or more dependent variables must satisfy a differential equation everywhere within a known domain of independent variables and satisfy specific conditions on the boundary of the domain. Boundary value problems are also sometimes called *field* problems. The field is the domain of interest and most often represents a physical structure. The *field variables* are the dependent variables of interest governed by the differential equation. The *boundary conditions* are the specified values of the field variables (or related variables such as derivatives) on the boundaries of the field. Depending on the type of physical problem being analyzed, the field variables may include physical displacement, temperature, heat flux, and fluid velocity to name only a few.

FEA generally and broadly consists of three major scopes. Geometry properties, Material definition and Simulation. The whole procedure starts with segmentation of the artery and the desired calcification, the empty area of the geometries are built in which the volume must be constructed out of the objects. After constructing the volume we have bodies and in this phase depending on the objective, many peripheral geometrical proofing must be performed such as smoothing, merging, etc. The next step is to assemble all the objects and bodies using Computer Aided Design (CAD) software, so that we can build our required construction in which in this research includes assembly of arteries and the balloon and stents. In this phase many cares have to be taken, since geometrical properties that have already been defined in the previous case plays a big role in the assembly and those specifications must be justified. The final step in the main phase of FEM which the simulation is performed. In order to perform the simulation the most important aspect is the definition of boundary condition.

First coordinates are defined based on the movement of the bodies in the simulation. Each boundary condition that is defined must be specified if it is symmetry or anti-symmetry. Then “Supports” are defined, in which depending on the confined movement of the bodies or faces, cylindrical, fixed, elastic etc supports can be defined. After this section, Mesh is defined for every object. Size, number of elements and nodes of the meshes depends on type of meshes that we define. Obviously the fine the mesh is, more accurate the simulation could be performed. Next part in which indicates the nonlinearity of the analysis, is the Contact definition. Likewise, depending on type of the contact that we have in the reality we would be able to define the desired contact properties between the bodies. Usually, the cross-sectional areas that we have contacts between the bodies has to be defined the same mesh type in order to facilitate the final FEM analysis. The insignificant parts of the bodies could be left with coarser meshes. The final section of FEM is the definition of loading condition. Types, amounts and direction of pressures/forces are indicated here in order to initialize the analysis.

However in this work, we performed nonlinear static structural analysis in which we ignore inertia and initial acceleration, but we define static forces base on clinical guides. Our material properties are nonlinear since we also analyzed plasticity, also our geometry is nonlinear because of having large deformations. We justified final criterion for nonlinearity that is contact, hence we follow all the criteria for a nonlinear analysis.

In figure 5.11, the three major phases of FEM for carotid artery stenting is illustrated and in the Figure 5.12 below, the general scheme of post-processing analysis of the artery stenting has been depicted.

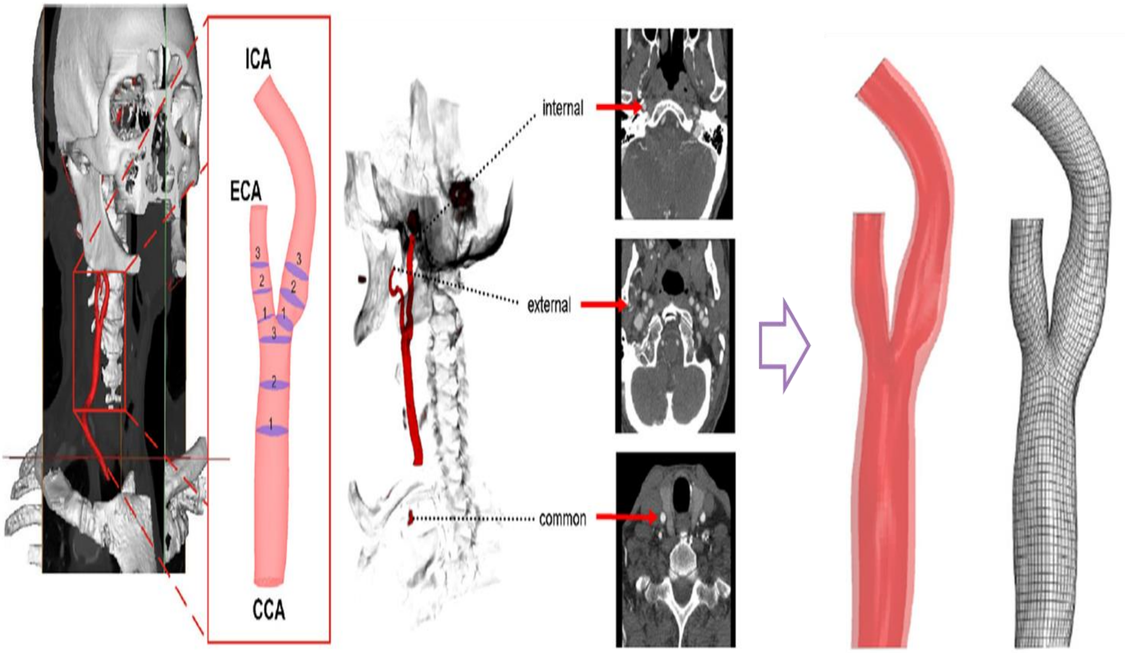

Figure 5.11. The broad procedure of FEM starting from segmentation part, in which the artery is segmented from a CT image. Afterwards, the geometry is structured and volumes are shaped in which the bodies are ready for the assembly part.

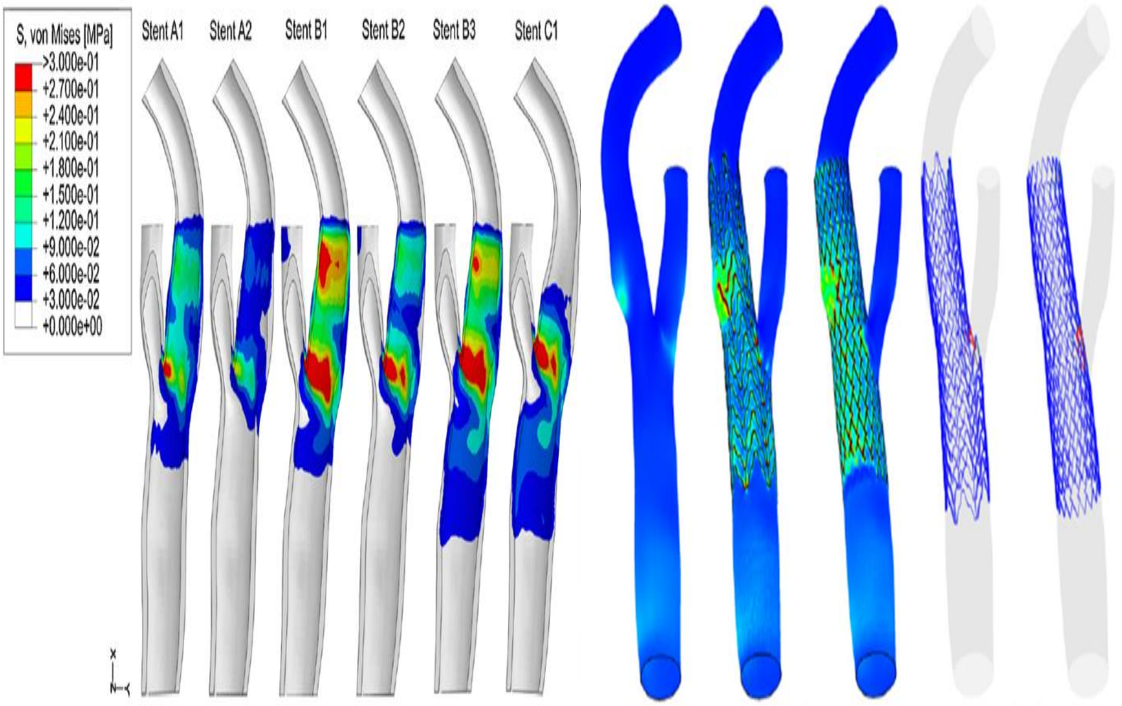

Figure 5.12. A general scheme of a post processing analysis of a FEM simulation as an example. In this sample analysis von mises pressure of the stent expansion is depicted inside the carotid artery.

5.5. Problems and aims of the work

Two major problems exist in CAS angioplasty: (i)elastic and small plaques with early calcifications penetrate into the stent leading to “plaque protrusion”(Figure 5.13-(a)). (ii)stiff and large caps which contain advanced calcifications when being pushed by the stent/balloon lead to eventual arterial wall rupture or stent fracture during the operation (Figure 5.13-(b)). Investigation on clinical as well as mechanical behavior of fibrous cap, lipid pools and different arterial layers have been extensively performed [54], [55], however there is lack of probe into association of calcification and physiological phenomena that occurs during the development of atherosclerosis as well as susceptibility of the carotid plaque during CAS angioplasty. The aim of this work is to particularly explore on contribution of calcification in atherosclerotic plaque rupture and to find its maximum resistance when imposed by external pressure load during interventional CAS placement by exploiting Agatston Calcium score.

In this work, we performed a virtual simulation exploiting FEM to design a patient-specific pre-operative framework in order to predict the interaction of main objects i.e. balloon, stent, calcified plaque and artery in CAS operation. In order to achieve this goal, we followed two approaches; (i)we obtained mechanical parameters imposed by balloon and stent on calcifications during CAS placement through a nonlinear static structural analysis to elaborate about plaque penetration and rupture characteristics. (ii)to find the nonlinear correlation between material properties of the calcification i.e. Ca score, elasticity, and its obtained mechanical properties i.e. equivalent stress, strains and ultimate external load in an imposed configuration. Teng *et al*. [38] statistically investigated on carotid atherosclerotic plaque progression measured by wall thickness increase (WTI) on *in vivo* Magnetic Resonance Imaging (MRI) data and found a negative correlation between WTI and plaque wall stress confirming the fact that increase in plaque size leads to lower flow wall shear stress. They also performed regression analysis to define a model for predicting a patient-specific quantitative plaque growth functions. However both correlation and regression analyses are linearly performed.

In the current study, we innovatively analyzed plastic behaviors of calcification and arterial wall in additional to linear elastic properties. However, in reality large calcifications with high Ca score could act as a ductile elastic material and conversely, calcifications with both small volume and Ca score might behave as hard brittle material, hence it is not trivial to non-experimentally classify the calcifications base on its hardness through the material properties. Therefore, we defined inter-patient densities for each calcification as a novelty, considering them as inhomogeneous material hence categorizing them by their elastic modulus.

(a)

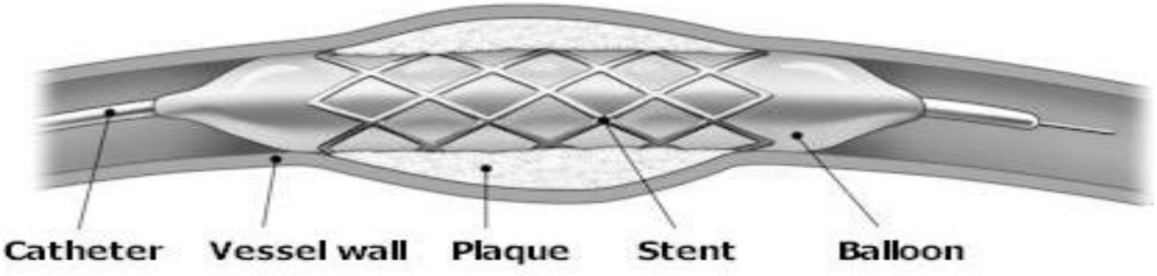

(b)

Figure 5.13. (a) When the stent is too much open, the plaque is smashed and penetrated into the stent leading to plaque protrusion. (b) When the stent is expanding, hardness of the plaque prevents the stent to open completely leads to plaque and arterial vulnerability.

This section of the work is organized as follows:

In Chapter 5 we introduced and explained general concepts of atherosclerosis and calcified carotid plaques and the mode of its evaluation using Agatston score. Then whole general procedure of carotid artery stenting is explained in detail. In order to become acquaintance with the investigated parameters and the way to probe the plaque rupture we introduced material and mechanical parameters exploited to analysis the plaque rupture. Finally we stated some general procedure of Finite Element Analysis in order to deploy the method in simulation and obtaining *in silico* results.

In chapter 6 the material and method of the work is explained in detail. The method to data acquisition is stated first and the model to design and reconstruction both calcification and balloon/stents are explained in elaboration. The final part of this chapter is dedicated to exploiting FEM in our method.

In chapter 7, the results that are obtained through both imposing balloon and stent on the calcification belonging to each patient are presented. In addition to mechanical and material parameters that are obtained we performed nonlinear statistical analysis to find the correlation between the parameters.

Eventually in chapter 8, the final chapter we presented discussion and conclusion about our work along with the future work.

Chapter 6 : Materials and Methods

6.1. Data Acquisitions

A total of 148 carotid bifurcations belonging to 74 patients (mean age 72.7 ± 6.6 years, male:female=69:5) were acquired. MDCT angiography was performed in all study patients using helical acquisition with a 64-detector row CT scanner (SOMATOM Definition; Siemens Medical Solutions, Forchheim, Germany) with two X-ray tubes mounted onto a single gantry at an angle of 90° as described previously [46]. The imaging acquisition parameters were as follows: spiral mode 0.33-second gantry rotation; collimation, 32 x 0.6 mm; pitch factor, 1.5; section thickness 1.0 mm; reconstruction interval, 0.5 mm, and acquisition parameters 120 kVp and 350 mA. A total 50 ml of non-ionized contrast medium, iohexol (Omnipaque 300; Daiichi Sankyo, Tokyo, Japan) or iopamidol (Iopamiron 300; Bayer Schering Pharma, Berlin, Germany), was injected at a flow rate of 3.5 ml/s, followed by 25 ml of a saline chaser at the same rate as the contrast medium. Optimal timing of MDCT angiography acquisition was determined by an automated bolus-timing program. Images were obtained from the aortic arch to the level of the inferior orbits. The image data were transferred to a computer workstation (Ziostation version 1.17; Amin, Tokyo, Japan) for image post-processing and calcification of the carotid plaque was quantified. The Agatston calcium score [47] of any calcification area >1 mm2 with attenuation ≥130 Hounsfield units (HU) was determined by multiplying lesion area (total number of pixels) by the cofactor 1–4 (cofactor 1; 130–199 HU, cofactor 2; 200–299 HU, cofactor 3; 300–399 HU, cofactor 4; ≥400 HU) with non–contrast-enhanced CT obtain before contrast media injection for CT angiography. Calcium was further quantified in cubic millimeters with the volume score calculated as the product of voxel volume and number of voxels in the region of interest and the overall calcium score of the plaque was the sum of the values for all individual lesions [48]. All the carotid bifurcations have gone under surgical interventions by CAS, including 4 restenosis cases. The ethics guidelines for clinical studies by the Japanese Health Labor and Welfare Ministry (2003) were strictly observed.

6.2. Calcification model reconstruction

Among all the bifurcations, 20 cases were chosen for three dimensional experimental simulations with average Ca score and calcified area of 400±510 and 84.2±77.1 mm^2 respectively. Average peak HU is 835±351. Table 1 represents material properties of calcifications ordered from the highest Ca score to the lowest. Cases with a fair dispersion of Ca score along with similar geometry and volume score are chosen in order to prevent dependency of the final results on extensiveness of local geometry. The reason in which distribution of volume score and area of the calcifications does not coincide is that volume score is calculated based on all the lesions inside the carotid artery, however area belongs to one or two calcifications chosen among all the lesions depending on the case, hence area is single calcification specific.

We defined different densities for each calcification, since calcified plaques are inhomogeneous and material substantial are irregularly distributed over the plaque, thus some parts are denser than the other parts. With respect to our previous work [46] 81.3% of calcified plaque with Volume Score >500 mm^3, have larger differences between peak and mean HU, indicating that larger calcifications tend to be more inhomogeneous. Therefore by defining different densities, we experience a virtual configuration which is close to reality. We considered calcified plaques as inhomogeneous but isotropic material for two reasons: (i)we assume tensile and compressive tensions imposed on the materials are equal on all the directions. (ii)complexity in analyzing anisotropic mechanical behavior for inhomogeneous materials.

In order to define material properties for calcifications, an equation is required to numerically express the available energy in fracture of vulnerable plaques. Consequently, a stress-strain curve is modeled according to Ramberg-Osgood equation (Equation 6.1) in which divides the material behavior into elastic-plastic parts and explains the strain in both domains.

$$\varepsilon = \varepsilon_e + \varepsilon_p \quad \text{(Equation 6.1)}$$

ε_e and ε_p represent elastic and plastic strain respectively. For low stress values, the nonlinear component is not significant when compared to the linear component. In the following sections, we described the numerical methodology in order to express both linear and nonlinear material behavior in this study.

6.2.1. Linear elasticity

It has been suggested that existence of the calcification leads to stiffness of the arterial wall, thus the aortic calcification is associated with aortic stiffness [50], [51]. Consequently, implies association of Ca score and stiffness i.e. EM. Since calcium accumulation in arteries by mineralization and calcium loss from bone often coexists, and vascular calcification may share common mechanisms with bone remodeling [52], [53] hence in order to obtain different EM for different calcification, we shared the stiffness characteristics of the bones. In [54] Cortical and Spongy bones are analyzed in order to relate HU, density and EM using linear and exponential regression empirically. Cortical bone as the main tissue that forms the bones, it is dense and stiff which release chemical materials mainly calcium. However spongy bone is soft and it is combined with cortical bone to form the whole skeleton. Therefore, we first utilized the method in [55] to obtain density of the calcified plaque with respect to its peak HU. Then we computed EM by employing the obtained density using equations 6.2 and 6.3. In this way we correlate the HU, density and EM for each plaque. The correlation range of HU and bone types is presented in [56].

Patient No.	Ca Score	Volume score (mm^3)	Area(mm^2)	Poisson ratio	Elastic Modulus (MPa)	Density (Kg/m^3)
C1	2309	1882	304	0.4	4.461	1243
C2	867	700	116	0.4	5.61	1348
C3	850	709	242	0.4	2.22	907
C4	665	528	40	0.4	5.84	1369
C5	512	412	150	0.4	2.87	1036
C6	336	289	69	0.3	3.2	1104
C7	313	292	45	0.3	1.66	778
C8	292	247	104	0.3	2.18	898
C9	262	232	38	0.3	1.93	843
C10	221	190	118	0.3	2.31	925
C11	215	187	134	0.3	1.76	802
C12	212	200	33	0.3	1.09	624
C13	209	181	56	0.3	0.91	567
C14	198	203	73	0.25	1.72	793
C15	166	151	56	0.25	2.87	1037
C16	142	179	31	0.25	1.04	610
C17	102	138	22	0.25	0.4	363
C18	54	67	15	0.25	0.389	364
C19	45	42	5	0.25	0.733	507

C20	31	40	33	0.25	0.381	360
AVG	*400*	*343*	*84.2*	-	*2.17*	*823*
SD	*510*	*408*	*77.1*	-	*1.6*	*310*

Table 6.1. Material properties belong to all the calcifications in this study ordered from the highest to the lowest Ca score. patient-specific elastic modulus and density are also presented.

$HU \geq 1200 \rightarrow$ Considered as Cortical bone,

$$E = 0.011 \times \rho - 9.212 \qquad \text{(Equation 6.2)}$$

$100 \leq HU \leq 1200 \rightarrow$ Considered as Spongy bone,

$$E = 0.005 \times \rho\hat{}1.91 \qquad \text{(Equation 6.3)}$$

ρ represents density and E is elastic modulus. HU is considered as peak HU. All the EM for the calcified plaques are assigned based on the latter equations. Average of calculated EM and density are 2.17±1.6 MPa and 823±310 Kg/m^3 respectively. In Table 6.1, EM and density calculated for each patient is summarized. In chapter 8 correlation of Ca score and EM has been debated.

6.2.2. Nonlinear plasticity

The goal to investigate nonlinear behavior of a material is to obtain ultimate tensile strength (UTS) and strain at break. Utilizing FEM the idea is to apply the external loads on inner surface of both stent and balloon to expand and press the calcification while the internal stress of calcification cross the yield point. At this point plastic deformation starts and eventually calcification reaches to UTS and breaks. We performed sensitivity analysis on the external pressure load to find maximum allowed external pressure on each calcification and obtain the ultimate mechanical parameters at rupture. However in order to apply abovementioned simulation we required tangent modulus (TM) which we defined as slope of nonlinear domain after the yield point (σ_y) and then depending on applied forces on cross-sectional region of interest, desired ultimate parameters are achieved. Figure 6.1 expresses stress-strain curve obtained after stent simulation for calcification case 1.

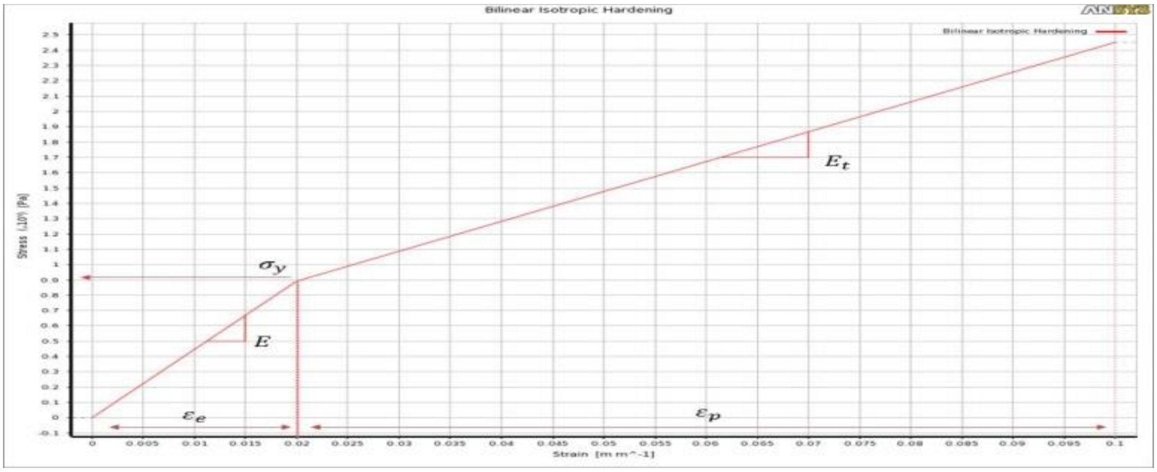

Figure 6.1. Stress-strain curve belong to calcification of case 1. σ_y is yield stress that plastic deformation begins. EM (E) and TM (E_t) have been pointed along with ε_e and ε_p that represent elastic and plastic strain.

Figure 6.1 depicts a sudden change from elastic domain to plastic deformation indicating the simulation using bi-linear strain hardening material model for both elastic-plastic domains. Following equations adequately define stress-strain relationship for this type of model that meet Equation 6.1 (Ramberg-Osgood) and eventually we can obtain TM, thus required mechanical parameters. [56]

$$\varepsilon_e = \frac{\sigma_y}{E} \quad \text{for } \sigma \leq \sigma_{y,} \quad \text{(Equation 6.4)}$$

$$\varepsilon_p = \frac{(\sigma - \sigma_y)}{E_t} \quad \text{for } \sigma > \sigma_y, \quad \text{(Equation 6.5)}$$

In above equations, E is EM and E_t is TM, σ and σ_y represent corresponding stress and yield stress respectively. However it has to be mentioned that if one is interested to define multi-linear constitutive low in order to numerically obtain the power-law relationship between stress and the amount of plastic strain for each calcification then following Ramberg-Osgood equation could be applied.

$$\varepsilon = \frac{\sigma_y}{E} + \left(\frac{\sigma - \sigma_y}{H}\right)^{\frac{1}{n}} \quad \text{for } \sigma > \sigma_y, \quad \text{(Equation 6.6)}$$

The first and second parts represent elastic and plastic domains respectively. On the logarithmic scales, this exponential function is mapped onto a straight line ($\log \sigma = \log H + n \log \varepsilon$), whose slope is equal to the strain hardening exponent (n), and whose intercept with a true strain value of 1 is the strength coefficient (H). Therefore H and n are dependent upon material property describing the hardening behavior and ε is corresponding true strain.[57]

6.2.3. 3D Reconstruction

Three dimensional reconstruction of the calcification and artery in fact follows the finite element section introduced in Chapter 5 section 4. The procedure starts with 3D segmentation of the artery and calcification from the DICOM CT image of the patients. The segmentation has been performed through the software Mimics (Materialise, 10.01, USA) by defining the specific intensity thresholding indicated as Masks. In this method, predefined intensity thresholding of Hounsfield Unit (HU) are deployed for each object of calcification and the artery to be segmented. The intensity thresholding we used for the artery is between 150 – 500 HU and 500 – 2000 HU for the calcification. By setting these values we can smoothly select only those objects by eliminating the background and all the other non-necessary objects inside the image such as head and neck. In this phase 3D geometries are constructed with volume and we store the files as binary STL files in order to be able to import in the next phases. (Figure 6.2)

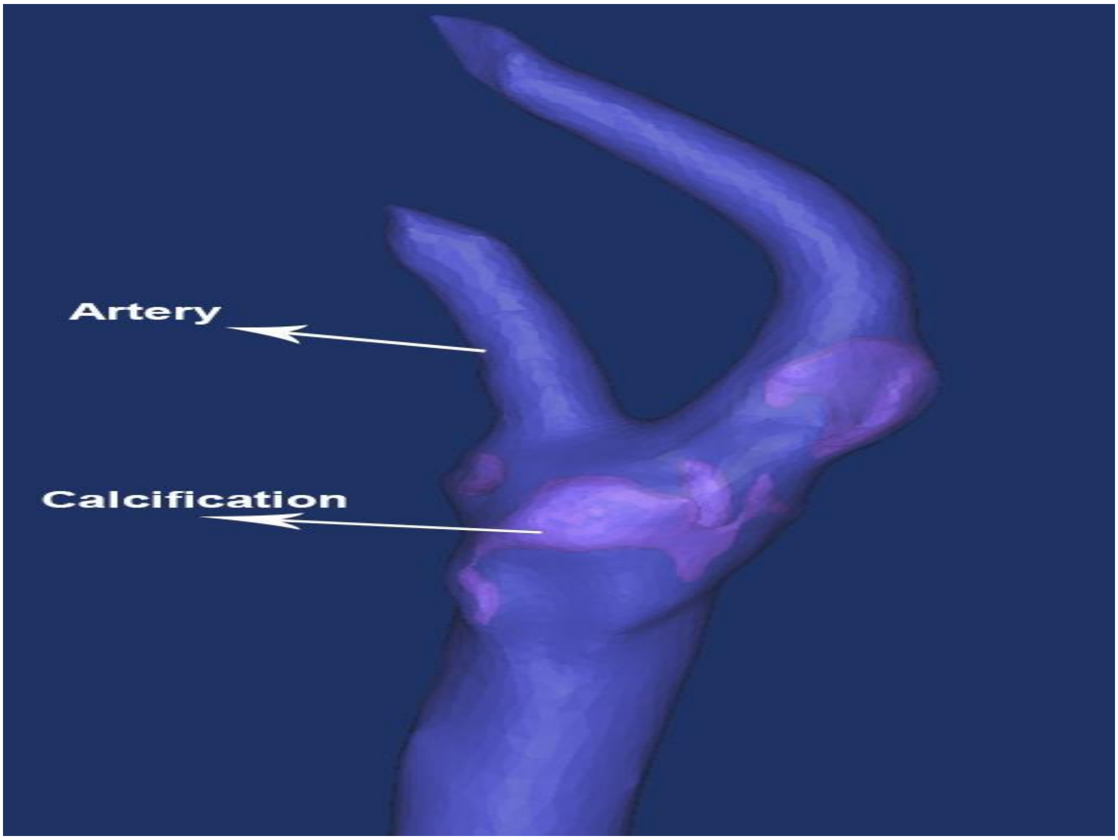

Figure 6.2. Segmentation and 3D reconstruction of the artery and the calcification without volume.

After building STL files from each object separately, we import the files in Rhinoceros (Robert McNeel & Associates, 5.8, USA) (Figure 6.3). In this phase we perform two major and crucial action. First we smooth the STL meshes by reducing the number of elements in the meshes. In this way we can simplify the meshes imported from Mimics. Then we must connect the nodes of the meshes from two objects of calcification and the artery, since as we import each file separetly the objects are sperated from eachother and this would make a problem in the next phase of analysis. As shown in Figure 6.3, we extract the mesh faces and then by using the PatchSingleFace command, we connect the edges belonging to two meshes. In this way we can specifically connect the meshes from two different objects. After that we must build the volume which is the most important section of this phase. We first merge the meshes and are connected together and then we use MeshToNurbs command to create the closed polysurface and construct the NURBS. In this way we can create the volume out of all the objects we just segmented from the CT images of the patients. Finally we save the files as .igs file for the next assembly part.

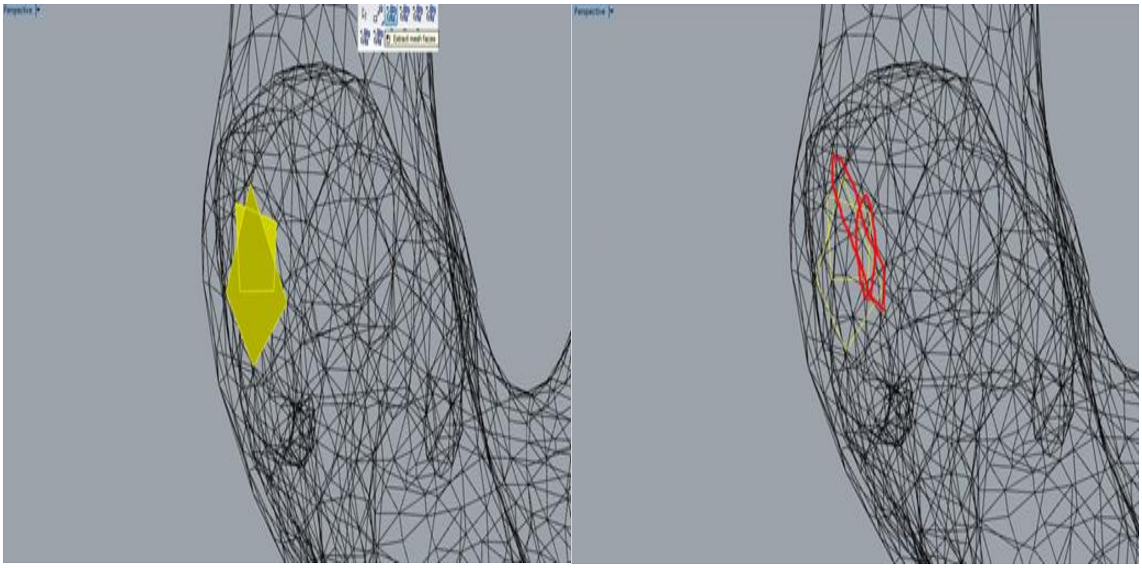

Figure 6.3. Connecting the meshes belonging to calcification and the artery in Rhinoceros.

The next phase is the assembly part. We must assemble and merge the previously designed stents and the balloon inside the arterial calcification. We perform this action using Solidworks (Dassault Systèmes SolidWorks Corp., 2013, Vélizy, France). The .igs file is imported and assembly is performed. The exact geometry and the distances are explained in the parts 6-3-1 and 6-4 in details. Figure 6.4 depicts the assembly of two stents models fixed on the calcification inside the artery.

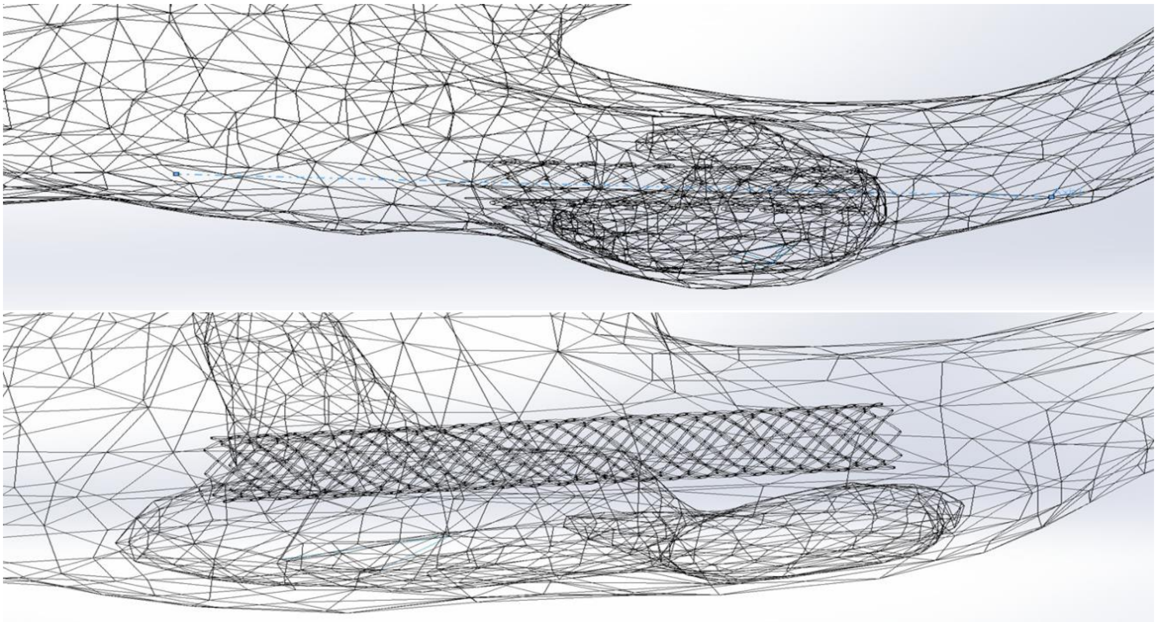

Figure 6.4. Assembly of two stent models resided on the calcification inside the artery using a specific geometry.

The final phase of 3D reconstruction belong to importing the designed assembly into geometry section of the Ansys (Ansys, Inc. 15.0, USA) in which it is employed for the main FEM analysis and obtaining the final mechanical parameters. Figure 6.5 below depicts the imported assembled stents, artery and calcification.

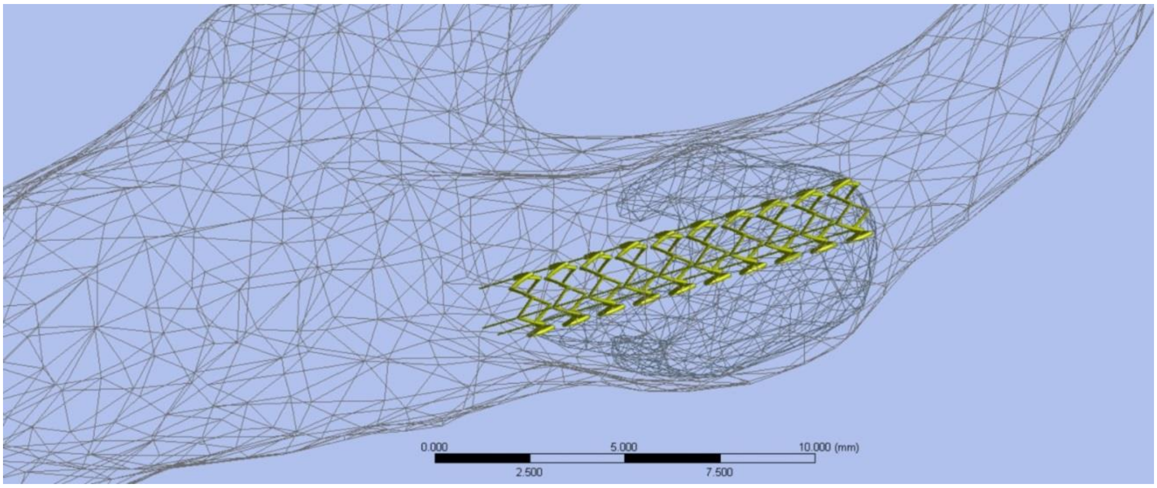

Figure 6.5. Assembled layout belongs to a case in which the stents is resided on the calcification inside the artery.

6.3. Balloon/Stent model reconstruction

We analyzed elastic-plastic material behavior of balloon/stents/artery and calcifications, thus Elastic Modulus (EM) and Poisson Ratio are defined to characterize linear elastic stiffness and compressibility for each calcified plaque. On the other hand to characterize the nonlinear plastic behavior, we defined slope of the curve after the yield point in the stress-strain curve as Tangent Modulus (TM). Two types of stents and one type of pre-stenting balloon are deployed in the simulations. Modeled stents are both carotid self-expandable open-cell and close-cell stent depending on the model of bifurcations. We chose the cases as such two types of stents are fairly included. Open cell stent belongs to Cordis Corporation registered as PRECISE® PRO RX®. The material is Nitinol alloy with geometry property of maximum expansion of 6~10 mm, 40 mm length and cell size of 2 mm and fits to extremely tortuous vessels. On the other hand, closed-cell stent is Carotid WALLSTENT® Monorail® from Boston Scientific. The material is stainless steel Elgiloy composed of DFT (Draw Filed Tubing) alloy monofilament wires braided in a tubular mesh configuration. The stent has 10 mm in diameter and 40 mm length which fits to unstable plaque morphology. Average arterial diameter for our experiments is 8~10 mm and the average calcification diameter is 0.5~7 mm and since the chosen stents should be 1~2 mm wider than the artery, the geometrical parameters are carefully chosen. Average calcification thickness is $95\mu m$. We deployed Sterling pre-stenting dilation balloon from Boston Scientific. It is made of compressible elastoplastic material with very low friction coefficient composed of Polyether block Amide (PDA) leading to atraumatic lesion entry with diameter of 3.5 mm and 40 mm length. In Table 6.2 all the material properties for the artery, angioplasty balloon and two utilized stents are presented.

Material property	Elastic Modulus (MPa)	Poisson ratio	Yield Strength (MPa)	Tangent Modulus (MPa)	Density (Kg/m^3)	Heat capacity (J/Kg.C)
Artery	1.75	0.49	1.1	0.9	1000	300
Sterling Balloon	513	0.27	56	85	1010	1700
Precise Stent	28000	0.3	100	800	6450	320
Wallstent Stent	189600	0.226	480	900	8300	430

Table 6.2. Utilized material properties for artery, balloon and two stents.

In the following Table 6.3 we present very useful and important information for each patient on type of stents, balloon number of voxels of calcification in the images, the side of carotid artery that has the crucial stenosis, size of the stents and the balloon and finally the amount of pressure and time on imposing the balloon by the real cardiologists.

No.	Side	Voxel	Stent	Size (mm)	Balloon Pre-dilatation	Size (mm)	atm	sec
1	L	2917	Precise	8x40	Sterling	3x40	6	30
2	L	1118	Precise	10x40	Sterling	3.5x40	6	30
3	R	1137	Wallstent	10x31	Sterling	3.5x40	6	30
4	L	831	Precise	8x40	Sterling	3x40	6	30
5	L	567	Wallstent	8x29	Sterling	3.5x40	6	30
6	R	474	Precise	8x40+8x30	Sterling	3x40	6	30
7	R	494	Wallstent	10x40	Sterling	3x40	6	30
8	R	388	Precise	8x40	Sterling	3.5x20	6	30
9	R	369	Wallstent	8x21	Sterling	3x30	6	30
10	R	291	Wallstent	10x24	Sterling	3x30	6	30
11	R	256	Precise	10x40	AMIIA	4x30	10	30
12	R	432	Wallstent	10x31	Sterling	3x40	6	30
13	R	388	Precise	7x40	Sterling	3x40	6	30
14	R	305	Wallstent	10x24	Sterling	3x30	6	30
15	R	245	Precise	7x40	Sterling	3x20	6	30
16	R	307	Precise	10x40	Sterling	3x40	6	30
17	L	251	Precise	10x40	Sterling	3x30	6	30
18	L	147	Wallstent	8x29	-	-	-	-
19	R	88	Wallstent	8x29	Sterling	3x40	6	30
20	L	71	Wallstent	10x31	Sterling	3.5x40	6	30

Table 6.3. Clinical information belonging to all the patients.

6.3.1. 3D reconstruction

3D reconstruction of the deployed balloon and two open-cell and closed-cell stents exactly follows the geometrical section of FEM already explained in Section 6-2 belonging to design of calcification and the artery. Except that we did not segment or extract the stents and balloon from the CT images. We designed using CAD software of Solidworks with respect to the geometry parameters presented in the previous section. Therefore, here we only present the final constructed images of the balloon and the stents in the following Figure 6.6.

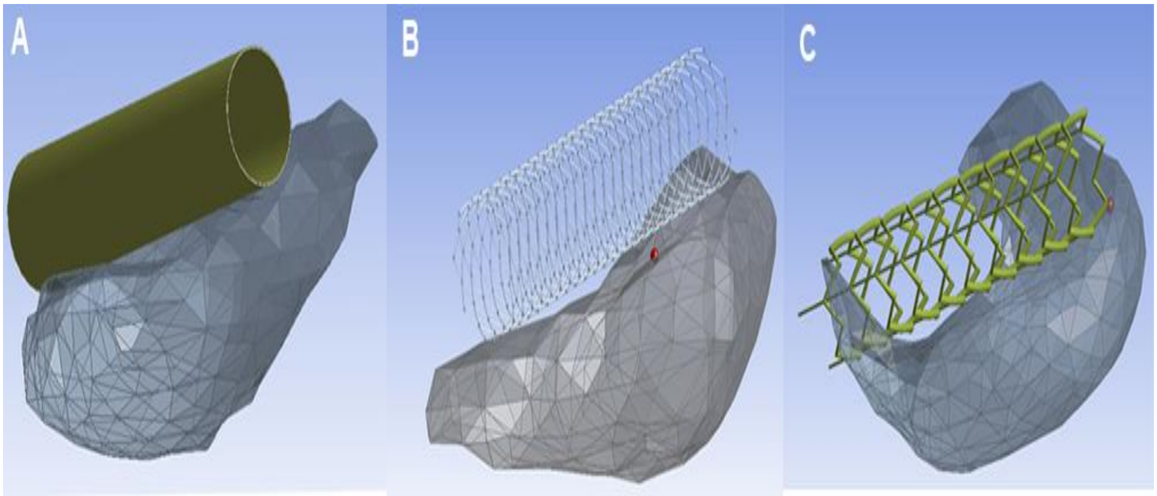

Figure 6.6. Sterling Balloon (A) and two stents: Closed-cell Wallstent (B) and Open-cell Precise (C) three dimensional design.

6.4. Finite Element Analysis and Simulation

An advanced interventional endovascular CAS angioplasty consists of three steps that starts with pre-dilation balloon to open the artery and pushes the plaque followed by self-expandable stenting that fits to the arterial wall and finally post-dilation balloon placement in order to adjust the previously expanded stent. In this study we performed a patient-specific modeling and simulation for the balloon and stent expansion as a separated structural configuration. Therefore, we performed two independent FEM simulations for balloon and stent. In many cases of previous studies the “failure” is defined as the ultimate fracture of the whole plaque [59], [60], however we defined the “failure” as initial intimal plaque rupture. Since, “vulnerable” is defined as a considerable amount of internal stress resisting the break, thus vulnerability has direct correlation with the stress imposed on calcification [60]. Therefore if the plaque has a part protruded or indented then the failure could happen from that part in which we take the ultimate internal stress of the calcification into consideration at that moment.

The whole technical workflow starts with segmentation of the arteries from DICOM CT images using Mimics (Materialise, 10.01, USA). Among all the lesions inside the artery, depending on local geometry, location and feasibility of stenting we chose one or two calcified plaque for segmentation. Selected lesions are mostly resided inside or in the entry of ICA bifurcation. Reconstructed geometry is stored as an STL file in order to apply thickness and volume in the next step. Calcifications inside the left carotid artery are visible in CT image of a patient in Figure 6.7.

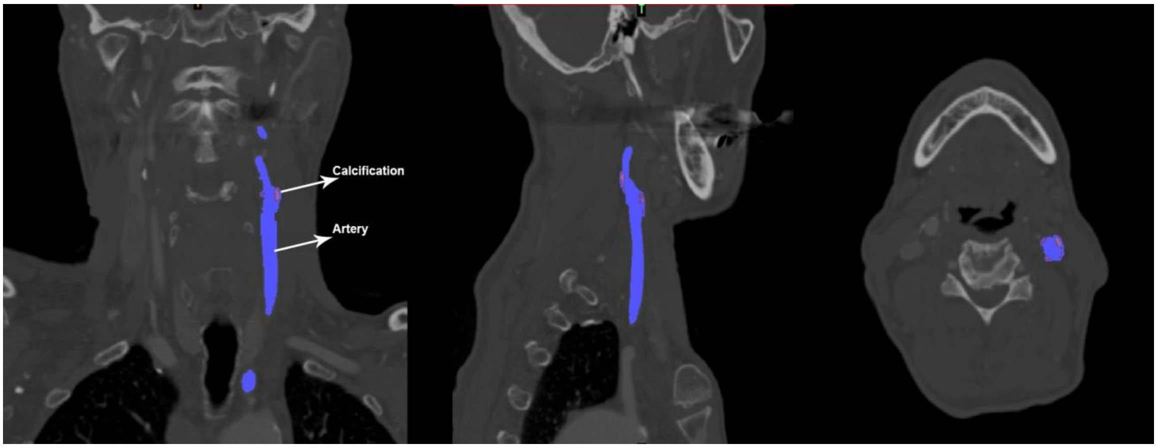

(a) (b) (c)

Figure 6.7. CT image belongs to a case where left carotid artery along with the calcifications are visible. Both artery and the calcified plaque are segmented for further construction in coronary (a), saggital (b) and axial view (c).

Three dimensional open surface geometry is constructed as STL which using Rhinoceros (Robert McNeel & Associates, 5.8, USA) it is converted to a closed polysurface volume or solid NURBS. Since STL file is made of a triangular mesh, after volume creation, arterial body and the calcified plaque is detached. By using merge mesh methods, we connect the meshes in order to prevent the cavity that is emerged between the plaque and the arterial wall. Final volumes are stored as IGS files in order to be imported in the assembly part. Followed by arterial segmentation and reconstruction, we designed the balloon (Figure 6.6-A) and two stents models (Figure 6.6-B, C) deploying predefined geometry properties presented in section II.B. We then assembled artery and calcification volumes with the modeled stents and balloon according to the patient data by employing Solidworks (Dassault Systèmes SolidWorks Corp., 2013, Vélizy, France). As shown in Figure 6.6, balloon and stents are designed fixed above the calcification and spaced 0.15 mm from the surface.

FEA is performed through commercially available software Ansys (Ansys, Inc. 15.0, USA). We used nonlinear static structural analysis to perform the simulation, due to simplicity in analysis by applying structural loads and neglecting inertial forces. Likewise we looked into a global response of the structural system by assuming the loads for both balloon and stent placement over >1s of time. Utilizing FEA application consists of three major procedures. First material properties are defined in which we employed nonlinear hardening material definition for artery, calcification, stents and the balloon. Next geometry properties of each material are specified through the configuration assembled previously. Arterial wall is extruded for 1 mm layer thickness that represents three arterial layers i.e. intima, media and adventitia. One of the most important criteria which affect the final result is the distance of each calcification and the arterial wall and it is completely patient-specific.

In the modeling, we defined boundary conditions to describe the simulation. The boundary condition defined for balloon/stent is symmetrical in axial direction of the Cartesian coordinate system in order to characterize evenly distributed loads and to force a symmetric expansion. Cylindrical support is defined to confine the expansions only to axial and radial direction, but not circumferential direction and prevent rigid body motion. We defined a frictional connection between the balloon/stent and the calcified plaque with frictional coefficient of 0.2 for balloon-plaque and 0.4 for stent-plaque respectively using Augmented Lagrange formulation that have been obtained through sensitivity testing. Calcified plaques are in contact with the artery using a bonded connection. Free displacement is applied on the calcified plaque since clinically it is free to move in any direction as long as limited inside the arterial layers. On the other hand, fixed and elastic support are defined for arterial walls, however it is allowed to stretch and having relatively damping effect. Damping effect is given to the arterial wall by defining stiffness foundation of 0.1 N/mm^3.

Loading condition is defined by applying external radial load on inner surface of balloon and stents. Balloon expansion configuration is resembled as 6-10 atm of the pressure into the balloon continuously pushing the calcified plaque for 30s. In terms of stent, since it is self-expandable, it instantly opens soon as taken out from angioplasty catheter. Tetrahedrons patch conforming meshing is utilized for the whole configuration with minimum element size of 0.1 mm for calcification and 0.4 mm for other parts because of being less significant except the contact region in which location-specific meshing configuration is applied for both contact and target bodies. Figure 6.8 expresses mesh configurations of Case 4 for balloon/calcification. Panel (a) shows finer mesh size for only the calcification comparing to panel (b) with coarser mesh. Results for both mesh size have been described in chapter 7.

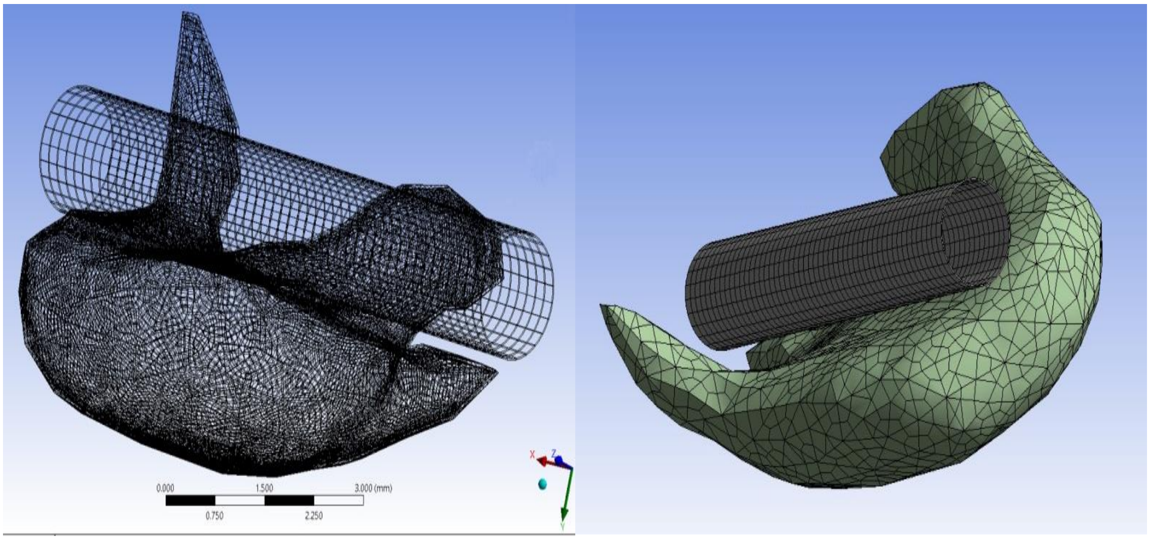

(a) (b)

Figure 6.8. Mesh view of balloon placed on calcification for Case C4. (a)Finer mesh size is utilized for the calcification where (b)Coarser meshing has been defined for calcification. Mesh element size for balloon is coarser comparing to calcification due to priority in importance of the objects in the analysis. Contacts area has the same mesh configuration.

As mentioned before two types of coordinate systems are defined depending on types of loads and supports that have been identified. Figure 6.9 shows two types of coordinate systems comprises cylindrical system that is used for supports and confining the displacements of the objects and Cartesian coordinate system to define loads and symmetrical boundary condition.

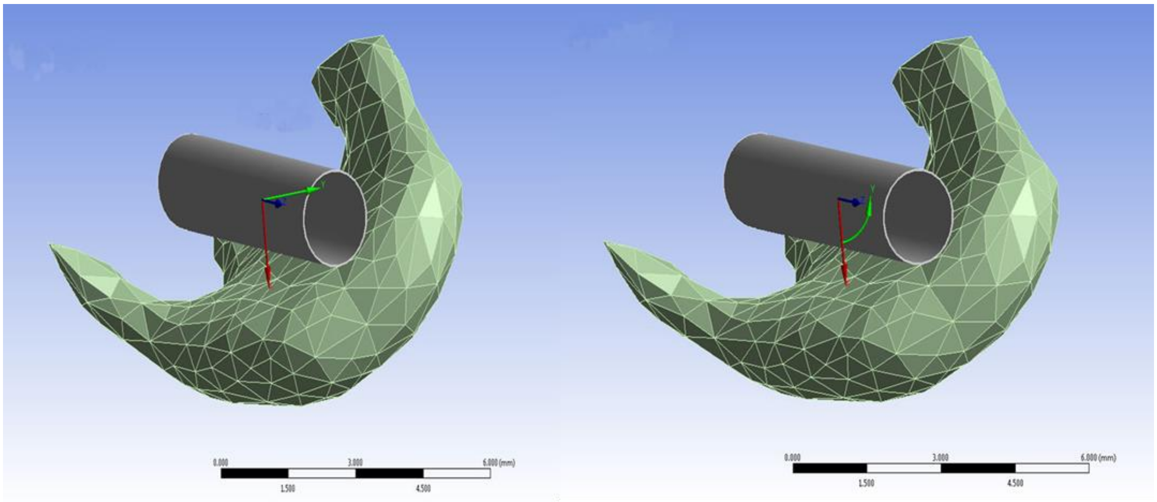

(a) (b)

Figure 6.9. (a) Cartesian coordinate system (b)Cylindrical coordinate system

The geometrical specification and properties that were mentioned in the previous section has been presented in the following Figure 6.10.

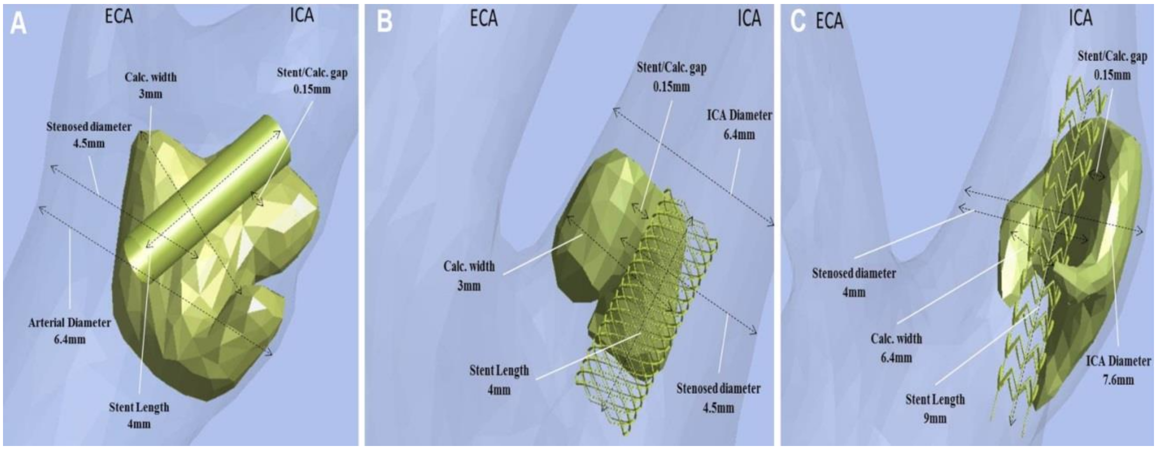

Figure 6.10. Geometrical properties of the modeled balloon and stents are presented. External Carotid Arteries (ECA) and Internal Carotid Arteries (ICA) are shown along with the calcification resided in the entry of ICA. Panel (A) shows pre-dilation balloon placed on calcification and in Panel (B) designed closed-cell Wallstent is presented. In Panel (C) open-cell Precise stent is fixed on a case with particular calcification.

Finally in the following Figure 6.11, a sample of loading condition is presented. As mentioned, the force is imposed on the X direction of the predefined cylindrical coordinate system in order to push the inner faces of the stent and open it and press the calcified plaque. The force has been obtained through an approximation of guidance pressure multiplied by the cross-sectional area and by using trial and error it has been finally determined for each case and it is case specific.

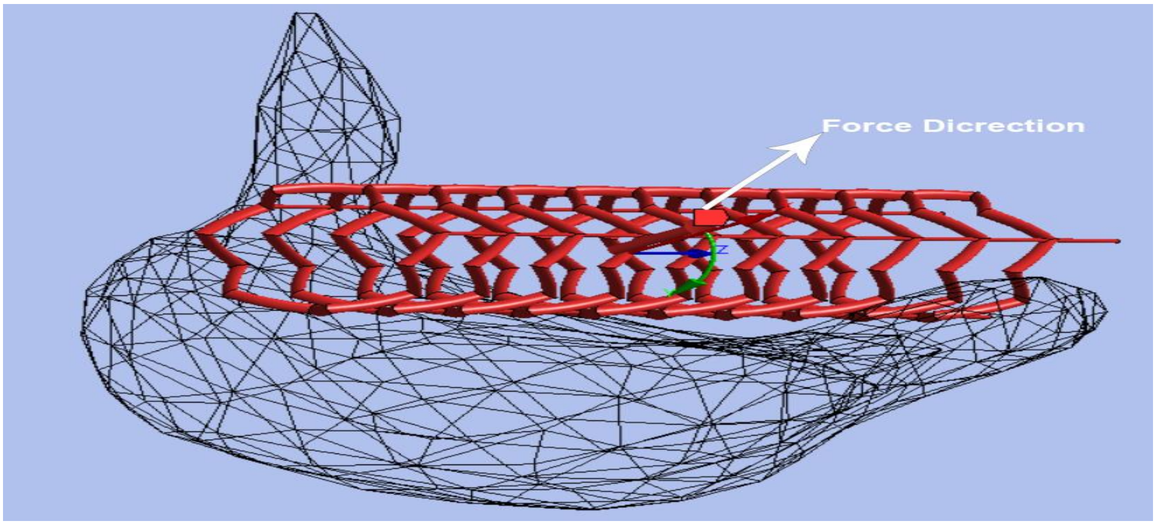

Figure 6.11. Loading condition defined on the inner surface of the stent to be pushed and opened. The force is imposed on the x direction of the cylindrical coordinate in this case. The force has been obtained through an approximation of guidance pressure multiplied by the cross-sectional area and by using trial and error it has been finally determined for each case and it is case specific.

Chapter 7 : Results

7.1. Arterial Diversity

We demonstrated coronal view of carotid artery bifurcations belonging to twelve patients out of twenty cases we acquired, categorized by the largest to smallest calcification directly segmented from the CT images to show diversity in the local geometry (Figure 7.1). Diversity of the arterial local geometry is evident in Figure 7.1, as such the largest calcifications are correlated with the larger arteries.

Figure 7.1. Overall coronal mesh view of the segmented arteries and calcification from CT images belonging to 12 cases out of 20 cases. Yellow objects express calcifications.

7.2. Plaque imposed by Balloon

Here mechanical parameters obtained from imposing balloon on calcified plaques are presented in terms of both quantitative and qualitative results. Imposing the maximum and average ultimate external pressure as 1.5MPa and 1.11 ± 0.31MPa to expand the balloon, we obtained the maximum and average ultimate stress of 120kPa and 55.7 ± 41.2kPa on the calcifications respectively. Average elastic and plastic strain were 0.03±0.02 and 0.006±0.01. We indicated patient-specific Plaque Wall Stress (PWS) which was defined as shear stress on cross-sectional area of arterial layer and calcification when is in dynamic contact with balloon/stent. Maximum and average PWS was equal to 44kPa and 19.03±16.05kPa. TM is also calculated with respect to obtained mechanical parameters using Equation 5 with average of 0.68±1.17MPa. Expanding the balloon by imposing maximum external load, we did not encounter rupture in arterial wall whereas except 3 cases with balloon rupture, all the other cases led to calcification break.

Next we statistically analyzed the relationship between material properties of the calcification i.e. Ca score, EM and obtained mechanical parameters i.e. ultimate stress, PWS using nonlinear Spearman’s correlation to find the most influential material characteristics in calcified plaque rupture. However Ca score is obtained for all the lesions inside an artery, while EM is calcification-specific, hence practically it conveys stronger correlation (See Chapter 8). Therefore in Table 2 we summarized average values for each parameter and its correlation (indicated with R) with EM. There was a strong positive correlation between EM and ultimate stress (0.58; *P=0.008*) as well as EM and PWS (0.66; *P=0.002*). We can state that calcified plaques with larger EM when imposed by maximum pressure, have higher ultimate stress and PWS, consequently it is stiffer and more resistance to rupture.

Parameters	Average values	Correlation with EM
Ultimate external force	1.11±0.31 MPa	R= 0.62; *p=0.005*
Ultimate Stress	55.7±41.2 kPa	R= 0.58; *P=0.008*
Plaque Wall Stress	19.03±16.05 kPa	R= 0.66; *P=0.002*
Elastic Strain	0.03±0.02	R= -0.56; *p=0.005*

Table 7.1. Average mechanical parameters from balloon simulation and their correlation with elastic modulus. (statistically significant threshold, $p<0.05$)

In Figure 7.2, scatter graph is plotted to demonstrate the relationship between EM and ultimate stress/PWS for twenty data pairs imposed by balloon.

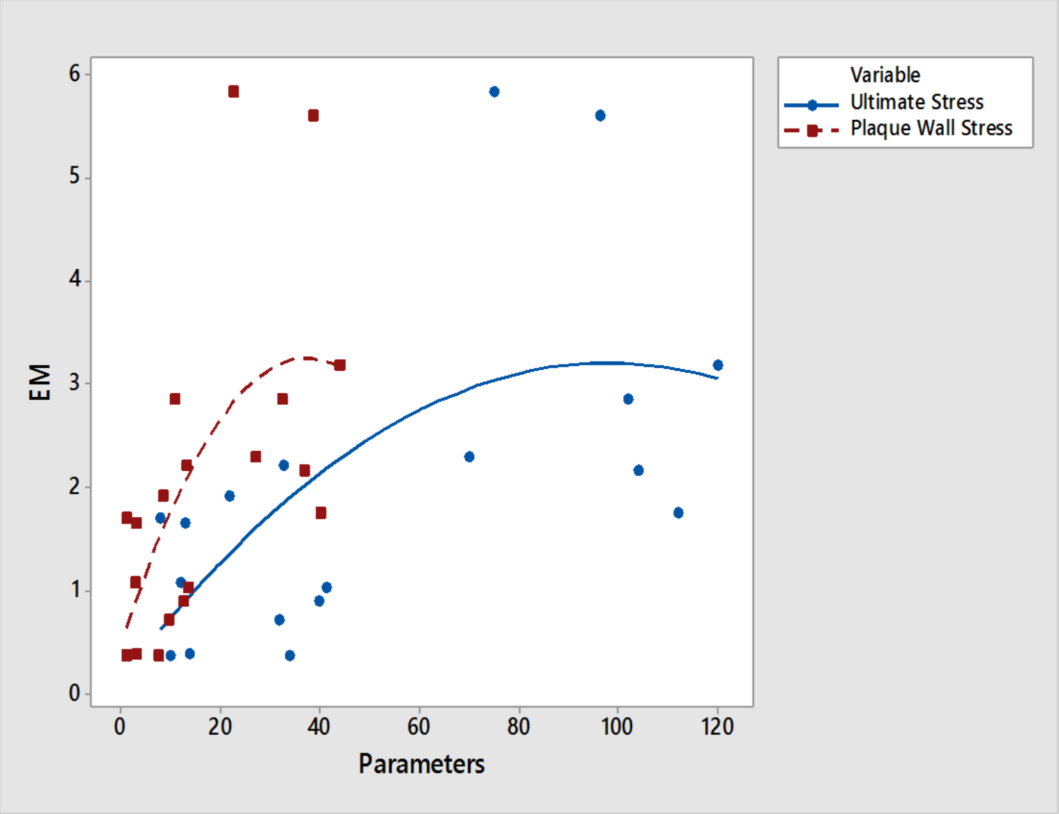

Figure 7.2. Scatter plot for EM v.s. ultimate stress and PWS for balloon analysis. Quadratic regression curves are also depicted to fit the intercepts. Strong positive correlation is inferred from the graph.

In Table 7.2, mechanical parameters belong to all the cases that are obtained by calcified plaque imposed by balloon are presented in the order of largest CA score to the smallest. The cases with plastic strain equal to zero indicate that the nonlinear deformation has not reached through balloon expansion, due to contacts and material properties of the balloon and each calcification.

Patient NO	Load at break (MPa)	Max von mises stress (KPa)	Max Elastic strain(mm/mm)	Plastic strain(mm/mm)	Tangent Modulus (MPa)	Plaque Wall stress (KPa)
1	0.8	116	0.02	0.003	3.5	50
2	1.5	96.42	0.00	0.02	2.4	38.78
3	1.1	32.8	0.01	0	0	13.22
4	1.3	99.7	0.006	0.013	4.92	24.1
5	1.1	32.6	0.009	0	0	11
6	1.5	120	0.03	0	0	44
7	0.8	13	0.009	0.001	1.01	3.2
8	1.5	104	0.04	0	0	37
9	0.8	22	0.01	0	0	8.5
10	1.4	70	0.02	0	0	27.2
11	1.5	112	0.04	0.035	1.05	40.2
12	0.7	12	0.09	0	0	2.9
13	1.3	40	0.04	0	0	12.8
14	0.6	12	0.004	0.012	0.47	1.2
15	1.5	102	0.03	0	0	32.6
16	1.1	41.3	0.03	0.032	0.18	13.5
17	1	14	0.03	0	0	3.3
18	1	34	0.08	0.009	0.33	7.7
19	1.1	32	0.04	0.002	0.9	9.6
20	0.6	10	0.02	0	0	1.26
Avg	1.11	53.36	0.063	0.035	0.68	19.03

Table 7.2. Mechanical parameters obtained for each patient by imposing balloon on the calcified plaque.

Finally we presented quantitative analysis of all the obtained mechanical parameters from imposing loads on calcification by balloon in the following graphs. The graphs in Figure 7.3 represent (a)ultimate stress, (b)PWS, (c)elastic, (d)deformation and (e)plastic strain came from outcome of 12 cases. In Figure 7.3 panel (f) we also presented the standardized amount of Ca score and ultimate stress in order to show the standardized normal correlation between two parameters. As can be seen, most of the cases have direct correlation between Ca score and ultimate stress.

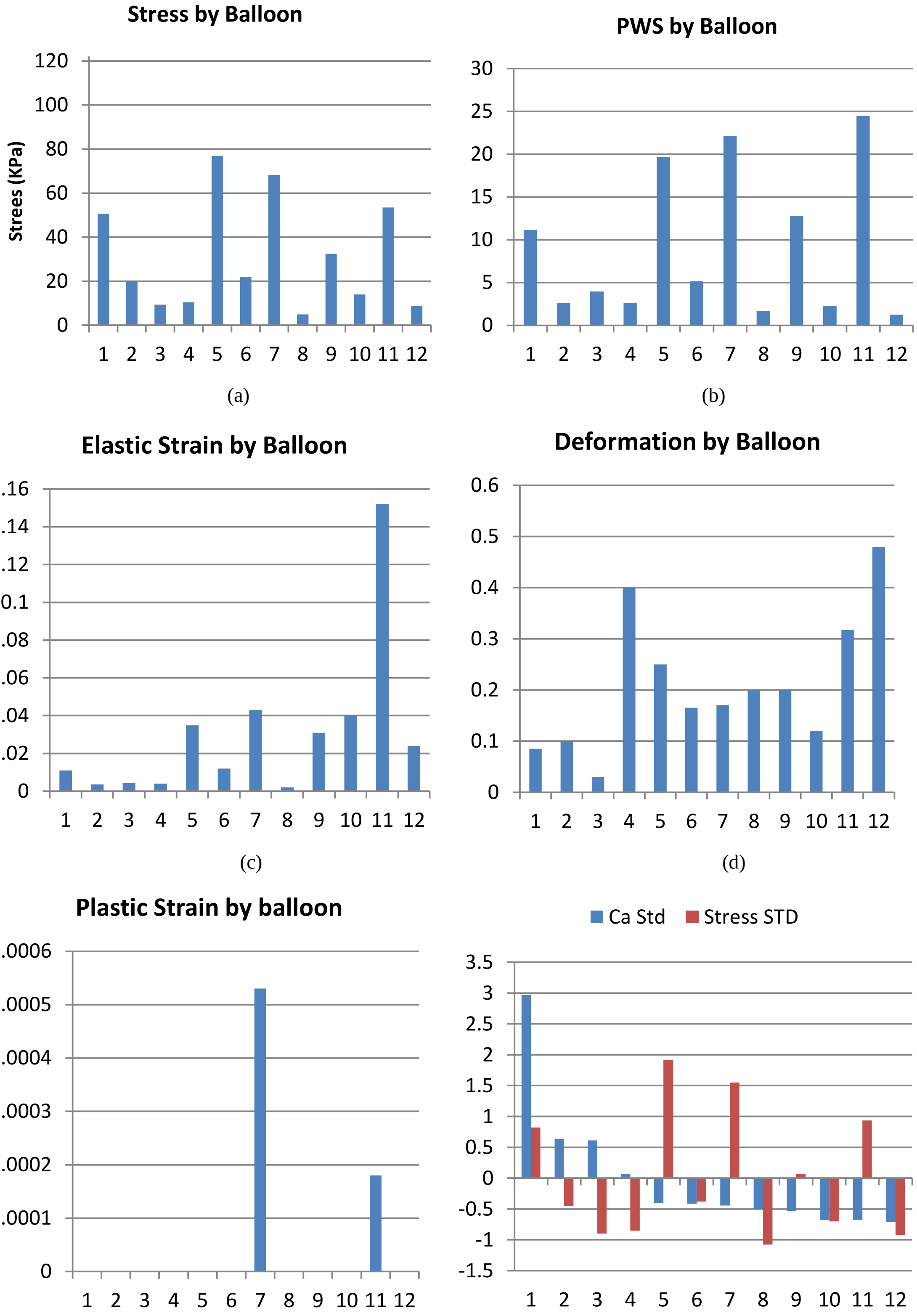

(a) (b) (c) (d) (e) (f)

Figure 7.3. Mechanical parameters of (a)ultimate stress (b)PWS(c)Elastic strain(d)Deformation(e)Plastic strain(f)standardized Ca score and ultimate stress for 12 cases imposed by balloon.

7.3. Plaque imposed by stent

The same analysis has been performed for both open-cell and closed-cell stents to find the maximum pressure imposed on stent and ultimate parameters of the calcified plaques. Quantitatively, ultimate stress on the calcifications is increased notably comparing to balloon expansion. Since the ultimate stress is dependent upon material of contact object, surface friction, temperature, therefore number of calcified plaque reached to plastic domain is increased. Maximum and average ultimate stresses were 492kPa and 171±145kPa respectively. Maximum and average ultimate external load at break were obtained as 4.2MPa and 2.32±1.16MPa obviously showing a huge difference comparing to balloon. PWS caused by stent expansion were 208kPa and 64.3±63.3kPa for maximum and average values. We obtained average elastic and plastic strain as 0.08±0.06 and 0.03±0.04 which were significantly increased due to stent interaction. We specifically computed the penetration of the stent inside the calcification with average of 0.03±0.04mm in which helps in calculation of patient-specific plaque protrusion. Slope of the plastic deformation (TM) was increased to 1.19±1.47MPa. Table 7.3 shows the average values for each mechanical parameters and their correlation with EM. The Spearman's coefficient between EM and external load was significantly increased to 0.71 ($p=0.001$). Likewise correlation between EM and ultimate stress and then PWS were 0.85 ($p<0.0001$) and 0.92 ($p<0.0001$) respectively, which comparing to balloon we obtained much stronger and positive correlation. We can infer the same interpretation for balloon here as the higher the EM of the calcification, higher the ultimate stress hence less susceptible to rupture. Scatterplot in Figure 7.4 depicts the stronger relationship comparing to the balloon between EM and ultimate stress/PWS.

Parameters	Average values	Correlation with EM
Ultimate external force	2.32±1.16 MPa	R= 0.71; $p=0.001$
Ultimate Stress	171±145 kPa	R= 0.85; $p<0.0001$
Plaque Wall Stress	64.3±63.3 kPa	R= 0.92; $p<0.0001$
Elastic Strain	0.08±0.06	R= -0.72; $p<0.0001$

Table 7.3. Average values for mechanical parameters obtained from stent simulation and their nonlinear spearman's correlation with elastic modulus. (statistically significant threshold, $p<0.05$).

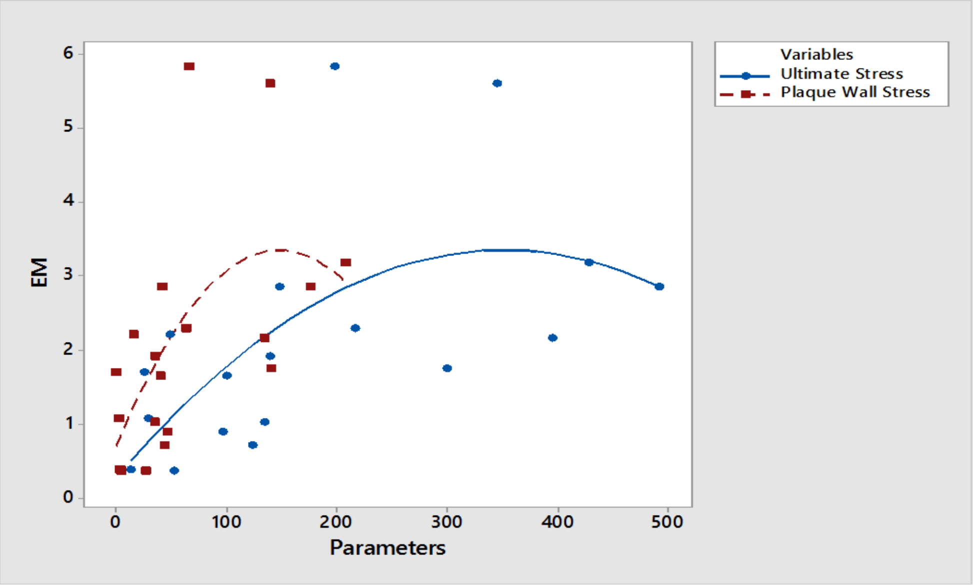

Figure 7.4. Scatter plot for EM v.s. ultimate stress and PWS for stent simulation. Quadratic regression curves show better data fit for stent analysis whereas comparing to balloon expansion monotonic pattern is well demonstrated.

In Table 7.4, mechanical parameters belong to all the cases that are obtained by calcified plaque imposed by stent are presented in the order of largest CA score to the smallest. The cases with plastic strain equal to zero indicate that the nonlinear deformation has not reached through balloon expansion, due to contacts and material properties of the balloon and each calcification. Comparing to balloon expansion, values for the stress/strain and TM are significantly increased and this proves the fact that the ultimate mechanical parameters strictly depends on contacts, material properties and cross-sectional area of the objects being in contact with eachother.

Patient No	Load at break (MPa)	Max von mises stress (before break) (KPa)	Max elastic strain (mm/mm)	Plastic strain (mm/mm)	Max Penetration of stent in Plaque (mm)	Tangent Modulus (MPa)	Plaque Wall stress
52	3	112.23	0.0241	0.0027	0.000543	1.95	49.9
33	4.2	344.91	0.029168	0.04280	0.000243	4.3	139.143
68	1.5	49.372	0.021177	0.00000	0.004769	0	16.30163
37	3	198	0.024929	0.012	0.000933	4.83	66.577
71	2.7	147.68	0.051179	0.00136	0.000066	1	41
26	3.8	428.97	0.033593	0.0130	0.000222	2.48	208.615
58	2	100	0.081456	0.02657	0.011476	0.61	40.02906
16	3.5	396	0.066092	0.1070	0.004655	2.53	134
45	1.5	140	0.070274	0.0090	0.014777	0.5	35
56	2.5	217	0.040084	0.0950	0.000239	1.37	63.1
13	3.8	300	0.150390	0.05530	0.015324	0.72	141
59	0.8	29.2	0.025195	0.00000	0.012300	0	2
61	3	96.986	0.094760	0.02570	0.025589	0.64	45.9
44	1.3	25.3	0.013256	0.00000	0.022230	0	0
19	4	492	0.051000	0.13600	0.000935	2.66	176
54	1	135	0.132130	0.08800	0.011626	0.125	35
22	0.9	13.491	0.151075	0.00000	0.121930	0	3.59
66	1	26.87	0.205180	0.00000	0.200000	0	5.16
73	1.7	124	0.147660	0.09280	0.246710	0.184	44
67	1.2	53	0.250000	0.00000	0.021174	0	27.1
Average	2.32	169.8505	1.03E-01	4.41E-02	2.13E-02	1.19	64
Std_dev	1.161487	147.3035	0.060927	0.048578	0.05943	1.47	59.83285

Table 7.4. Mechanical parameters obtained for each patient by imposing balloon on the calcified plaque.

Eventually in this section, we presented quantitative analysis of all the obtained mechanical parameters from imposing loads on calcification by the stents in the following graphs. Figure 7.5, represent (a)ultimate stress, (b)PWS, (a)elastic, (d)deformation and (e)plastic strain came from outcome of 12 cases.

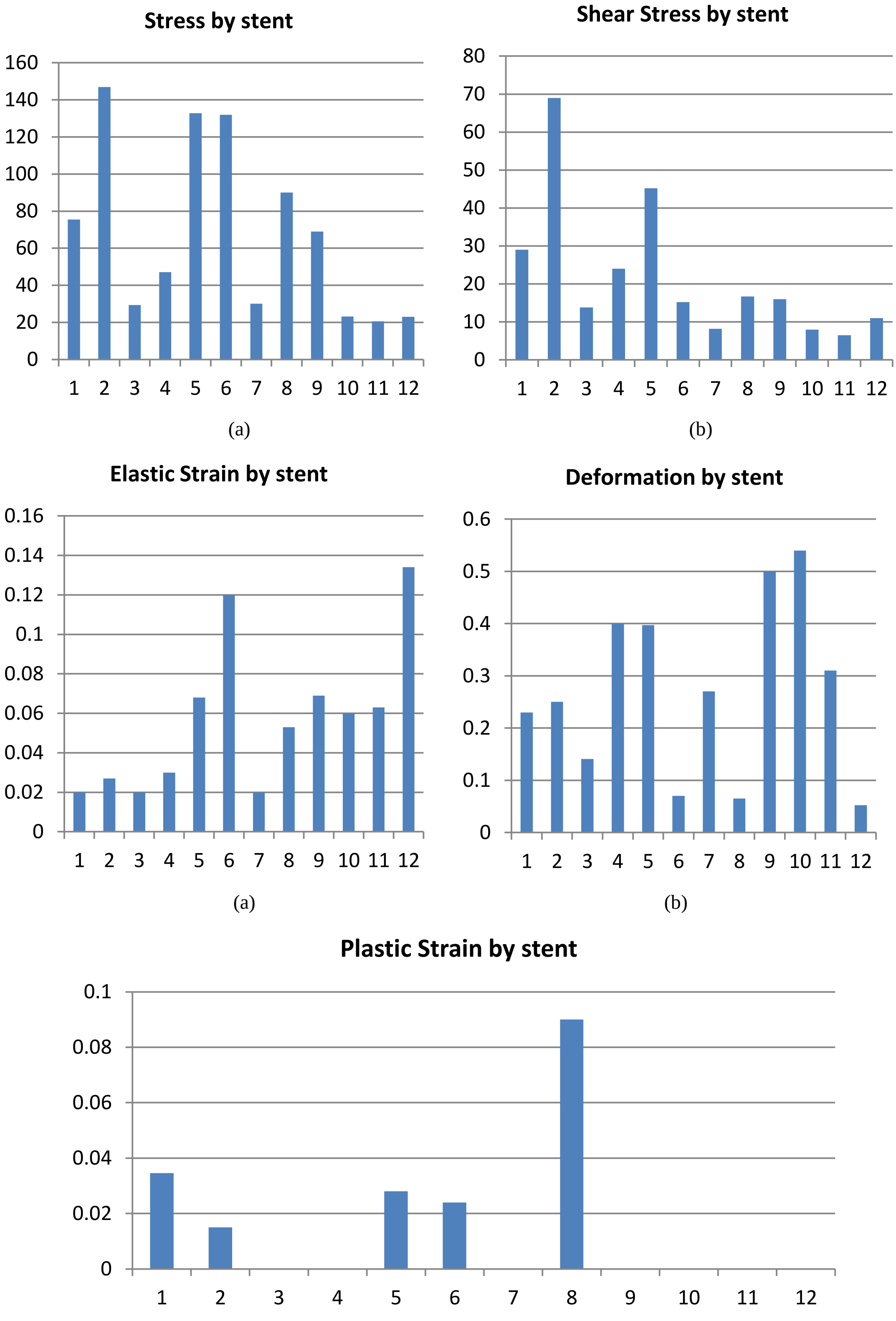

Stress by stent

(a)

Shear Stress by stent

(b)

Elastic Strain by stent

(a)

Deformation by stent

(b)

Plastic Strain by stent

(e)

Figure 7.5. Mechanical parameters of (a)ultimate stress (b)PWS(c)Elastic strain(d)Deformation(e)Plastic strain for 12 cases imposed by stents.

Finally for qualitative evaluation, we presented stress-strain analysis of the calcification imposed by balloon for a case in Figure 7.6. Panel A shows maximum Von mises stress of the calcified plaque resided in the entrance of internal carotid artery after being pushed by balloon. Panels B and C illustrate elastic strain and plastic strain distributed over the calcification respectively. In panel A position of the balloon, ICA, ECA and arterial wall thickness have been specified. Figure 7.7, Top panel A shows UTS as Von mises stress where panel B presents PWS. Panel C demonstrates both plaque/stent rupture in which due to large stiffness of the calcification higher stress level is reached.

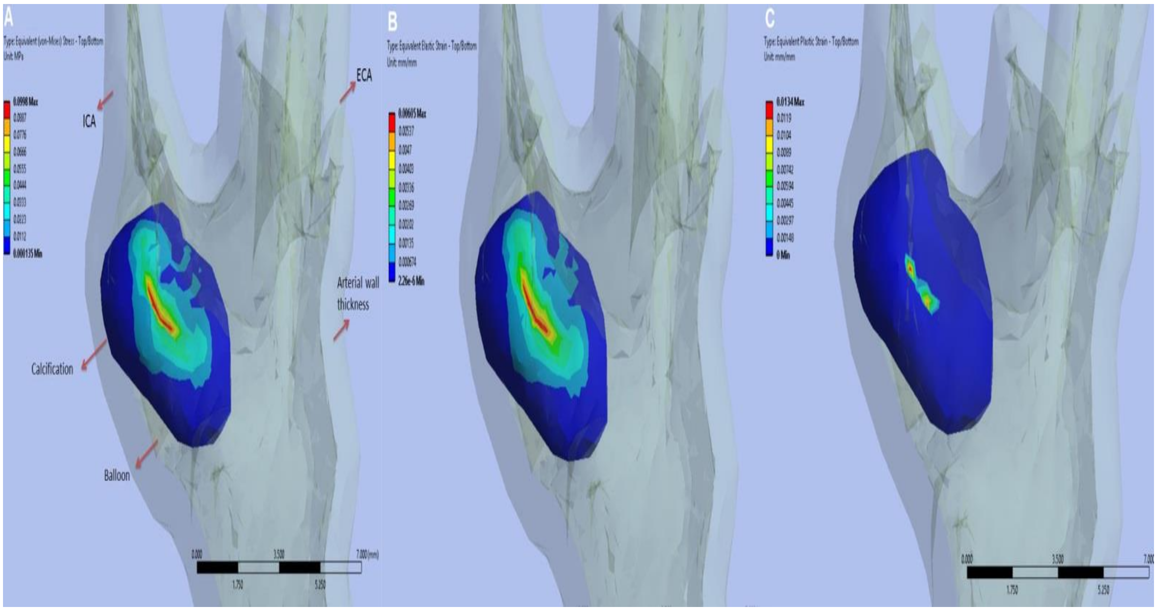

Figure 7.6. Stress-strain analysis for C4. Panel A shows Von mises stress distributed over the surface of the calcified plaque. Expanded balloon is pointed along with the ICA, ECA and wall thickness. Panel B represents elastic strain. Left color bar for strain distribution corresponds to the maximum values in Table 7.4. Panel C belongs to nonlinear plastic deformation occurred in the center of dynamic interaction between balloon and calcification.

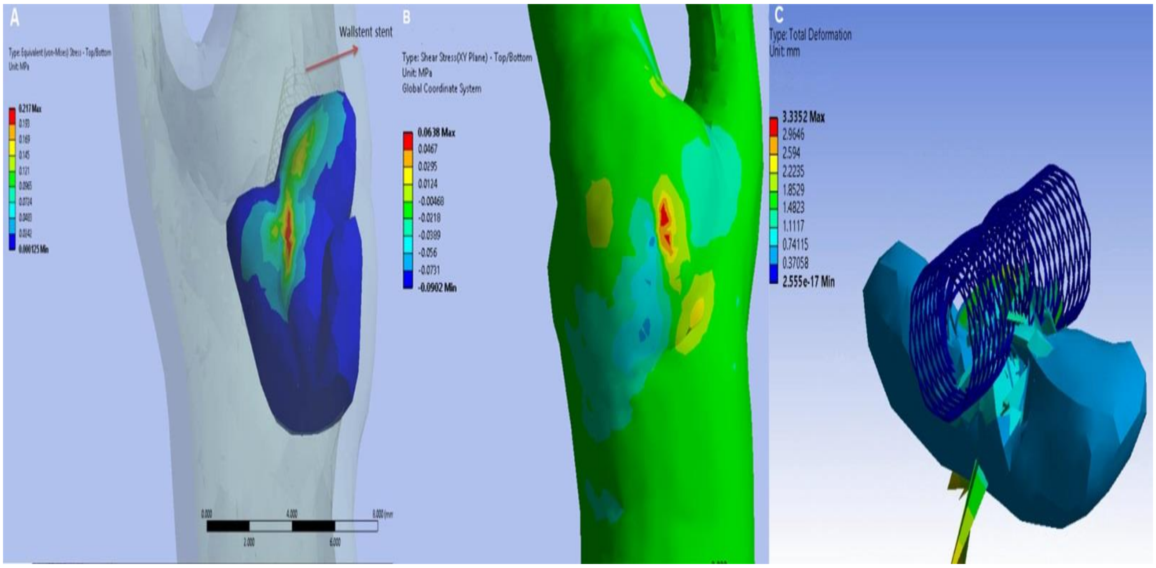

Figure 7.7. Stress-strain analysis belongs to C10. Panel A represents Von mises stress distribution due to wallstent expansion which has been pointed. Panel B shows WSS on the arterial wall. In panel C we presented plaque and stent break due to stiffness of the calcification in which causes to cross the UTS and fail.

Finally for qualitative evaluation, we presented stress-strain analysis of the calcification imposed by both balloon and stent for three different cases in Figure 7.8. Panel A shows maximum ultimate stress of the calcified plaque in the entrance of internal carotid artery after being stented by Wallstent. Panel B illustrates PWS shear stress induced between balloon/arterial wall and calcification. For each case arterial wall thickness is visible in which the calcification is resided under. In panel C we presented plastic strain started from the middle of calcification while stented by Precise stent. Case in panel C is one the rare cases with stent break by having high TM equal to 4.92MPa leading to a stiffer plasticity. Length of the stents and balloon is case-specific and determined according to the cross-sectional area of the calcifications and stent/balloon for simplicity in the calculation. In Figure 7.9 we presented qualitative analysis of both plaque protrusion and plaque rupture. Panel A shows deformation values in a soft calcification where the stent is penetrated inside due to high elasticity of calcification. Panels B and C demonstrate fracture in plaque and stent in which due to large stiffness of the calcification, maximum stress level is reached. The ultimate stress value and its locations after the rupture are indicted in the images.

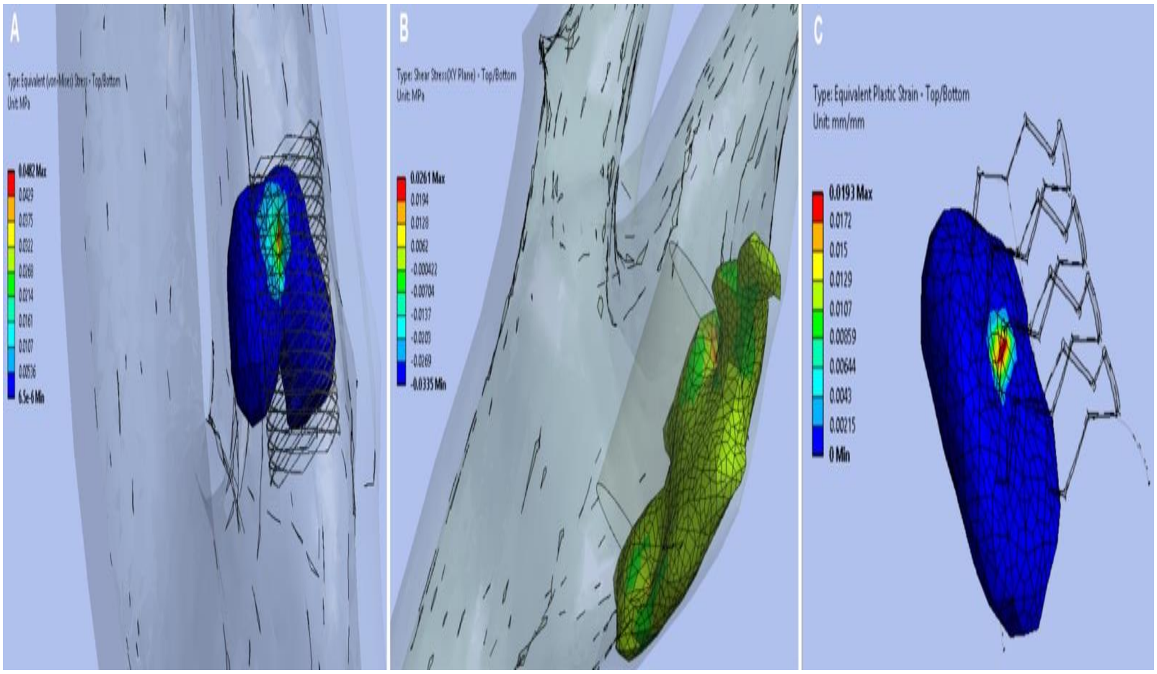

Figure 7.8. Stress-strain analysis of three different cases imposed by balloon and stent. Panel (A) shows equivalent stress from center of the calcification while pressed by closed-cell stent. Panel (B) demonstrates PWS of a calcification on balloon case and Panel (C) represents plastic-strain imposed by closed-cell stent on a case.

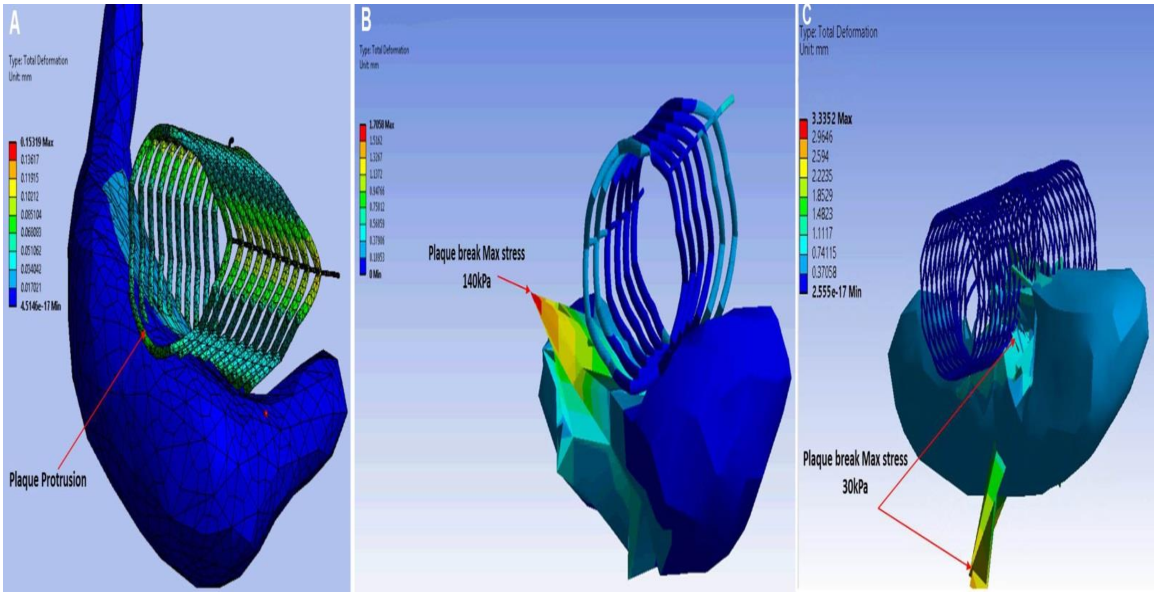

Figure 7.9. Plaque protrusion and rupture are simulated by inducing the ultimate pressure on the stents. Panel (A) shows the plaque is penetrated inside the stent. Panel (B) and (C) demonstrate soft plaque break due to 140kPa and 30kPa of the ultimate stress that crossed the maximum resistance of the calcification.

Finally for the qualitative evaluation, Figure 7.10 shows mechanical parameters obtained on three different cases all by balloon expansion. In panel (a) ultimate stress as equivalent von mises stress is visible in the bottom of calcification when pushed by the balloon. The contact between the arterial layer and the bottom layer of calcification has the largest load. Panel (b), shear stress between calcification and both balloon and the arterial wall are shown which we presented as PWS. In the last panel (c) again the ultimate stress on the calcified plaque by the balloon is shown in which the largest stress has been imposed on the bottom layer of the calcification.

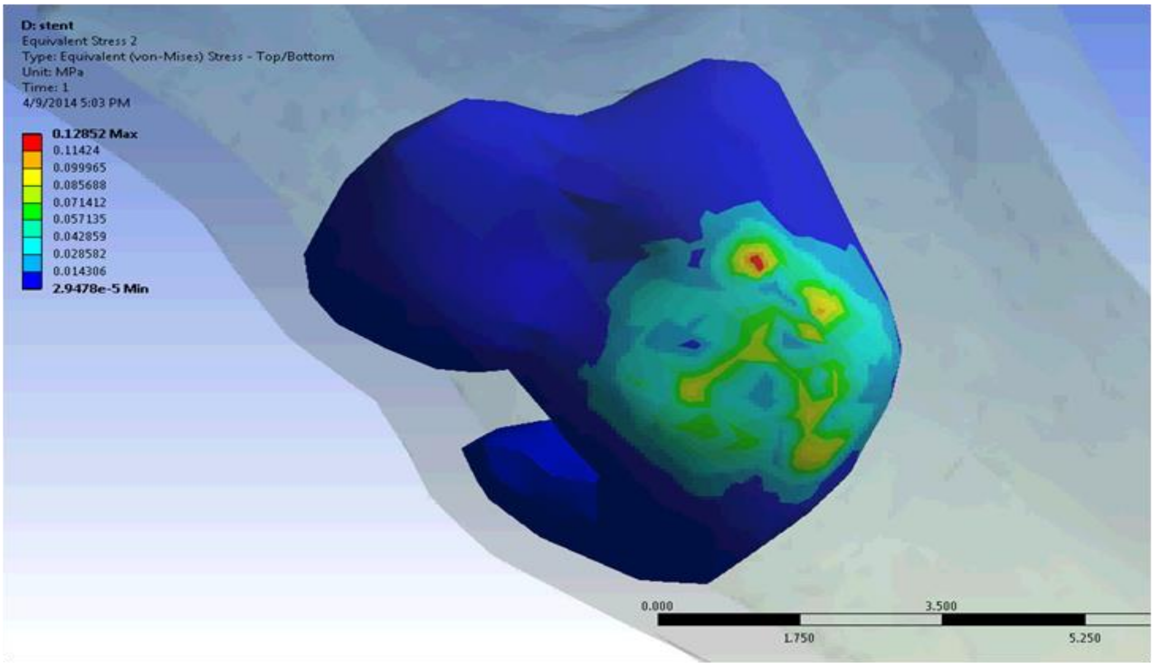

(a)

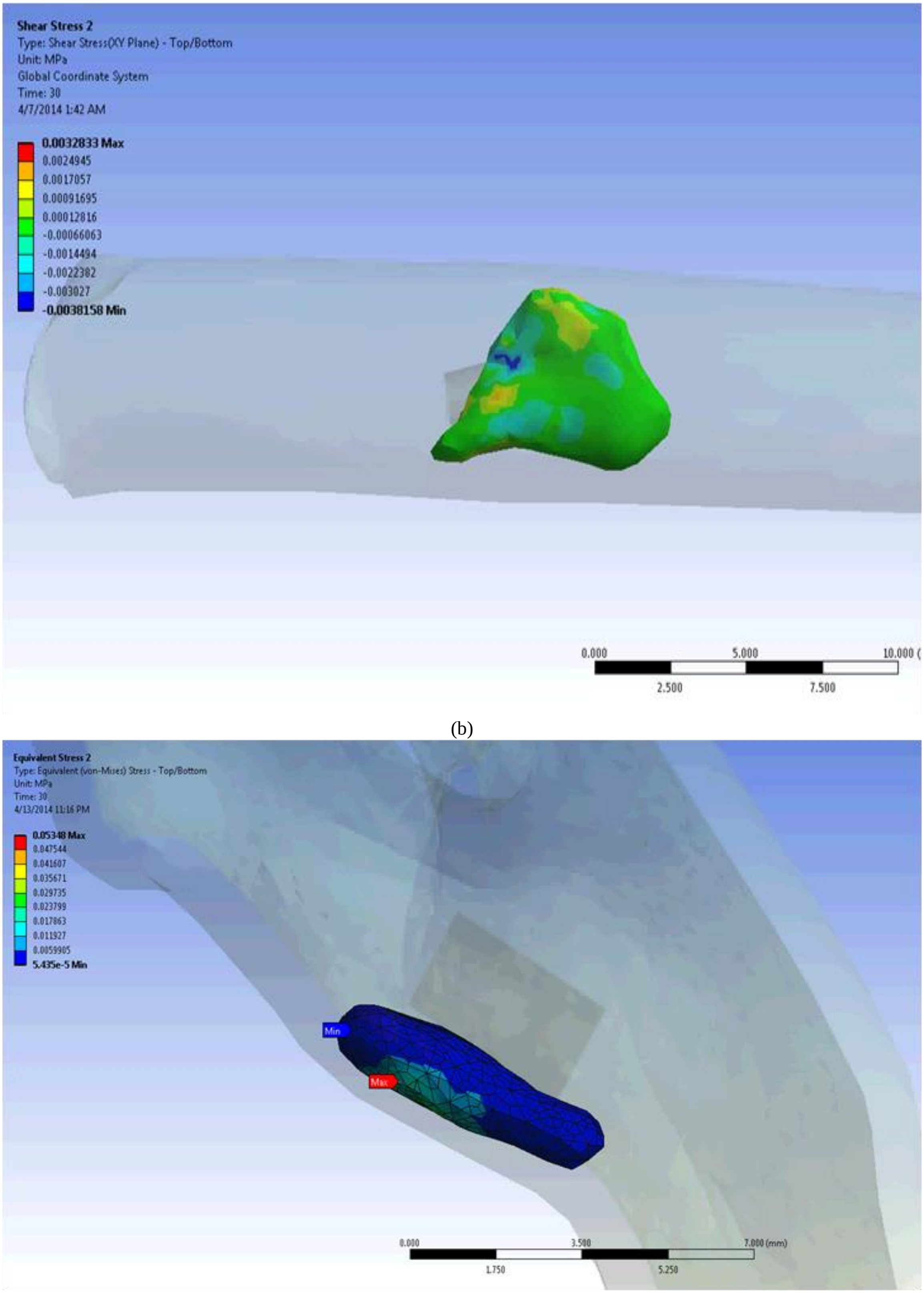

(b)

(c)

Figure 7.10. (a)Equivalent Von mises stress on the Plaque wall being pushed by the balloon. (b)PWS on a plaque in the middle of lumen. (c)stress on the calcified plaque imposed by balloon.

Chapter 8 : Discussion and Conclusion

8.1. Comparison of loads imposed by balloon and stents

In this section we compared all the mechanical parameters i.e. ultimate stress, elastic and plastic strain and PWS obtained for the calcified plaques belong to 12 cases imposed by both balloon and stents. Each panel in Figures 8.1 presents the graphs of comparisons. Panel (a) represents ultimate stress, (b)elastic strain, (c)PWS and (d)plastic strain respectively. As can be seen obviously, parameters obtained for the stents expansions are higher comparing to balloon expansion. The question is that how linear and nonlinear stress/strain are different for one calcified plaque belongs to a patient when imposed by two different objects. This is very normal since when we intend to obtain the ultimate tensile strength or ultimate compressive strength in which we would obtain different stress values on one same object. Likewise, if we employ uniaxial tensile test or biaxial tensile test on a object we would obtain two different results. Therefore we can conclude that the final mechanical parameters definitely depends material properties such as elastic modulus, Poisson's ratio and other material properties, types of contacts and cross-sectional area of the contact.

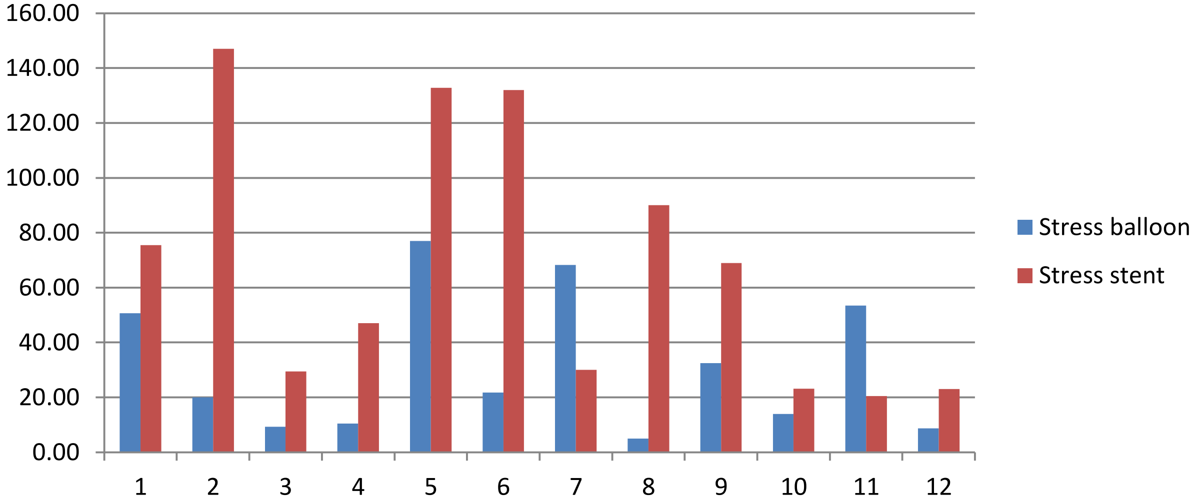

(a)

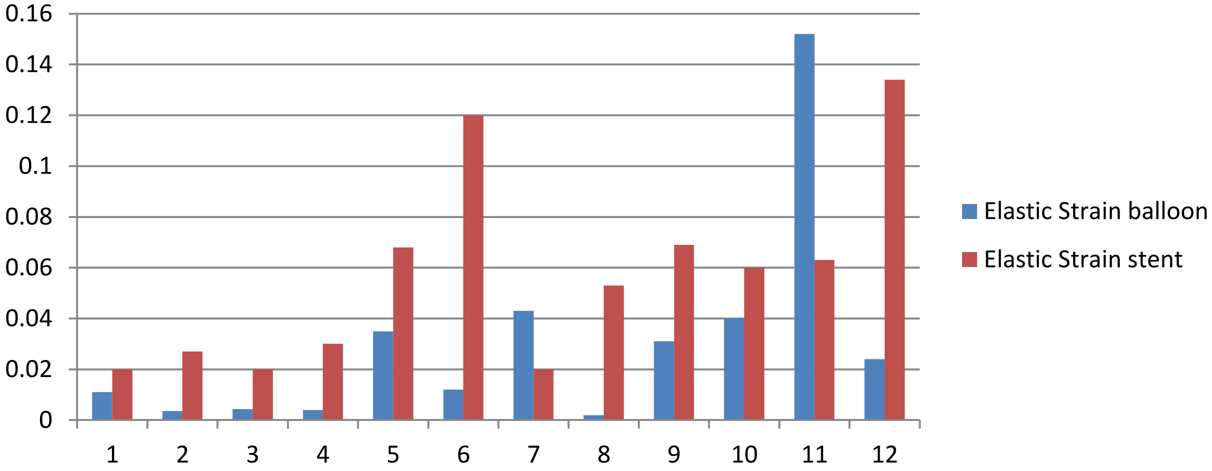

(b)

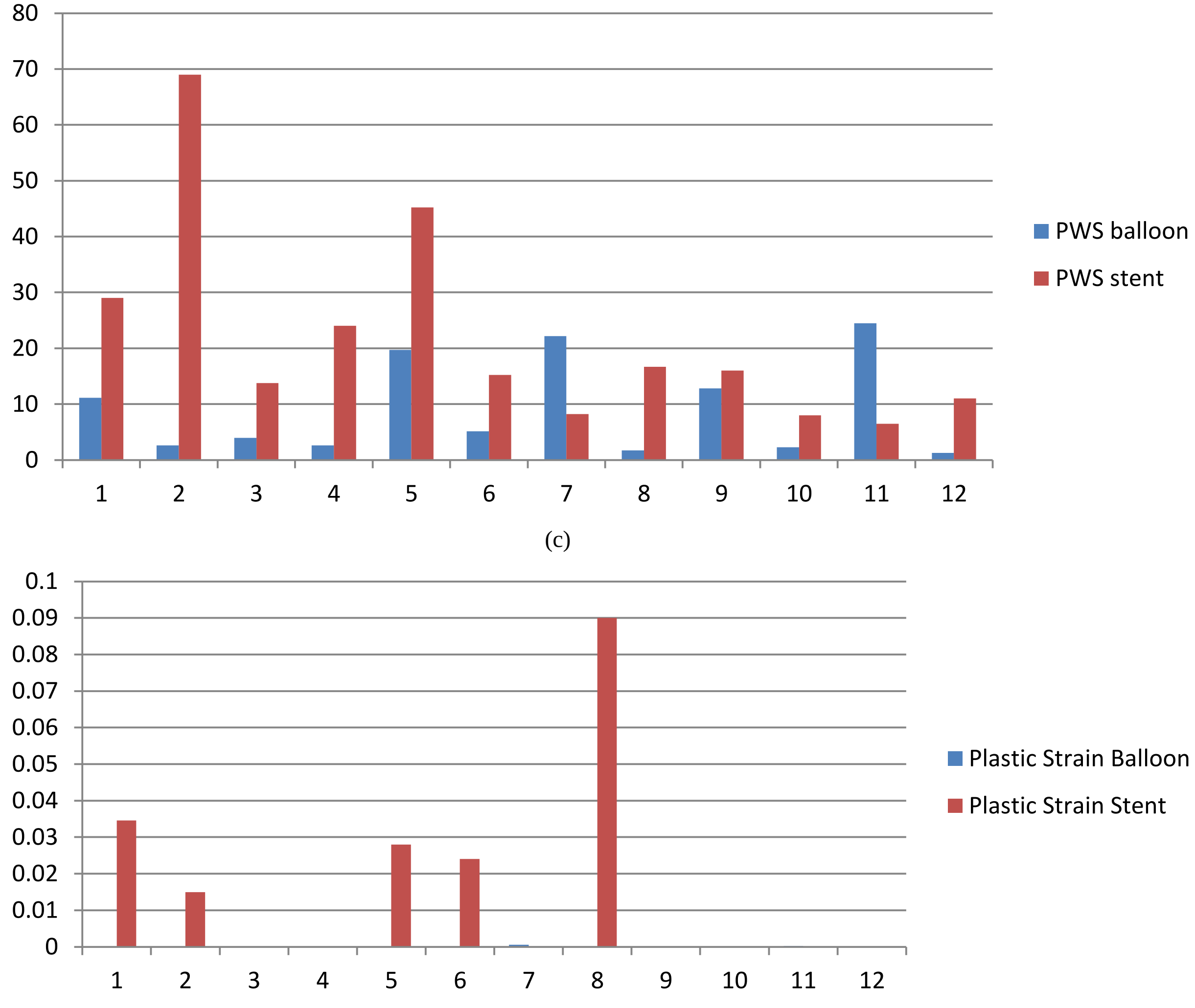

(c)

(d)

Figure 8.1. Graphs representing comparisons of obtained mechanical parameters imposed by balloon and the stents. (a) Stresses (b)Elastic strain (c)PWS and (d) Plastic strain.

8.2. Calcium score

In order to evaluate the ultimate parameters obtained for calcified plaque before break, Wong *et al*. [43] obtained critical stress and deformation of 286.12kPa and 0.239mm respectively on carotid calcified plaque by justifying the plaque rupture stress level threshold of 300kPa. Another study by Zhao *et al*. [44] established maximum stress equal to 75kPa in ruptured calcification. Eventually, Lowlor *et al*. [57] performed an experimental study of atherosclerosis carotid plaque by classifying them based on their stiffness to hard, mixed and soft with respect to their mechanical parameters. Average ultimate tensile stress and strain were reported as 366.6±220MPa and 0.46±0.088 respectively which are insignificantly higher comparing to this work. These data show that the results obtained in the current study in terms of ultimate mechanical parameters fairly correspond to the average overall values in the literature.

Finally we assessed the relationship of several influential material properties of calcification with obtained ultimate mechanical stresses/strains in order to investigate which material characteristics are extremely involved in “plaque vulnerability” and “plaque protrusion”.

As a potentially influential parameter, we investigated on correlation between Ca score and ultimate stress/PWS/external load for stent expansion. Although as mentioned before, in spite of EM that is calcification-specific, Ca score is calculated based on all the lesions inside the carotid artery. Nonlinear correlation between Ca score and ultimate stress was 0.44 ($p=0.057$) followed by PWS that was 0.38 ($p=0.103$) in which shows no significant correlation exists. Likewise, there is no statistically significant correlation between ultimate external load and Ca score in both balloon and stent expansion as shown in Table 8.1 despite EM that showed strong positive relationship (Chapter 3). This is because in reality large calcifications with high Ca score could act as a ductile elastic material and conversely, calcifications with small Ca score might behave as hard brittle material, hence it is not trivial to classify the calcifications base on its Ca score. Another robust reason is that there is an element of “weight” that plays a big role in construction of Ca score in which calcifications with the same range of HU have the same weight in their Ca score [38]. Scatterplot in Figure 8.2 shows week correlation between Ca score and ultimate stress imposed by both balloon and stent before break. Although among the rare probe on Ca score, Nandalur *et al*. [58] statistically found that carotid artery Ca score have clinically significant relationship with degree of stenosis and other cardiovascular risk factor, although as shown in Table 8.1 in terms of mechanical parameters we concluded that Ca score has minor impact on plaque break comparing to EM. However we believe that calculating calcification-specific Ca score instead of One-for-all value could strength the proportion. Although the abovementioned element of “weight” still influences the final correlation.

Mechanical Parameters	Average values	Correlation with Ca score
Ultimate external force	2.32±1.16 MPa	R=0.53; $p=0.089$
Ultimate Stress	171±145 kPa	R=0.44; $p=0.057$
Plaque Wall Stress	64.3±63.3 kPa	R=0.38; $p=0.103$
Elastic Strain	0.08±0.06	R= -0.66; $p=0.012$

Table 8.1. Mechanical parameters obtained from Stent simulation and their nonlinear spearman’s correlation with Ca Score. (statistically significant threshold, $p<0.05$).

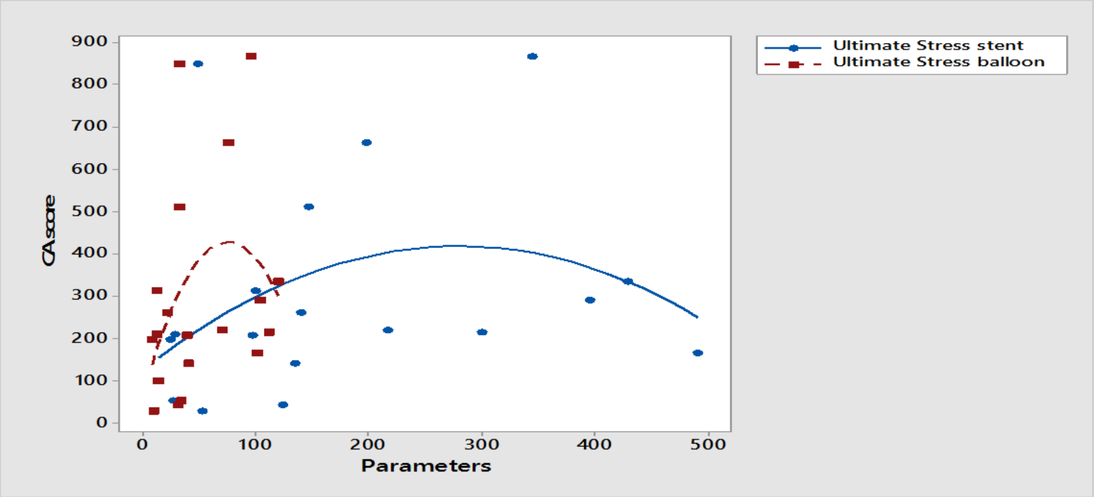

Figure 8.2. Scatter plot showing weak correlation of Ca score and ultimate stress of calcifications obtained for balloon and stent simulations.

In addition to the statistical values obtained above, here we also presented the graph of comparison of real values of the Ca score and HU, Volume score and EM that will be analyzed in the next sections. Figure 8.3 below shows the comparisons for only 12 cases and obviously volume score and HU have direct relation with Ca score. However EM in this graph seems not in the direct correlation for some cases which is totally normal and their statistical relationship has already been explained in Chapter 7. Panel (a) only presents elastic modulus belonging to 12 cases in the order of higher Ca score to the lower CA score. As can be seen relatively the higher Ca score has the case, the higher EM is assigned to that case. C1 and C2, C3 and C4 with the higher Ca score the also have higher EM. Panel (b) shows the proportion of CA score and HU which since they have been obtained through the same equation they have direct correlation. In panel (c) the relation of Ca score and volume score is shown. Similar to HU, since volume score is one of the elements to obtain the Ca score, hence they have positive and direct correlation. Finally in panel (d) standardized values belonging to Ca score and EM are shown. As stated in the latter paragraph, they have relatively direct correlation.

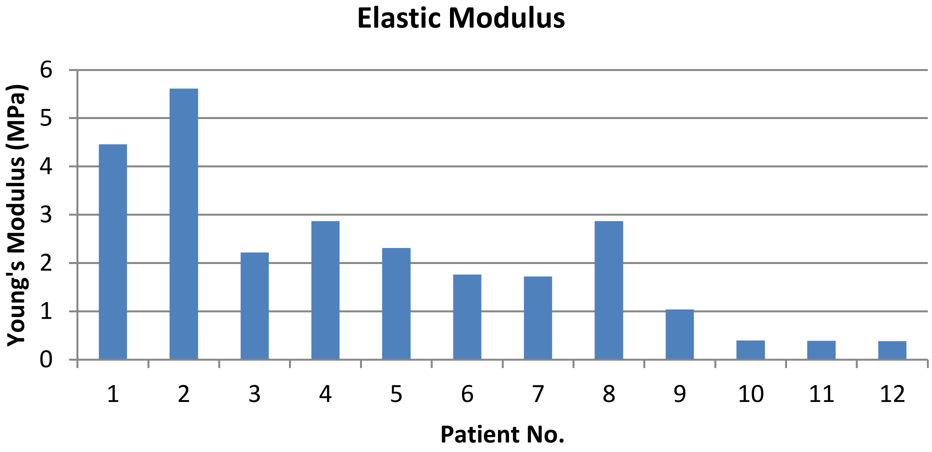

(a)

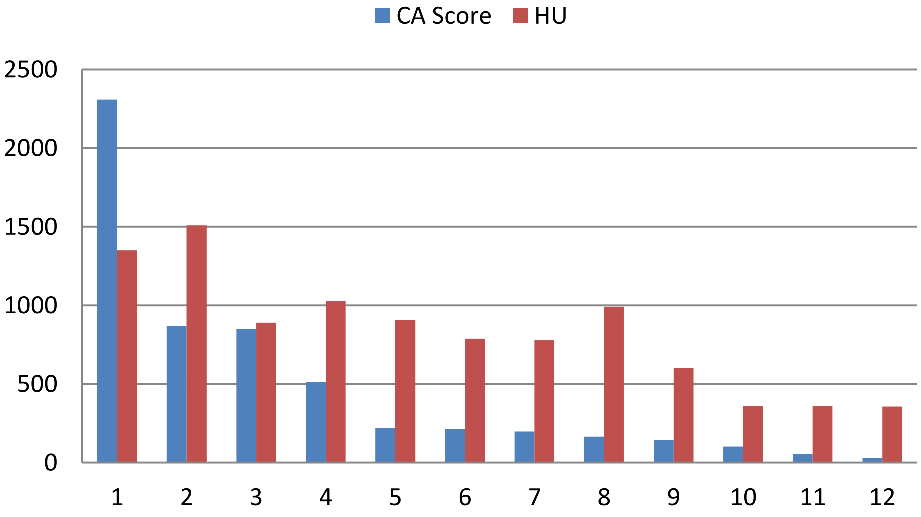

(b)

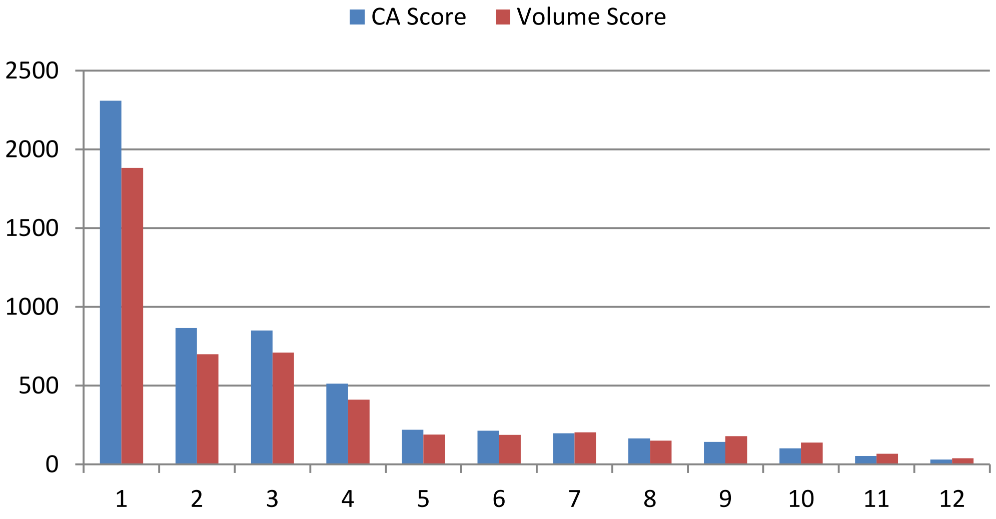

(c)

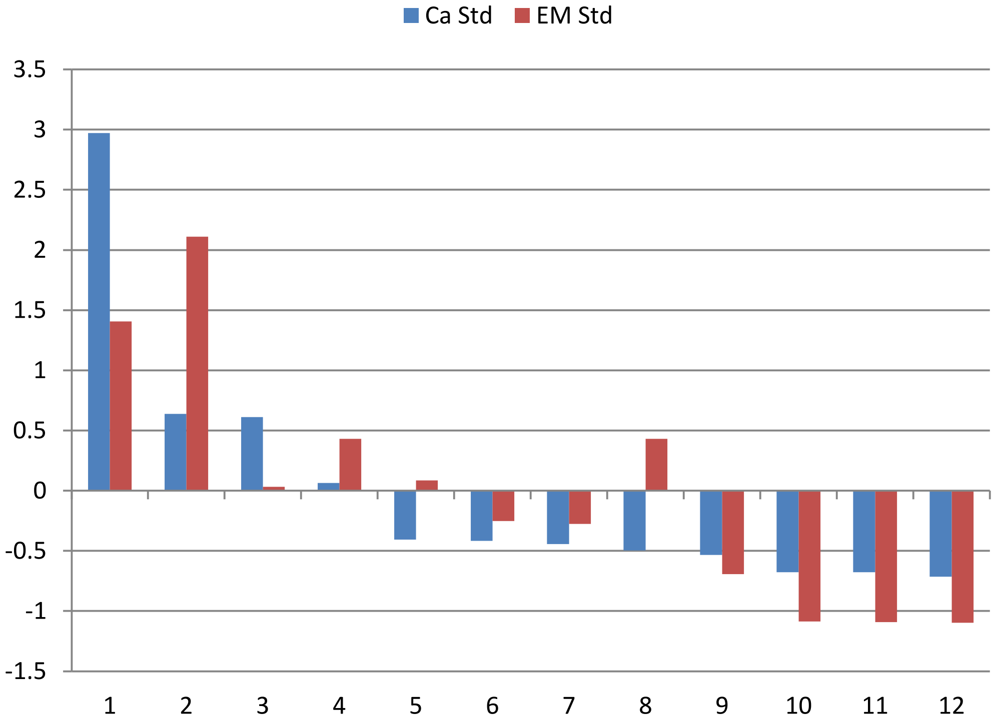

(d)

Figure 8.3. Comparisons of Ca score in correlation with Volume score, HU and elastic modulus. Panel (a) shows only EM belongs to 12 cases, (b) proportion of Ca score and HU, (c)corralation between Ca score and volume score and (d)shows standardized values for Ca score and EM for the sake of seeking the relations.

8.3. Area and Volume score

The most common criteria to define a “vulnerable plaque” is the thickness of fibrous and lesion size. Maldonado *et al*. [59] investigated on cap thickness including calcification in HR-µCT images and confirms 300kPa threshold for cap rupture that correlates it with plaque thickness. Likewise Vengrenyuk *et al*. [60] mathematically proves that calcified plaques smaller than 65µm can reach to an ultimate stress of more than 600kPa. We investigated on correlation between area of calcification and ultimate stress as well as PWS on stent expansion. The Spearman’s coefficient was 0.43 ($p=0.061$) for ultimate stress and 0.39 ($p=0.093$) for PWS respectively, thus the correlations are statistically not significant. The same relationship exists for volume score, therefore size of calcification is not related to its fracture in the current study. This is because we defined the rupture as the initial failure not the ultimate failure and since stress distribution is function of both geometry and mechanical properties of the tissues, thus soon as indentation or protrusion is met between contacts, stress distribution begins to occur leading to plaque susceptibility. We also evaluated the proportion of area of calcification and ultimate external load to know if the size has any impact on external load at break. We obtained spearman’s rho equal to 0.6 ($p=0.008$) that proves the larger the calcified plaque is, the higher load is required to press it.

8.4. Penetration and protrusion

Next, we evaluated penetration values obtained during stent expansion to figure out if any correlation exists between EM and amount of protrusion in the calcified plaque. Spearman’s correlation coefficient between EM and penetration was -0.9 ($p<0.0001$) considering as a strong negative relationship. Therefore, the stiffer the calcification, the less protrusion occurs during the expansion in CAS placement.

8.5. Ultimate External Pressure

Correlation of external loads and UTS/WSS/EM has already been presented in Sections III.B, C for both balloon and stent expansion in which obviously shows a strong positive relationships. However there is no statistically significant correlation between ultimate external load and Ca score in both balloon and stent expansion by achieving spearman’s rho equal to 0.4 ($p<0.084$) and 0.53 ($p<0.019$) respectively despite having strong correlation with EM. We also evaluated the proportion of ultimate external load and area of calcification to know if the size has any impact on external load at break time. We obtained spearman’s rho equal to 0.6 ($p<0.008$) that proves the larger the calcified plaque is, the higher load is required to press it.

8.6. Tangent Modulus

Finally we examined the relationship exists between the numerically obtained TM that expresses the amount of plasticity and EM as elastic property of calcifications in both balloon and stent simulations. However in the balloon simulation due to some cases with zero TM, obtaining a meaningful correlation is not possible, but an implicit correlation is inferred that higher the EM, the less plastic (steeper slope) is the calcification, thus it is stiffer. However interpretation of this behavior cannot be fully determined. The same conclusion is achieved for stent simulation that is proved by a strong positive Spearman’s correlation between EM and TM equal to 0.791 ($p<0.0001$). This means that the steeper the elastic line is, the plastic slope also elevates higher and vice versa.

8.7. Conclusion

There is a gap in investigating the contribution of calcification in carotid artery plaque vulnerability during interventional carotid artery stenting operation. We performed nonlinear static structural simulations using Finite Element Method for both balloon and stent angioplasty in order to obtain mechanical parameters i.e. ultimate stress/strain, external load involved in calcified plaque fracture. The results correspond to the literature and nonlinear correlation between the mechanical and material parameters shows a negative correlation between Ca score and plaque rupture; however a strong positive correlation exists between elastic modulus of the calcifications and plaque vulnerability.

The long term goal of the current work is to exploit the latter correlations and perform regression analysis in order to develop a platform for pre-operative CAS operation and plaque vulnerability prediction by deploying material and mechanical characteristics of the objects involved.

There were some limitations and assumptions that we considered in this study as follows:

- Non-geometrical shapes of calcified plaque and the artery cause both CAD and CAE nontrivial, and it has a considerable impact on the final results.
- Lack of material properties for atherosclerotic calcification due to small amount of robust experimental analysis.
- Restriction in providing elaborated material properties for the stent and balloon from the vendor.
- Hemodynamic effect of blood flow on the imposed configuration is neglected due to complexity in analysis of computational fluid dynamics and nonlinear static structural modeling.
- Due to limited sample size statistical analysis could be considered less robust, however regression analysis is considered as future work in order to be able to prospect the sample size and also to predict the mechanical parameters.

Obtaining these parameters and relationships helps the researchers in developing a virtual platform for a pre-operative CAS in the future in order to predict the calcified plaque rupture and maximum external load to impose.

Bibliography

1. A.G. Hauss and M.J. Yaffe, “A categorical course in physics: technical aspects of breast imaging”, 78th Scientific Assembly and Annual Meeting of RSNA, 1994.
2. J.S. Suri and R.M. Rangayyan, “Recent Advances in Breast Imaging Mammography and Computer-Aided Diagnosis of Breast Cancer”, 1st edn. SPIE, 2006.
3. M. Anbar, C. Brown, L. Milescu, J. Babalola, et al. “The Potential of Dynamic Area Telethermometry in Assessing Breast Cancer”, IEEE Engineering in Medicine and Biology Magazine, Vol. 19, Issue: 3, pp. 58-62, 2000.
4. M. Anbar, L. Milescu, C. Brown, C. Carty, et al. “Diagnosis of Breast Cancer with Infrared Dynamic Area Telethermometry (DAT)”, Proc. Engineering in Medicine and Biology Society. Vol.2, pp.1215-1218, 2000.
5. R. Joro, AL. Lääperi, S. Soimakallio, R. Järvenpää, T. Kuukasjärvi, T. Toivonen et al. “Dynamic infrared imaging in identification of breast cancer tissue with combined image processing and frequency analysis”, Med Eng Technol. Vol. 32(4), pp. 325-35, 2008.
6. V. Agostini, S. Delsanto, M. Knaflitz and F. Molinari, “Communications Noise Estimation in Infrared Image Sequences: A Tool for the Quantitative Evaluation of the Effectiveness of Registration Algorithms”, IEEE Transaction on Biomedical Engineering, Vol. 55, No. 7, pp. 1917-1920, 2008.
7. S. Riyahi-Alam, M. Peroni, G. Baroni and M. Riboldi, “Regularization in deformable registration of biomedical images based on divergence and curl operators”, Methods Inf. Med. Vol. 53, pp. 21–28, 2014.
8. Y.L. Sant. “An image registration method for infrared measurements”, Quantitative InfraRed Thermography. Vol. 2, No.2, pp. 207-222, 2005.
9. V. Agostini, S. Delsanto, F. Molinari and M. Knaflitz. “Evaluation of feature-based registration in dynamic infrared imaging for breast cancer diagnosis”, Proc. IEEE Eng Med Biol Soc. Vol. 1, pp. 953-956, 2006.
10. V. Agostini, M. Knaflitz and F. Molinari, “Motion Artifact Reduction in Breast Dynamic Infrared Imaging”. IEEE Transaction on Biomedical Engineering, Vol. 56, No.3, pp. 903-906, 2009.
11. L. Ibanez, W Schroeder. L. Ng and J Cates. The ITK software guide. Insight Toolkit Kitware Inc, 2003.
12. N. Scales, C. Herry and M. Frize. “Automated Image Segmentation for Breast Analysis using Infrared Images”, Proc. IEEE Eng Med Biol Soc. Vol. 3, pp. 1737-40, 2004.
13. 3D Slicer. [Internet]. Available from http://www.slicer.org.
14. J. V. Hajnal and D. L.G. Hill, Medical Image Registration, CRC Press, pp. 46-50, 2001.
15. S. Klein, M. Staring and J. P. W. Pluim, “Evaluation of Optimization Methods for Nonrigid Medical Image Registration using Mutual Information and B-Splines”, IEEE Transaction On Image Processing, Vol. 16, pp. 2879-2890, 2007.
16. T. Guerrero, G. Zhang, T. Huang, K. Lin, “Intrathoracic tumour motion estimation from CT imaging using the 3D optical flow method”, Physics in Medicine and Biology, Vol. 49, No. 17, Aug 2004.
17. D. Rueckert, L. I. Sonoda, C. Hayes, D. L. G. Hill, M. O. Leach, and D. J. Hawkes, “Nonrigid registration using free-form deformations”, Application to breast MR images, IEEE Transaction on Medical Imaging, Vol. 18, No. 8, Aug 1999.
18. P. Viola, W. M. Wells, “Alignment by Maximization of Mutual Information”, International Journal of Computer Vision, Vol. 24, Issue. 2, pp. 137–154, 1997.

19. G. E. Christensen, H. J. Johnson, “Consistent Image Registration”, IEEE Transaction on Medical Imaging, Vol. 20, Issue. 7, pp.568 – 582, Aug 2002.
20. G. E. Christensen, J. He, “Consistent Nonlinear Elastic Image Registration”, IEEE Transaction on Mathematical Methods in Biomedical Image Analysis, pp.37 – 43, Aug 2002.
21. T. Rohlfing, R. Calvin, Jr. Maurer, A. David, M. A. Jacobs, “Volume-Preserving Nonrigid Registration of MR Breast Images Using Free-Form Deformation With an Incompressibility Constraint”, IEEE Transaction on Medical Imaging, Vol. 22, Issue. 6, pp.730 – 741, July 2003.
22. Ch. Venkateswara Rao, K. M. M. Rao, A. S. Manjunath, and R. V. N. Srinivas. “Optimization of automatic image registration algorithms and characterization”, Proceedings of the ISPRS Congress, Istanbul, Turkey, pp. 698–702, July 2004.
23. H. Rezaei, S. Azadi, “Nonrigid Medical Image Registration using Hierarchical Particle Swarm Optimization”, IEEE Transaction on Soft Computing, Computing with Words and Perceptions in System Analysis, Decision and Control, ISBN: 978-1-4244-3429-9, pp. 1-4, Sep 2009.
24. A. Carreras, C. Ó. S. Sorzano, R. Marabini, J. M. Carazo, C. O. Solorzano, J. Kybic, “Consistent and elastic registration of histological sections using vector-spline regularization, in Computer Vision Approaches to Medical Image Analysis”, Lecture Notes in Computer Science, Vol. 4241. Springer Berlin / Heidelberg, pp. 85-95, May 2006.
25. M. Chu, H. Chen, C. Hsieh, T. Lin, H. Hsiao, G. Liao, Qi Peng, “Adaptive Grid Generation Based Non-rigid Image Registration using Mutual Information for Breast MRI”, Journal of signal processing systems, Vol. 54, No. 1-3, pp. 45-63.
26. Akinlar, M. Ali, “A new method for non-rigid registration of 3D images”, PhD Dissertation, University of Texas Arlington, DISS-10194, Jan 2009.
27. D. Ruan, S. Esedoglu, J. A. Fessler, “Discriminative sliding preserving regularization in medical image registration”, IEEE International Symposium on Biomedical Imaging, Vol. 129, ISBN: 9781424439317, pp. 430-433, 2009.
28. M. Urschler, S. Kluckner, H. Bischof, “A Framework for Comparison and Evaluation of Nonlinear Intra-Subject Image Registration Algorithms”, Institute of Computer Graphics and Vision, Graz, University of Technology, Austria, Insight Journal, 2008.
29. P. Hellier, C. Barillot, I. orouge, B. Gibaud, G. Le Goualher, D. L. Collins, A. Evans, G. Malandain, N. Ayache, G. E. Christensen, and H. J. Johnson, “Retrospective Evaluation of Intersubject Brain Registration”, IEEE Transaction on Medical Imaging, Vol. 22, Issue. 9, pp. 1120 - 1130, Sep 2003.
30. A. Klein et al, “Evaluation of 14 nonlinear deformation algorithms applied to human brain MRI registration”, Elsevier Science Direct Publication, NeuroImage, Vol. 46, Issue 3, pp. 786-802, July 2009.
31. T. Vercauteren, X. Pennec, et al. “Non-parametric diffeomorphic image registration with the demons algorithm”, Proc. MICCAI. Vol. 10, pp. 319-326, 2007.
32. G. E. Christensen and H. J. Johnson, “Consistent Image Registration”, IEEE Transaction on Medical Imaging, Vol. 20, Issue. 7, pp. 568-582, 2002.
33. T.M. Button, H. Li, P. Fisher, R. Rosenblatt, K. Dulaimy, S. Li et al. “Dynamic infrared imaging for the detection of malignancy”, Phys. Med. Biol. Vol. 49, pp. 3105–3116, 2004.
34. G. E. Christensen, “Consistent Linear-Elastic Transformations for Image Matching”, Information Processing In Medical Imaging, LNCS 1613, pp. 224-237, 1999.
35. H. Huang, R. Virmani, H. Younis, A.P. Burke, R.D. Kamm, R.T. Lee. “The impact of calcification on the biomechanical stability of atherosclerotic plaques”. Circulation. Vol. 103, Issue 8, pp. 1051–1056, 2001.

36. N. El-Barghouty, A. Nicolaides, V. Bahal, G. Geroulakos, A. Androulakis. “The identification of the high risk carotid plaque”. European Journal of Vascular and Endovascular Surgery, Vol. 11, Issue 4, pp. 470–478, 1996.
37. P. Tracqui, A. Broisat, J. Toczek, N. Mesnier, J. Ohayon, L. Riou. “Mapping elasticity moduli of atherosclerotic plaque in situ via atomic force microscopy”. J Struct Biol, Vol. 174, Issue 1, pp. 115–123, 2011.
38. Z. Teng, D. Tang, J. Zheng, P.K. Woodard, A.H. Hoffman. “An Experimental Study on the Ultimate Strength of the Adventitia and Media of Human Atherosclerotic Carotid Arteries in Circumferential and Axial Directions”. J Biomech, Vol. 42, Issue 15, pp. 2535–2539, 2009.
39. D. Bluestein, Y. Alemu, I. Avrahami, M. Gharib, K. Dumont, J.J. Ricotta, S. Einav. “Influence of microcalcifications on vulnerable plaque mechanics using FSI modeling”. J Biomech, Vol. 41, Issue 5, pp. 1111–1118, 2008.
40. D.I. Moussa, T. Rundek, J.P. Mohr, “Asymptomatic Carotid Artery Stenosis: A Primer on Risk Stratification and Management”, 1st ed., CRC Press, 2007, pp. 22–24.
41. J.J. Mulvihill, M.T. Walsh. “On the mechanical behavior of carotid artery plaques: the influence of curve-fitting experimental data on numerical model results”. Biomech Model Mechanobiol, Vol. 12, Issue 5, pp. 975–985, 2013.
42. G.A. Holzapfel, J.J. Mulvihill, E.M. Cunnane, M.T. Walsh. “Computational approaches for analyzing the mechanics of atherosclerotic plaques: a review”. J Biomech, Vol. 47, Issue 4, pp. 859–869. 2014
43. K.K. Wong, P. Thavornpattanapong, S.C. Cheung, Z. Sun, J. Tu. “Effect of calcification on the mechanical stability of plaque based on a three-dimensional carotid bifurcation model”. BMC Cardiovasc Disord, 12:7, 2012.
44. S. Zhao, L. Gu, S. R. Froemming. “Finite element analysis of the implantation of a self-expanding stent: impact of lesion calcification”. Journal of Medical Devices, Vol. 6, Issue 2, pp. 021001, 2012.
45. C. Yang, G. Canton, C. Yuan, M. Ferguson, T.S. Hatsukami, D. Tang. “Advanced human carotid plaque progression correlates positively with flow shear stress using follow-up scan data: an in vivo MRI multi-patient 3D FSI study”. J Biomech, Vol. 43, Issue 13, pp. 2530–2538, 2010.
46. T. Miura, N. Matsukawa, K. Sakurai, H. Katano, Y. Ueki, K. Okita, K. Yamada, K. Ojika. “Plaque vulnerability in internal carotid arteries with positive remodeling”. Cerebrovasc Dis Extra, Vol. 1, Issue 1, pp. 54–65, 2011.
47. A. Agatston, W.R. Janowiz, F.J. Hildner, N.R. Zusmer, M. Jr. Viamonte, R. Detrano. “Quantification of coronary artery calcium using ultrafast computed tomography”. J Am Coll Cardiol. Vol. 15, Issue 4, pp. 827–832, 1990.
48. H.E. Boyer, “Atlas of Stress-strain Curves”, 2nd ed., ASM International, pp. 12–17, 2002.
49. M.A. Meyers, P.Y Chen, “Biological Materials Science: Biological Materials, Bioinspired Materials, and Biomaterials”, 1st ed., Cambridge University Press, pp. 237–245, 2014.
50. L.L. Demer, Y. Tintut. “Vascular calcification: pathobiology of a multifaceted disease”. Circulation, Vol. 117, Issue 22, pp. 2938–2948, 2008.
51. C.L. Higgins, S.A. Marvel, J.D. Morrisett. “Quantification of calcification in atherosclerotic lesions”. Arterioscler Thromb Vasc Biol., Vol. 25, Issue 8, pp. 1567-1576, 2005.
52. J.Y. Rho, M.C. Hobatho, R.B. Ashman. “Relations of mechanical properties to density and CT numbers in human bone”. Med. Eng. Phys., Vol. 17, Issue 5, pp. 347-355, 1995.
53. U. Schneider, E. Pedroni, A. Lomax. “The calibration of CT Hounsfield units for radiotherapy treatment planning”. Phys Med Biol., Vol. 41, Issue 1, pp. 111-124, 1996.

54. R. Molteni, “From CT Numbers to Hounsfield Units in Cone Beam Volumetric Imaging: the effect of artifacts” 62th AAOMR, Annual Session, Chicago Illinois., (8-11), Dec. 2011.
55. E. Maher, A. Creane, S. Sultan, N. Hynes, C. Lally, D.J. Kelly. “Tensile and compressive properties of fresh human carotid atherosclerotic plaques”. J Biomech., 42(16), pp. 2760-2767, 2009.
56. R.T. Lee, S.G. Richardson, H.M. Loree, A.J. Grodzinsky, S.A. Gharib, F.J. Schoen, N. Pandian. “Prediction of mechanical properties of human atherosclerotic tissue by high-frequency intravascular ultrasound imaging an in vitro study”. Arteriosclerosis, Thrombosis and Vascular Biology, Vol 12, Issue 1, pp. 1-5, 1992.
57. M.G. Lawlor, M.R. O'Donnell, B.M. O'Connell, M.T. Walsh. “Experimental determination of circumferential properties of fresh carotid artery plaques”. J Biomech., Vol. 44, Issue 9, pp. 1709-1715, 2011.
58. K.R. Nandalur, E. Baskurt, K.D. Hagspiel, M. Finch, C.D. Phillips, S.R. Bollampally, C.M. Kramer. “Carotid artery calcification on CT may independently predict stroke risk”. AJR Am J Roentgenol., 186(2), pp. 547-552, 2006.
59. N. Maldonado, A. Kelly-Arnold, Y. Vengrenyuk, D. Laudier, J.T. Fallon, R. Virmani, L. Cardoso, S. Weinbaum. “A mechanistic analysis of the role of microcalcifications in atherosclerotic plaque stability: potential implications for plaque rupture”. Am J Physiol Heart Circ Physiol., Vol. 303, Issue 5, pp. 619-628, 2012.
60. Y. Vengrenyuk, S. Carlier, S. Xanthos, L. Cardoso, P. Ganatos, R. Virmani, S. Einav, L. Gilchrist, S. Weinbaum. “A hypothesis for vulnerable plaque rupture due to stress-induced debonding around cellular microcalcifications in thin fibrous caps”. Proc Natl Acad Sci U S A., 103(40), pp. 14678-14683, 2006.

Curriculum Vitae

PERSONAL INFORMATION

Sadegh Riyahi Alam

Address: Corso Duca degli Abruzzi, n. 24, Department of Mechanical and Aerospace engineering,
Politecnico di Torino, 10129, Turin, Italy.

Office phone: +39-(0)11-903394, Mobile: +39-3284563145
Email: sadegh.riyahi@polito.it
Skype ID: sadeghit
Website: http://socrate.polito.it/biolab/Home.html
Researchgate: https://www.researchgate.net/profile/Sadegh_Riyahi_Alam
Linkedin: https://www.linkedin.com/profile/public-profile-settings?trk=prof-edit-edit-public_profile

Date of birth: 17/01/1983 | Nationality: Iranian

RESEARCH INTERESTS

- Computer aided detection/diagnosis (CAD), Computer Vision.
- Medical image processing, Image Registration and Segmentation.
- Biomechanical finite element analysis (FEM), CAD/CAE.
- Cardiovascular imaging, Vascular mechanobiology, Carotid Artery Stenting, Atherosclerosis.
- Breast dynamic infrared imaging, Digital Mammography.
- 4DCT Adaptive/Image guided radiotherapy.

EDUCATION

Jan 2012 – Jan 2015

PhD in Biomedical Engineering

Politecnico di Torino, Turin, Italy

Thesis title: Preoperative Systems for Computer-Aided-Diagnosis based on image registration: applications to Breast Cancer and Atherosclerosis.

I have been involved in two projects to develop a Computer Aided Diagnostic System comprising:

1. Implementation of automated 3D time-series image registration methods in Breast Dynamic Infrared Images for detection of breast cancer. We developed both linear and non-linear registration methods using ITK in order to remove the patient movements to facilitate the patient acquisition procedure and improve further spectral analysis of vascular temperature modulation for the prospective breast cancer prognosis.

2. Patient-specific pre-operative carotid artery stenting simulation using Finite Element Analysis by considering Agatston score of calcified plaques in which using Computer Vision and in silico analysis, we assessed contribution of calcification in carotid atherosclerotic plaque rupture. We also performed correlation/regression analysis between material properties of calcification and obtained mechanical parameters to predict the plaque vulnerability.

Feb 2009 – Dec 2011

Master of Science in Computer Engineering

Politecnico di Milano, Milan, Italy

- *Thesis title*: Implementation of divergence and curl operators embedded cost function in deformable image registration for adaptive radiotherapy.

Sep 2001 – Sep 2006

Bachelor of Science in Computer Engineering (Software)

Azad University-Tehran Central Branch, Tehran, Iran

- *Thesis title*: Mammographic reporting and viewer software developed for Computer Aided Diagnostic (CAD) system of screening mammography.

RESEARCH EXPERIENCES

Oct 2013 – May 2014

Visiting researcher in vascular mechanobiology

- **Yokoyama Lab, Department of Biomedical Engineering, Nagoya city university, Nagoya, Japan.**
- **Department of Neurosurgery, Nagoya City University Graduate School of Medical Sciences, Nagoya, Japan.**

Supervisors: Kiyoko Yokoyama, Hiroyuki Katano

- Computer vision based nonlinear static simulation of patient-specific pre-operative carotid artery stenting using *in vivo* MDCT images in order to evaluate mechanical and material behaviour of calcified plaques in plaque vulnerability by exploiting finite element method.

Sep 2010 – Dec 2011

Trainee in biomedical image processing

- **TBM Bioengineering Laboratory Technologies, Department of Bioengineering, Politecnico di Milano, Milan, Italy.**

Supervisors: Marco Riboldi, Marta Peroni, Guido Baroni

- Analyse and implementation of a novel cost function for deformable image registration of 4DCT images using divergence and curl operators for adaptive radiotherapy application by ITK, VTK and Plastimatch.

July 2005 – Feb 2009

Image processing software developer

- **Medal Electronic Engineering Co. Ltd., Tehran, Iran. http://www.medalelectronic.com**

Supervisor: R. Aghazadeh Zoroufi

- Implementation of a Computer Aided Diagnostic System for microcalcification and mass detection in digital xray mammograms.
- Development of a Computer Aided Diagnostic Software for segmentation of Multiple Sclerosis (MS) plaques in MRI images using 3D slicer, FSL and MRIcron.

PUBLICATIONS

International Journals

1. **S. Riyahi-Alam**, K. Yokoyama, H. Katano, U. Morbiducci, A. Audenino, F. Molinari, "Preoperative carotid artery stenting simulation using Finite Element Analysis by considering Agatston score of calcified plaques", IEEE transaction on Biomedical Engineering, Submitted Feb 2015. In Peer-review.

2. **S. Riyahi-Alam**, V. Agostini, F. Molinari, M. Knaflitz, "Comparison of time-series registration methods in breast dynamic infrared imaging", Journal of Opto-Electronics Review, ISSN:1230-3402; Vol 23, Issue 1, January 2015, pp.68-77.

3. **S. Riyahi-Alam**, M. Peroni, G. Baroni, M. Riboldi. "Regularization in deformable registration of biomedical images based on divergence and curl operators", Journal of Methods of Information in Medicine, ISSN: 0026-1270; Vol 53, Issue 1, January 2014, pp.21-28.

4. **S. Riyahi-Alam**, N. Riahi. "Implementation analysis of a Mammographic Computer-Aided Diagnostic (CAD) System", International Journal of Medical Physics, Vol 38, Issue 6, 3396 / Joint AAPM/COMP Meeting Program, July 2011.

5. N. Riahi, F. Younesi, **S. Riyahi-Alam**. "Computer-Aided Mass Detection on Digitized Mammograms using a Novel Hybrid Segmentation System", North Atlantic University Union (NAUN) International Journal Of Biology And Biomedical Engineering, Vol 3, Issue 4, 2009, pp.51-56.

Conference Proceedings

1. **S. Riyahi-Alam**, U. Morbiducci, H. Katano, K. Yokoyama, S. Ali, A. Audenino, F. Molinari, "Preoperative in silico analysis of atherosclerotic calcification vulnerability in carotid artery stenting using Finite Element Analysis by considering Agatston score", World Congress on Medical Phys. and Biomedical Eng–IFMBE / IUPESM 2015, Jun 2015, Toronto, Canada, Submitted, In Peer Review.

2. S. Ali, M. Giachino, A. Bonani, A. Aprato, **S. Riyahi-Alam**, A. Khattab, C. Bignardi, A. Massè, "Pelvic Ring Fractures: External Fixation Comparative Numerical Structural Analysis", Proceeding of IEEE 7th Cairo International Biomedical Engineering Conference-IBEC2014, Dec 2014, Giza, Egypt.

3. **S. Riyahi-Alam**, V. Agostini, F. Molinari, M. Knaflitz. "Evaluation of time-series registration methods in Dynamic Area Telethermometry for breast cancer detection", Proceeding of 12th International Conference on Advanced Infrared Technology and Applications, Sep 2013, Turin, Italy, pp. 147-159.

TECHNICAL SKILLS

- Excellent programming skills in ***MATLAB and Visual C++ using ITK, VTK.***
- Experienced in ***3D Slicer***, **Amira**, **Plastimatch**, ***FSL, MRIcron and PACSPLUS*** for CT and MRI data analyses.
- Good knowledge in Finite Element Method and CAD/CAE using ***Mimics, Rhinoceros, Solidworks and Ansys***.
- Good knowledge in Statistical software ***Minitab*** as well as ***Unix and Linux*** operating systems.
- Good programming skills in ADO and ODBC database technology with Microsoft SQL Server.

PROFESSIONAL ACTIVITY

Reviewer: Journal of Medical Imaging and Health Informatics (JMIHI).

Workshop: 1st International workshop on Nanotechnology in Cancer Treatment. 10th Nov 2014. Castello del Valentino, Politecnico di Torino.

AWARDS and SCHOLARSHIPS

1. *The best paper award*: 12th International Conference on Advanced Infrared Technology and Applications (AITA 2013), Castello Del Valentino, Turin, Italy, Sep 2013.

2. *The Italian Government*: Italian Government Scholarship. 2012-2015.

3. *Award*: Innovations, Inventions and Scientific Speculation for "*Designing a Computer-Aided-Diagnostic System (CAD) for Assessment of Digital Mammograms in Iran*", The 11th Razi Research Festival on Medical Sciences, Ministry of Health & Higher Medical Educations, 27th December, 2005, Tehran, Iran.

REFERENCES

Prof. Filippo Molinari, Associate professor at department of Electronics and Telecommunication, Politecnico di Torino, Turin, Italy.
Website: http://socrate.polito.it/biolab/Home.html.
Email: filippo.molinari@polito.it. Tel: +39 (0)110904135

Prof. Kiyoko Yokoyama, Professor at Graduate School of Design and Architecture, Nagoya City University, Nagoya, Japan.
Website: http://www.sda.nagoya-cu.ac.jp/yokoyama.
Email: yokoyama@sda.nagoya-cu.ac.jp. Tel: +81-52-721-5439

Prof. Alberto Audenino, Professor at department of Mechanical and Aerospace engineering, Politecnico di Torino, Turin, Italy.
Email: alberto.audenino@polito.it. Tel: +39 (0)110906932

BACKGROUND SUMMARY

Graduating in biomedical engineering, I have deep technical skills in software development, specially in computer aided diagnostic/detection systems for biomedical applications. Starting from my academic career I was involved in several projects such as mass and microcalcification detection in digital mammography and implementation of novel deformable image registration for adaptive radiotherapy applications. During my PhD career, as a visiting researcher in Nagoya university, I was involved in biomechanical project of patient-specific pre-operative carotid artery stenting simulation using Finite Element Analysis in which elastic-plastic material behaviour of the calcification is observed in Atherosclerotic plaque rupture.
I also carried out a project regarding image/signal processing for implementation of 3D Time-series registration methods on dynamic infrared images for breast cancer detection to facilitate the spectral analysis of vascular temperature modulation for further prognosis.
In these projects I was able to deal with complex and multi-disciplinary subjects both in individual and team work with high level of autonomy.

PERSONAL SKILLS

Mother tongue(s) **Persian**

Other language(s)

	UNDERSTANDING		SPEAKING		WRITING
	Listening	Reading	Spoken interaction	Spoken production	
English	**C1**	**C1**	**C1**	**C1**	**C2**
Japanese	**C1**	**C1**	**C1**	**C1**	**C1**
Italian	**B1**	**B1**	**B1**	**B1**	**B1**

Levels: A1/2: Basic user - B1/2: Independent user - C1/2 Proficient user

Publications

1. **S. Riyahi-Alam**, K. Yokoyama, H. Katano, U. Morbiducci, A. Audenino, F. Molinari, “Preoperative carotid artery stenting simulation using Finite Element Analysis by considering Agatston score of calcified plaques”, IEEE transaction on Biomedical Engineering, Submitted Feb 2015. In Peer-review.
2. **S. Riyahi-Alam**, V. Agostini, F. Molinari, M. Knaflitz, “Comparison of time-series registration methods in breast dynamic infrared imaging”, Journal of Opto-Electronics Review, ISSN:1230-3402; Vol 23, Issue 1, January 2015, pp.68-77.
3. **S. Riyahi-Alam**, M. Peroni, G. Baroni, M. Riboldi. “Regularization in deformable registration of biomedical images based on divergence and curl operators”, Journal of Methods of Information in Medicine, ISSN: 0026-1270; Vol 53, Issue 1, January 2014, pp.21-28.
4. **S. Riyahi-Alam**, N. Riahi. “Implementation analysis of a Mammographic Computer-Aided Diagnostic (CAD) System”, International Journal of Medical Physics, Vol 38, Issue 6, 3396 / Joint AAPM/COMP Meeting Program, July 2011.
5. N. Riahi, F. Younesi, **S. Riyahi-Alam**. “Computer-Aided Mass Detection on Digitized Mammograms using a Novel Hybrid Segmentation System”, North Atlantic University Union (NAUN) International Journal Of Biology And Biomedical Engineering, Vol 3, Issue 4, 2009, pp.51-56.

6. **S. Riyahi-Alam**, U. Morbiducci, H. Katano, K. Yokoyama, S. Ali, A. Audenino, F. Molinari, “Preoperative in silico analysis of atherosclerotic calcification vulnerability in carotid artery stenting using Finite Element Analysis by considering Agatston score”, World Congress on Medical Phys. and Biomedical Eng–IFMBE / IUPESM 2015, Jun 2015, Toronto, Canada, Submitted, In Peer Review.
7. S. Ali, M. Giachino, A. Bonani, A. Aprato, **S. Riyahi-Alam**, A. Khattab, C. Bignardi, A. Massè, “Pelvic Ring Fractures: External Fixation Comparative Numerical Structural Analysis”, Proceeding of IEEE 7th Cairo International Biomedical Engineering Conference-IBEC2014, Dec 2014, Giza, Egypt.
8. **S. Riyahi-Alam**, V. Agostini, F. Molinari, M. Knaflitz. “Evaluation of time-series registration methods in Dynamic Area Telethermometry for breast cancer detection”, Proceeding of 12th International Conference on Advanced Infrared Technology and Applications, Sep 2013, Turin, Italy, pp. 147-159.